OPTIMIZATION-ORIENTED MODELING AND ANALYSIS OF RIS-ASSISTED SWIPT-IOT SYSTEMS

Ph.D. Thesis

by

Neha Sharma
Roll No. 2201102021



Department of Electrical Engineering
INDIAN INSTITUTE OF TECHNOLOGY INDORE

September 2026

OPTIMIZATION-ORIENTED MODELING AND ANALYSIS OF RIS-ASSISTED SWIPT-IOT SYSTEMS

A Thesis

Submitted in partial fulfillment of the
requirements for the award of the degrees
of
Doctor of Philosophy

by

Neha Sharma
Roll No. 2201102021



Department of Electrical Engineering
INDIAN INSTITUTE OF TECHNOLOGY INDORE
September 2026

INDIAN INSTITUTE OF TECHNOLOGY INDORE

I hereby certify that the work which is being presented in the Thesis entitled **'Optimization-oriented Modeling and Analysis of RIS-assisted SWIPT-IoT Systems'** in the partial fulfillment of the requirements towards the award of the **Doctor of Philosophy** degree and submitted in the **Department of Electrical Engineering**, Indian Institute of Technology Indore, is an authentic record of my own work carried out during the time period from **July 2022** to **June 2026** under the supervision of **Dr. Sumit Gautam**.

The matter presented in this Thesis has not been submitted by me for the award of any other degree of this or any other institute.

21-09-2026

Signature of the student with date

(Neha Sharma)

This is to certify that the above statement made by the candidate is correct to the best of my knowledge.

21-September-2026

Signature of Thesis Supervisor with date

(Dr. Sumit Gautam)

Neha Sharma has successfully given his/her Ph.D. Oral Examination held on *21 September 2026*.

21-September-2026

Signature of Thesis Supervisor with date

(Dr. Sumit Gautam)

ACKNOWLEDGEMENTS

I would like to express my deepest gratitude to all those who have supported and encouraged me throughout my Ph.D. journey.

First and foremost, I am sincerely thankful to my supervisor, Dr. Sumit Gautam, whose invaluable guidance, continuous encouragement, and unwavering support has been a constant source of inspiration. His insightful advice and constructive feedback have shaped the direction of this research and contributed significantly towards the completion of the Thesis. It has been a privilege to work under his supervision. I am also grateful to Prof. Swaminathan R., and Prof. Aniruddha Singh Kushwaha, the PSPC members of my research progress committee, for their thoughtful suggestions, critical evaluations, and motivating discussions. Their insightful comments have greatly enhanced the quality and depth of this research work.

My sincere acknowledgment to Prof. Suhas Joshi, Director, Indian Institute of Technology Indore, for providing me the opportunity to explore my research capabilities at Indian Institute of Technology Indore. I would like to thank the respective Head of the Department, Electrical Engineering, for their kind support. I am also indebted to the administrative and technical staff at the Indian Institute of Technology Indore, India, whose support has been invaluable in overcoming many logistical and technical challenges during my research.

I am grateful to my research collaborators and eminent Professors: Prof. Symeon Chatzinotas, Prof. Björn Ottersten, Dr. Swaminathan R., Prof. Aryan Kaushik, Prof. Prabhat Kumar Upadhyay, Prof. Prabhat Kumar Sharma and Prof. Anamika Singh for their invaluable guidance. I am equally thankful to my dear friends who gradually became valued research collaborators throughout this academic journey namely, Mr. Manojkumar Balaji Kokare, Ms. E.N.S.S Anjana, and Ms. Shivani Dhok for fostering a supportive environment that greatly contributed to my learning and personal growth. Special mention to Dr. Suchitra Tiwari who helped me survive in the foreign land during my research stay in Luxembourg.

I would like to mention the support of my friends and colleagues during this Ph.D journey Mr. Pawan Soni, Ms. Shilpa Vishwakarma, Mr. Nayim Ahmed, Mr. Prashant Sharma,

and WiSTAR lab members.

I am profoundly grateful to my family for their unconditional support, encouragement, and unwavering belief in me throughout my academic journey. I extend my heartfelt appreciation to my parents: Dr. Nisha Jyoti Sharma and Mr. Vishnu Sharma, as well as my parents-in-law: Mrs. Gita Mishra and Mr. Bharat Bhushan Mishra, who believed in their daughter above societal expectations. Their constant encouragement and blessings have been a continuous source of strength and motivation. It is with profound gratitude that I acknowledge the unwavering support of my spouse, Mr. Ghanshyam Bhushan, whose patience, understanding, and encouragement have sustained me through the challenges and accomplishing the milestones of this journey. The constant support of my brother: Mr. Deepak Sharma has been a source of strength and reassurance.

Finally, I fondly remember the departed souls: my maternal grandfather, Late Mr. Shashi Bhushan Sharma, for passing on the academic intellect; and paternal grandfather, Late Dr. Bhramanand Sharma, for his wise wisdom, vision and open thinking.

I also acknowledge the Prime Minister Research Fellows (PMRF) scheme of Govt. of India, and the SIGCOM group, SnT, University of Luxembourg, Luxembourg, for providing the financial resources necessary to complete my work. I would like to thank all those who have contributed to this Thesis, directly or indirectly. Your support and contributions have been instrumental in the completion of my Ph.D. research work.

Last but not the least, I thank Shiva-the Supreme Lord for giving me the opportunity, strength, and ability to undertake and successfully complete this research work.

Neha Sharma

Dedicated

to

My Parents

ABSTRACT

The rapid evolution of wireless communication technologies toward beyond-5G (B5G) and sixth-generation (6G) networks has unlocked a new era of massive connectivity and intelligent automation, where billions of Internet-of-Things (IoT) devices are expected to reshape the application areas ranging from remote environmental monitoring to precision agriculture. Such areas require the self-sufficiency of IoT devices with higher data rate and energy harvesting (EH) solutions that are convenient, safe, uninterruptible and flexible. The conventional EH options like wind, solar, etc., are highly unpredictable, thus harnessing radio frequency (RF) electromagnetic (EM) waves and convert them to usable direct current (DC) serves our purpose.

In this context, Simultaneous Wireless Information and Power Transmission (SWIPT) has emerged as a promising approach capable of jointly delivering information and RF energy to wireless devices, having potential to reduce the need for frequent battery replacement. When extending the coverage of SWIPT receivers, a green communication solution lies in integration of SWIPT with Reconfigurable Intelligent Surfaces (RIS) technology. RIS has gained considerable attention due to its ability to intelligently manipulate the wireless propagation environment, thereby significantly enhancing the communication reliability and energy efficiency (EE). Motivated by these advancements, this thesis presents a comprehensive investigation of RIS-assisted SWIPT systems for next-generation IoT-enabled wireless networks under practical deployment constraints.

The first chapter of this thesis presents a comprehensive overview of the considered research topic, which establishes the fundamental basis for the subsequent studies. It highlights the key contributions of the thesis, discusses about the adopted optimization tools, and provides a structured outline of the overall organization of the work. Following this, a detailed overview of SWIPT, RIS technology and their advanced integration into the wireless communication systems is provided. Fundamental concepts, practical EH models, and RIS hardware variants are systematically discussed to establish the theoretical foundation of the thesis. Furthermore, a case study on diverse areas of smart agriculture highlight-

ing the compatibility of RIS-assisted SWIPT-IoT with emerging technologies is presented. Furthermore, the thesis work has been divided into four main research topics, summarized as follows. Firstly, a multiple RIS-assisted SWIPT-IoT frameworks considering practical hardware impairments is investigated, with distinct tri-optimization problems of data rate, EH, and EE under Quality-of-Service (QoS) constraints using both time-switching (TS) and power-splitting (PS) SWIPT protocols. Next, the system is advanced with multiple RIS-user pair, dealing with joint rate-energy (R-E) optimization problem. Subsequently, the heart and core of RIS system with active and passive beamforming optimization, considering multi-user (MU) multiple-input single-output (MISO) systems is examined. Then, Simultaneously Transmitting and Reflecting RIS (STAR-RIS) system is studied with energy splitting (ES) and mode switching (MS) operational protocols, to provide full-space intelligent signal manipulation and extending coverage of RIS. Practical considerations such as discrete phase shift (DPS) constraints, phase-dependent amplitude reflection, non-linear energy harvesting (NL-EH) models, and imperfect channel state information (ICSI) are incorporated to capture real-world deployment scenarios. To address the highly coupled and non-convex optimization problems, several advanced optimization frameworks and algorithms are developed. Extensive numerical simulations are conducted to validate the effectiveness, robustness, complexity, latency and convergence behavior of the proposed algorithms under varying system parameters. Lastly, the thesis concludes to provide a unified and practical perspective on optimization, resource allocation, and hardware-aware design of RIS-assisted SWIPT-IoT systems. Additionally, future research directions are highlighted for sustainable and intelligent 6G wireless networks.

Keywords: Beamforming, Energy Efficiency (EE), Energy Harvesting (EH), Internet-of-Things (IoT), Optimization Techniques, Reconfigurable Intelligent Surfaces (RIS), Simultaneous Wireless Information and Power Transmission (SWIPT), Simultaneous Transmitting and Reflecting RIS (STAR-RIS).

Contents

List of Figures vi

List of Tables xi

List of Abbreviations xiii

Notations xvii

List of Publications xxii

1 Introduction 1

1.1 Problem Overview and Motivation 3

1.2 Major Objectives of this thesis 4

1.3 Contributions and Main Highlights 5

1.4 Discussion on Optimization Problems and Techniques 8

1.5 Organization of the thesis 10

2 Review of RIS-SWIPT Systems 15

2.1 Reconfigurable Intelligent Surfaces (RIS) 16

2.1.1 RIS and its variants 17

2.1.1.1 Reflect-only RIS 17

2.1.1.2 STAR-RIS 18

2.1.1.3 Hybrid Active-Passive RIS 19

2.1.1.4 Beyond Diagonal RIS (BD-RIS) 19

2.2 Simultaneous Wireless Information and Power Transmission (SWIPT) . . . 20

2.2.1 Energy Harvesting (EH) Models 21

2.3 Amalgamation of RIS and SWIPT 24
2.4 Case Study: Smart Agriculture 25
2.4.1 Advanced Farming 27
2.4.2 Animal Husbandry Management 28
2.4.3 Storage Management 28
2.4.4 Agri-logistics Monitoring 29
2.5 Summary 29

3 Integrating Multiple RIS for Enhanced SWIPT-IoT Performance 31
3.1 Introduction to Multi-RIS assisted SWIPT-IoT Systems 32
3.2 System Model 36
3.2.1 Signal Modeling 37
3.2.2 Multi-RIS Selection Strategies 39
3.2.2.1 Optimal RIS Approach (ORA) 39
3.2.2.2 Exhaustive RIS Approach (ERA) 40
3.2.3 Simultaneous Wireless Information and Power Transmission (SWIPT) 41
3.3 Data Rate Maximization 42
3.3.1 Optimized solution for TS 43
3.3.2 Optimized solution for PS 44
3.4 Harvested Energy Maximization 46
3.4.1 Optimized solution for TS 46
3.4.2 Optimized solution for PS 48
3.4.3 Algorithmic Solution for Rate and EH Maximization 49
3.5 Maximization of Energy Efficiency (EE) 53
3.5.1 Dinkelbach based Solution 54
3.6 Results and Discussion 55
3.7 Summary 61

4 Joint Rate-Energy Optimization in RIS-assisted SWIPT-IoT System 63

4.1 Introduction to Fractional Programming Strategy in RIS-assisted SWIPT-IoT Systems . . . 64
4.2 System Model . . . 67
4.2.1 Practical Phase Shift Model . . . 68
4.2.2 Signal Model . . . 69
4.2.2.1 Discrete Phase Shift Model . . . 70
4.3 Problem Formulation and Proposed Solution . . . 71
4.3.1 KKT Conditions based Solution . . . 72
4.3.2 Dinkelbach based Solution . . . 74
4.3.3 Quadratic Transform based Solution . . . 75
4.3.4 Intermediate Algorithmic Solution . . . 77
4.4 Results and Discussion . . . 79
4.5 Summary . . . 83

5 Active and Passive Beamforming in RIS-assisted SWIPT-IoT system 85

5.1 Introduction to Joint Active-Passive Beamforming Optimization in RIS-assisted SWIPT-IoT System with DPS . . . 86
5.2 System Model . . . 91
5.2.1 Imperfections in Channel . . . 92
5.2.2 Signal Model . . . 93
5.3 Problem Formulation and Solution . . . 95
5.3.1 Joint Optimization of Beamforming Vector and PS Ratio . . . 97
5.3.1.1 Solution via SDR method . . . 97
5.3.1.2 ZF based Closed form Solution . . . 100
5.3.2 Phase Shift Optimization . . . 103
5.3.3 Overall Transmit Power Minimization . . . 106
5.4 Simulation Results . . . 108
5.4.1 Single User System . . . 110
5.4.2 Multiple User system . . . 111

5.4.2.1 Algorithmic Comparison . . . 111
5.4.2.2 Number of RIS Elements and Antenna Count . . . 116
5.4.2.3 Impact of Optimized Phase and Quantized Phase Level . . 116
5.4.2.4 Variation in the Number of Users . . . 120
5.4.2.5 Impact of CSI Error . . . 121
5.5 Summary . . . 122

6 STAR-RIS assisted SWIPT-IoT System 125
6.1 Maximizing Weighted Function in STAR-RIS aided SWIPT-IoT with Discrete Phase Shifting . . . 126
6.2 System Model . . . 129
6.2.1 SWIPT with STAR-RIS in Energy Splitting mode . . . 130
6.2.2 SWIPT with STAR-RIS in Mode Switching Framework . . . 131
6.3 Problem Formulation and Solution . . . 132
6.3.1 Weighted Rate-Energy Maximization Problem . . . 133
6.3.2 Proposed Solution . . . 134
6.3.2.1 Computational Complexity . . . 136
6.4 Results and Discussion . . . 136
6.4.1 Impact of Energy Split and Element Division . . . 138
6.4.2 Impact of DPS Levels . . . 140
6.5 Summary . . . 142

7 Conclusion and Future Directions 143
7.1 Main Conclusions . . . 143
7.2 Future Directions . . . 145
7.2.1 Potential Extensions . . . 146
7.2.2 Towards Novel Problem Formulations and Solutions . . . 148

A Optimization Techniques 152
A.1 Relevant Optimization Techniques . . . 152
A.1.1 Classification based on Uncertainty . . . 152

A.1.2 Classification based on Optimization Objective 153
A.1.3 Classification based on the Nature of Variables 153
A.1.4 Classification based on Nature of Constraints 154
A.2 Leveraged Optimization Techniques 154
A.2.1 Karush-Kuhn-Tucker (KKT) Conditions 155
A.2.2 Semidefinite Programming (SDP) 156
A.2.3 Gaussian Randomization 156
A.2.4 Fractional Programming 157
A.2.5 Alternate Optimization (AO) 158

B Appendices for Chapter 3 **160**

B.1 Rate Maximization using KKT Optimization 160
B.2 EH Maximization using KKT Optimization 160

List of Figures

1.1 Main contributions of this thesis in a nut-shell. 6

1.2 Taxonomy of optimization problems and list of convex optimization techniques used in this thesis. 9

2.1 Basic structure of RIS. 16

2.2 STAR-RIS operates via three main protocols, mode switching (MS), energy splitting (ES), and time switching (TS); serving the information receivers (IRs) in the reflection zone as well as energy receivers (ERs) in the transmission zone. 18

2.3 The TS and PS-SWIPT receiver architecture. 20

2.4 Power harvested by various models along with the energy conversion efficiency. 21

2.5 Basic system model for SISO RIS-assisted SWIPT-IoT system, considering PS-SWIPT and TS-SWIPT user receiver. 24

2.6 Identified areas of agriculture: advanced farming, animal husbandry, storage management and agri-logistics, with the showed impact of RIS-SWIPT in improving coverage and saving energy. 26

2.7 Integrated V2I-UAV-assisted communication system employing an RIS for enhanced coverage between a BS and a vehicle equipped with SWIPT-IoT sensor. The UAV positioned at a height performs EH to support its operation. 28

3.1 System model of IoT UE employing SWIPT in multi-RIS scenario. 37

3.2 Convergence plot of Algorithm 3.1 for rate and EH maximization with TS or PS cases. 53

3.3 Convergence plot of Algorithm 3.2 utilizing Dinkelbach Transform. 55

3.4 Comparison of distinct solutions for rate maximization with demanded EH. 56
3.5 Comparison of distinct solutions for EH maximization with maximum transmit power. 58
3.6 ERA and ORA schemes are compared for EE maximization with maximum transmit power to see the impact of increasing RIS elements. 59
3.7 Comparative Rate and EH maximization plots for TS and PS with the variation of (a) Number of RIS elements (assumed to be same for all RIS surfaces) (b) BS $-$ R_n $=$ R_n $-$ UE $=$ d distance. 59
3.8 EH variations with increased RIS surfaces for ERA and ORA schemes highlighting $\mathcal{R}_{th}$ differences. 60
3.9 Effect of imperfect CSI on rate maximization for both TS and PS. 60

4.1 System model for RIS assisted PS-SWIPT communication. 67
4.2 Reflection amplitude dependency on phase with circuit constants. 68
4.3 Convergence plot of UF maximization by DT and QT approach, utilizing Algorithms 4.2 and 4.3, respectively. 76
4.4 CDF plot of UF for number of RIS elements and ideal phase shift condition. 79
4.5 Comparative analysis of various solution types for UF vs $\mathcal{P}_{\text{max}}$. 80
4.6 R-E trade-off by converting UF to either rate/EH maximization problem for RIS elements and BS-RIS-U separation distance ($d_{br} = d_{ru} = d$). 81
4.7 UF comparison with number of RIS elements and demanded rate. 82
4.8 UF variations with number of DPS levels for different transmit power levels. Tremendous change in UF is observed from $L = 2$ to $L = 4$ and its saturation after $L = 64$. 83

5.1 System model for RIS assisted PS-SWIPT communication. 91
5.2 Solution frameworks for Problem (P1). 96
5.3 Flow chart summarizing the Algorithms: 5.1, 5.2, 5.3 and 5.4. 107
5.4 Convergence plot for the validation of various Algorithms. 108
5.5 Simulation setup for BS, RIS and users placement. 108

5.6 Comparison of optimized phase with random phase and CPS for single user employing MRT based beamformer. The ICSI with error index $\epsilon = 0.9$ shows increased power required for both random and optimized phase, when compared with the 'No ICSI' case. 111

5.7 Comparative analysis of various Algorithmic solution for $M = 20$. Herein, [R1] corresponds to [1]. 112

5.8 Execution time comparison for various algorithmic solutions of the primal problem. 114

5.9 Combined impact of RIS elements and BS antenna count on transmit power. 115

5.10 Minimized transmit power solved by ZF, varying with desired SINR and EH. The performance gains for random, optimized and QEPM [R2] (i.e., [2]) phase shift matrix are marked. 117

5.11 Optimized phase by Algorithm 5.3 is compared with random phase, QEPM [R2] (i.e., [2]) and MM phase model [R3] (i.e., [3]), for minimized power varying with demanded EH. 118

5.12 Minimized transmit power varying with desired SINR and EH for different quantized phase levels with $M = 100$. 119

5.13 Impact of increasing the users on transmit BS power with growing user's radial distance (r) and BS antenna count with $M = 100$. 120

5.14 Impact of channel state error on minimized power with quantized level and BS-RIS distance. 121

6.1 System model of STAR-RIS assisted SWIPT-IoT communication operating in ES and MS mode, simultaneously serving IR in reflection zone and ER in transmission zone. 129

6.2 Convergence of WRE function for ES and MS mode of transmission considering Case 2 (Table 6.2). 136

6.3 ES and MS comparison for various cases described in Table. 6.2. 138

6.4 Various types of solution comparisons for ES and MS with the number of STAR-RIS elements and reflection coefficient. Here, baseline solution [R4] corresponds to [4]. 139
6.5 Impact of DPS levels on WRE function with $\mathcal{P}_{\max}$ comparing conventional RIS. 140
6.6 Impact of DPS level on CDF plot of maximized WRE for ES and MS comparing PS. 141

List of Tables

2.1 Comparison of existing literature and present work. 22

3.1 General survey based on recent RIS-SWIPT frameworks. 33

4.1 Recent studies on RIS-SWIPT systems. 65
4.2 KKT cases for UF maximization. 73

5.1 Recent works on MISO multi-user RIS systems. 89
5.2 Simulation parameters 109
5.3 Comparative solution types 112
5.4 Comparative analysis of computational complexity 115

6.1 Comparison of existing literature on STAR-RIS assisted SWIPT systems. . 127
6.2 Simulation cases for ES and MS. 137
6.3 Parameter values' initializations 138

B.1 Rate maximization: KKT cases for TS scheme. 161
B.2 Rate maximization: KKT cases for PS scheme. 161
B.3 KKT cases for EH maximization in TS scheme. 162
B.4 KKT cases for EH maximization in PS scheme. 162

LIST OF ABBREVIATIONS AND ACRONYMS

5G	Fifth Generation Mobile Technology.
6G	Sixth Generation Mobile Technology.
AP	Access Point.
AO	Alternate Optimization.
AOA	Alternating Optimization Algorithm.
AWGN	Additive White Gaussian Noise.
B5G	Beyond 5G.
BB	Baseband.
BD-RIS	Beyond Diagonal RIS.
BS	Base Station.
CL	Constant-Linear.
CLC	Constant-Linear-Constant.
CPS	Continuous Phase Shift.
CSI	Channel State Information.
DAC	Digital-to-Analog Converter
DF	Decode-and-Forward.

DFBS	Dual-Functional Base Station.
DSRC	Dedicated Short-Range Communication.
DPS	Discrete Phase Shift.
DT	Dinkelbach Transform.
ECE	Energy Conversion Efficiency.
EE	Energy Efficiency.
EH	Energy Harvesting.
ER	Energy Receiver.
ES	Energy-Splitting.
EUs	Energy Users.
eMBB	Enhanced Mobile Broadband.
ERA	Exhaustive RIS Approach.
FSO	Free Space Optics.
GR	Gaussian Randomization.
HD	Half-Duplex.
HMIMO	Holographic Multi-Input-Multi-Output.
ID	Information Decoding.
IMT	International Mobile Telecommunications.
IoT	Internet-of-Things.
IoV	Internet-of-Vehicles.
IoX	Internet-of-Everything.
IR	Information Receiver.

IR^2S	Intelligent Reflecting and Refracting Surfaces.
ISABC	Integrated Sensing and Backscatter Communication.
ISAC	Integrated Sensing and Communication.
ITS	Intelligent Transportation Systems.
KKT	Karush-Kuhn-Tucker.
LoS	Line-of-Sight.
MF-RIS	Multi-Functional RIS.
MIMO	Multi-Input Multi-Output.
MISO	Multi-Input Single-Output.
mMTC	Massive Machine Type Communications.
MS	Mode Switching.
NLoS	Non Line-of-Sight.
NL-EH	Non-Linear Energy Harvesting.
ORA	Optimal RIS Approach.
PS	Power-Splitting.
QoS	Quality-of-Service.
QT	Quadratic Transform.
R-E	Rate-Energy.
RF	Radio Frequency.
RIS	Reconfigurable Intelligent Surfaces.
RSMA	Rate Splitting Multiple Access.

RT	Ray-Tracing.
SCMA	Sparse Code Multiple Access.
SDP	Semidefinite Programming.
SDR	Semidefinite Relaxation.
SIM	Stacked Intelligent Metasurfaces.
SINR	Signal-to-Interference-plus-Noise Ratio.
SISO	Single-Input Single-Output.
SNR	Signal-to-Noise Ratio.
STAR-RIS	Simultaneous Transmitting and Reflecting RIS.
SWIPT	Simultaneous Wireless Information and Power Transmission.
TS	Time-Switching.
UAV	Uncrewed Aerial Vehicle.
UCs	Unit Cells.
UE	User Equipment.
UF	Utility Function.
ULA	Uniform Linear Array.
URLLC	Ultra-Reliable and Low Latency Communications.
V2I	Vehicle-to-Infrastructure.
WPCN	Wireless Powered Communication Network.
WRE	Weighted Rate-Energy.
WSNs	Wireless Sensor Networks.
ZF	Zero-Forcing.

NOTATIONS

a, b, E', χ	Non-linear Energy Harvesting (NL-EH) modeled constant circuit parameters.
α	Time switching (TS) ratio.
β	Power splitting (PS) ratio.
β_k	PS ratio of the k^{th} user in multiple-input single-output (MISO) system.
C_0	Reference pathloss.
d_{BR} or d_{RU}	Base station (BS)-RIS or RIS-user separation distance, respectively.
E_h	Harvested energy at the user.
ϵ	Channel estimation error index.
η_i or η_m	Reflection coefficient of the i^{th} or m^{th} RIS element.
$\eta_{r,_i}$ or $\eta_{t,_i}$	Reflection coefficient of the i^{th} reflection or transmission STAR-RIS element.
$\mathbf{f}_k$	Cascaded channel from BS $\rightarrow$ RIS $\rightarrow$ U_k.
$\mathbf{g}_k$	Imperfect channel vector from RIS to the k^{th} user U_k in MISO system.
$\overline{\mathbf{g}_k}$	Line-of-Sight (LoS) channel vector from RIS to the k^{th} user U_k in MISO system.
$\tilde{\mathbf{g}_k}$	Baseband channel vector from RIS to the k^{th} user U_k in MISO system.

$\widehat{\mathbf{g}_k}$	Estimated LoS channel vector from RIS to the k^{th} user U_k in MISO system.
$\mathbf{g}_n$	Channel vector of n^{th} RIS-user pair.
$g_{R_{n(i)}}$	Channel magnitude from n^{th} RIS's i^{th} element to single user in multi-RIS system.
γ_{th}	Desired signal-to-interference-plus-noise ratio (SINR) threshold.
Γ_k or Γ_n	SINR/signal-to-noise ratio (SNR) at the k^{th} user or n^{th} RIS-user pair.
$\mathbf{H}$	Imperfect channel matrix from BS to RIS in MISO system.
$\overline{\mathbf{H}}$	LoS channel matrix from BS to RIS in MISO system.
$\tilde{\mathbf{H}}$	Baseband channel matrix from BS to RIS in MISO system.
$\widehat{\mathbf{H}}$	Estimated LoS channel matrix from BS to RIS in MISO system.
$h_{R_{n(i)}}$	Channel magnitude from BS to n^{th} RIS's i^{th} element in multi-RIS system.
$\tilde{h}_{R_{n(i)}}$	Complex channel from BS to n^{th} RIS in multi-RIS system.
$\tilde{\hbar}$	Complex channel from BS to i^{th} STAR-RIS element.
$\mathbf{H}_n$	Channel matrix from BS to the n^{th} RIS-user pair.
$\mathcal{J}$	Utility function of the system.
K	Number of Internet-of-Things (IoT) users.
K_1, K_2, K_3	Rician factors.
K_r or K_t	Power fraction for information receiver (IR) or energy receiver (ER).
L	Number of discrete phase shift (DPS) levels.
M	Number of RIS elements.

μ_k^2	Receiver noise power at the k^{th} user U_k in MISO system.
N	Number of RIS surfaces.
N_t	Number of BS antennas.
ν_1, ν_2, ν_3	Pathloss exponents.
ν_k^2	Receiver conversion noise power at the k^{th} user U_k in MISO system.
$\mathbf{o}$	Uniform Linear Array (ULA) response vector.
P_b	Transmitted BS power.
$\mathcal{P}_{\text{max}}$	Maximum BS power.
P_L	Large-scale total pathloss.
ϕ_i	Channel phase from BS to i^{th} RIS element.
ψ_i	Channel phase from i^{th} RIS element to user.
$\mathcal{R}_{th}$	Desired data rate threshold.
R_u	Data rate at the user.
s	Transmitted symbol.
$\mathcal{S}$	Set of discrete phase shift (DPS) values.
θ_i or θ_m	Phase shift of the i^{th} or m^{th} RIS element.
$\theta_{r,i}$ or $\theta_{t,i}$	Phase shift of the i^{th} reflection or transmission STAR-RIS element.
U_k	k^{th} IoT user.
$\varphi_{r,i}$ or $\varphi_{t,i}$	Channel phase from i^{th} STAR-RIS element to reflection or transmission side user.
ϖ, ω_{min}, κ	Practical phase shift model constants.

ϱ	Angle of arrival (AoA) or angle of departure (AoD).
w_e or w_r	Weights related to EH or data rate, respectively.
$\mathbf{w}_k$	Precoding vector of the N_t-antenna BS.
w_n	Additive white Gaussian noise (AWGN) at n^{th} RIS-user pair.
W_0^2	Cumulative noise power at user.
$\mathbf{x}$	Transmitted signal.
Ξ	Energy Efficiency of the system.
ξ_{th}	Desired harvested energy threshold.
y_k or y_n	Received signal at the k^{th} user or n^{th} RIS-user pair.
Z_n	Channel parameter of n^{th} RIS.
$\tilde{g}_{R_{n(i)}}$	Complex channel from n^{th} RIS's i^{th} element to single user in multi-RIS system.
$\tilde{h}_{r,_i}$ or $\tilde{h}_{t,_i}$	Complex channel from i^{th} STAR-RIS element to reflection or transmission side user.
$\mathbb{E}[\cdot]$	Expectation operator.
$(\cdot)^H$	Hermitian of a matrix.
$(\cdot)^{-1}$	Inverse of a matrix.
Tr$(\mathbf{A})$	Trace of matrix $\mathbf{A}$.
Rank$(\mathbf{A})$	Rank of matrix $\mathbf{A}$.
$\|\|\mathbf{a}\|\|$	Euclidean norm of vector $\mathbf{a}$.
diag$(\mathbf{A})$	Vector whose elements are the diagonal elements of $\mathbf{A}$.
$\mathbf{A} \succeq 0$	$\mathbf{A}$ is a positive semidefinite matrix.

$\sim$	Distributed as.
$\mathbb{C}^{x \times y}$	Space of $x \times y$ complex matrices.
$\arg$	Argument.
$\arg\max$	Argument of Maximum.
$\max$	Maximum.
$\min$	Minimum.
$\log(x)$	Natural logarithm function of x.
e^x or $\exp(x)$	Exponential function of x.

LIST OF PUBLICATIONS

Outcomes from Ph.D. Thesis Work

A1. In Refereed Journals

1. **N. Sharma**, M. B. Kokare, Swaminathan R., A. Kaushik, S. Chatzinotas, B. Ottersten, S. Gautam, "Energy Efficient RIS-assisted SWIPT-IoT Systems in Smart Agriculture", *IEEE Internet of Things Magazine*, vol. 9, no. 4, pp. 86-94, July 2026, doi: 10.1109/MIOT.2026.3676343.

2. **N. Sharma**, S. Gautam, S. Chatzinotas and B. Ottersten, "Power Optimization in RIS-assisted SWIPT-IoT System with Discrete Phase Shift," *IEEE Internet of Things Journal*, vol. 13, no. 11, pp. 22770-22786, June, 2026, doi: 10.1109/JIOT.2026.3665434.

3. **N. Sharma**, S. Gautam, S. Chatzinotas and B. Ottersten, "Fractional Programming Based Optimization Techniques for RIS-Assisted SWIPT-IoT System," *IEEE Communications Letters*, vol. 28, no. 12, pp. 2819-2823, Dec. 2024, doi: 10.1109/LCOMM.2024.3481289.

4. **N. Sharma**, S. Gautam, S. Chatzinotas and B. Ottersten, "Integrating Multiple RIS for Enhanced SWIPT-IoT Performance: Optimization Strategies," *IEEE Access*, vol. 12, pp. 182841-182855, 2024, doi: 10.1109/ACCESS.2024.3510886.

A2. In Refereed Conferences

1. **N. Sharma**, M. B. Kokare, Swaminathan R., and S. Gautam, "Maximizing Weighted Function in STAR-RIS Aided SWIPT-IoT with Discrete Phase Shifting," in *Proc. IEEE Vehicular Technology Conference (VTC2025-Spring)*, Oslo, Norway, 2025, pp. 1-5, doi: 10.1109/VTC2025-Spring65109.2025. 11174812.

2. **N. Sharma**, M. B. Kokare, Swaminathan R., and S. Gautam, "Distributed RIS SWIPT-IoT Systems: Optimizing Spectral Efficiency and Energy Harvesting," in *Proc. IEEE Wireless Communications and Networking Conference (WCNC)*, Milan, Italy, 2025, pp. 1-6, doi: 10.1109/WCNC61545.2025. 10978422.

3. **N. Sharma**, S. Gautam, A. Kaushik, S. Chatzinotas and B. Ottersten "Fractional Programming Strategy for Rate-Energy Optimization in RIS-assisted SWIPT IoT Networks," in *Proc. IEEE Global Communications Conference (GLOBECOM)*, Cape Town, South Africa, Dec. 2024, pp. 5126-5131, doi: 10.1109/GLOBECOM52923.2024.10901845.

4. **N. Sharma** and S. Gautam, "Optimization Strategy for RIS-Assisted SWIPT-IoTs with Non-Linear Energy Harvesting," in *Proc. 2024 National Conference on Communications (NCC)*, Chennai, India, 2024, pp. 1-6, doi: 10.1109/NCC60321.2024.10485849.

5. **N. Sharma**, S. Gautam, S. Chatzinotas and B. Ottersten, "On Optimizing RIS-aided SWIPT-IoTs with Power Splitting-based Non-Linear Energy Harvesting," in *Proc. IEEE Global Communications Conference (GLOBECOM)*, Kuala Lumpur, Malaysia, 2023, pp. 619-624, doi: 10.1109/GLOBECOM541 40.2023.10436799.

6. **N. Sharma** and S. Gautam, "Throughput Optimization for RIS-assisted SWIPT-IoTs with Hardware Impairments," in *Proc. 14th International Conference on Computing Communication and Networking Technologies (ICCCNT)*,
   Delhi, India, 2023, pp. 1-6, doi: 10.1109/ICCCNT56998.2023.10307124.

7. **N. Sharma** and S. Gautam, "Optimizing RIS-assisted Wireless Communication Systems with Non-Linear Energy Harvesting," in *Proc. International Conference on*

Energy, Power and Environment (ICEPE), pp. 1-6, 15th-17th June 2023, doi: 10.1109/ICEPE57949.2023.10201582.

A3. In Refereed Book Chapter

1. **N. Sharma**, S. Gautam, P. K. Upadhyay, S. Chatzinotas and B. Ottersten, "Spectrum Management for 6G RIS-SWIPT Systems," in *Intelligent Spectrum Management: Towards 6G , IEEE-Wiley*, 2025, pp.155-174, doi: 10.1002/9781394201235.ch6.

2. **N. Sharma**, S. Solanki, A. Kaushik, S. Gautam, P. K. Upadhyay, S. Chatzinotas, and B. Ottersten, "Semantic-Aware Resource Optimization Using Intelligent Algorithms," in *Semantic Communications for Next Generation Wireless Systems, IEEE-Wiley*, 2026. **(Under Review)**

Co-authored Publications during Ph.D.

B1. In Refereed Journals

1. P. K. Sharma, **N. Sharma**, S. Dhok, and A. Singh, "RIS-Assisted FD Short Packet Communication with NL-EH," in *IEEE Communications Letters*, vol. 27, no. 2, pp. 522-526, Feb. 2023, doi: 10.1109/LCOMM.2022. 3223286.

2. M. B. Kokare, **N. Sharma**, Swaminathan R., and S. Gautam, "Performance Analysis and Optimization of Full-Duplex RIS-Assisted SWIPT NTNs," submitted to *IEEE Journal on Miniaturization for Air and Space Systems*, 2026. **(Under Review)**

B2. In Refereed Conferences

1. M. B. Kokare, **N. Sharma**, Swaminathan R., S. Gautam, "Practical RRC-Based RIS-Assisted Full-Duplex UAV SWIPT Relaying for NTN," in *Proc. IEEE International Symposium on Personal, Indoor and Mobile Radio Communications-Workshops (PIMRC-Workshop))*, Singapore, Sept. 2026. **(Presented)**

2. M. B. Kokare, **N. Sharma**, Swaminathan R., and S. Gautam, "RIS-Integrated Full-Duplex UAV SWIPT Relaying for Next-Generation Non-Terrestrial Networks," accepted to *European Conference on Networks and Communications (EuCNC)*, Malaga, Spain, June, 2026. **(Presented)**

3. M. B. Kokare, S. Gautam, Swaminathan R., **N. Sharma**, A. Kaushik, and S. Chatzinotas, "Optimizing SWIPT in Multi-RIS aided V2I Networks: A Deep Learning Approach," in *Proc. IEEE International Conference on Communications (ICC)*, Montreal, Canada, 2025, pp. 6167-6172, doi: 10.1109/ICC52391. 2025.11161813.

4. M. B. Kokare, R. Mishra, **N. Sharma**, Swaminathan R., and S. Gautam, "Performance of Integrated Relay-RIS in UAV Systems: a Selection Combining Approach," in *Proc. National Conference on Communications (NCC)*, New Delhi, India, 2025, pp. 1-6, doi: 10.1109/NCC63735.2025.10983087.

5. E. N. S. S. Anjana, **N. Sharma** and S. Gautam, "RIS-assisted OFDM-based SWIPT System," in *Proc. 17th International Conference on COMmunication Systems and NETworks (COMSNETS)*, Bengaluru, India, Jan. 2025, pp. 507-513, doi: 10.1109/COMSNETS63942.2025.10885662.

6. N. Jadhav, **N. Sharma**, R. Dhaker, and S. Gautam, "AI/ML and Optimization Based Framework for SWIPT Systems Using Power-Splitting Protocol", in *Proc. 16th International Conference on Computing Communication and Networking Technologies (ICCCNT)*, Indore, India, 2025.

7. R. Dhaker, **N. Sharma**, N. Jadhav and Sumit Gautam, "ML-Driven Optimized Architecture for Time-Switching SWIPT Systems", in *Proc. 16th International Conference on Computing Communication and Networking Technologies (ICCCNT)*, Indore, India, 2025.

B3. In Refereed Book Chapters

1. M. B. Kokare, **N. Sharma**, Swaminathan R., and S. Gautam, "Integrated ISAC-RIS Systems for Next-Generation Connectivity Enhancement", in *Integrated Sensing and*

Communication for Sustainable Development Goals, 1st ed. Singapore: Springer, 2026, https://doi.org/10.1007/978-981-92-0209-6-2.

Chapter 1

Introduction

The International Mobile Telecommunications (IMT)-2020 usage scenarios for beyond 5G (B5G) communications include Enhanced Mobile Broadband (eMBB), Ultra-Reliable and Low Latency Communications (URLLC) and Massive Machine Type Communications (mMTC) [5]. These impact the prospect rapid digital transformation of agriculture, driven by the integration of advanced communication, sensing, and automation technologies aimed at improving productivity, sustainability, and operational efficiency [6]. Advanced Internet-of-Things (IoT) sensor nodes with embedded data analytics have made it possible to monitor crops, soil, temperature, weather and livestock in real time, enabling data-driven decision-making for better yield and resource management. The interconnection of millions of such sensor nodes is the main characteristic of the mMTC technology. Such techniques are expected to be cost effective and have a very low battery drainage. For the energy storage device to last over an year post installation in an IoT system, efficient power-saving solutions are desirable. However, existing wireless systems in rural and agricultural environments face inherent challenges such as intermittent connectivity, high device density, and limited power availability [7].

The concept of Energy Harvesting (EH) in Wireless Communication Networks repre-

sents an approach that enables the devices to replenish their batteries using external sources of energy present in the surrounding environment. Renewable energy sources like solar, wind, etc., are highly unpredictable and cannot be used for high Quality-of-Service (QoS) centric applications due to their dependence on favorable environmental conditions. In such a case, Simultaneous Wireless Information and Power Transmission (SWIPT) is a prudent EH solution, where the terminal node batteries are charged from the received electromagnetic (EM) radiations in a regulated manner [8]. Depending on the received RF power, energy conversion efficiency, and harvesting duration, SWIPT-enabled RF energy harvesting can accumulate harvested energy from the nanojoule to microjoule range, which is sufficient for many low-duty-cycle micro scale IoT devices employing modern ultra-low-power CMOS technologies [9, 10].

The emergence of joint Reconfigurable Intelligent Surfaces (RIS) and SWIPT offers a transformative solution to these limitations. RIS allows intelligent control over signal reflection, phase, and amplitude through programmable low cost metasurfaces. By adaptively adjusting these parameters, nearly passive RIS can direct, focus, and strengthen wireless signals toward target devices, improving coverage, reducing path loss, mitigating interference, and saving power [11]. In parallel, the SWIPT technology enables concurrent transmission of energy and information over the same radio frequency (RF) signals [12]. This capability allows the distributed IoT sensors, actuators, and communication nodes to harvest energy from the ambient RF environment while maintaining a continuous data exchange. The harvested energy can be used to power low-power sensors, communication modules, and even small-scale controllers, leading to self-sustaining, and a maintenance-free operation. The joint RIS-SWIPT framework thereby enables a ubiquitous coverage, enhanced energy sustainability, and long-term operational autonomy, which are critical requirements for the next-generation communication.

To proceed, we provide an overview of the problem statement and main motivation in Section 1.1, thesis objectives in Section 1.2 and major contributions in Section 1.3. A brief discussion regarding optimization tools used is given in Section 1.4. Finally, we provide details about the thesis organization and a chapter-wise summary in Section 1.5.

1.1 Problem Overview and Motivation

The emergence of 6G envisions a hyper-connected ecosystem, where billions of IoT devices operate seamlessly, particularly in remote and energy-constrained smart agricultural environments [7]. This intensifies the need for sustainable, energy efficient and reliable wireless communication system. SWIPT has evolved as a promising solution to prolong the lifetime of IoT device by enabling concurrent data transmission and EH [8]. However, the SWIPT system often suffers from severe performance degradation due to signal blockage and limited coverage in challenging propagation environment.

RIS has emerged as a transformative technology, controlling the propagation channel through its nearly passive elements by phase adjustments, to enhance the signal quality, coverage, and energy efficiency (EE) [13]. The advantages favor its integration with SWIPT-enabled networks [14]. Despite these advantages, RIS-SWIPT systems introduce significant challenges including, joint maximization of rate and energy, efficient resource allocation, RIS surface scalability, and robustness under imperfect channel state information (CSI). Furthermore, the reliance on ideal assumptions such as continuous phase shift (CPS) and linear EH model limits the practical applicability, necessitating realistic modeling with discrete phase shift (DPS), phase-dependent amplitude model for reflectivity and non-linear EH (NL-EH) behavior [15]. These challenges are further intensified with system advancements like multi-RIS, multi-antenna, multi-user and simultaneous transmitting and reflecting RIS (STAR-RIS), which demands joint active-passive beamforming and efficient solution for

highly coupled non-convex optimization problems [16], [17][18].

Motivated by the aforementioned challenges, this thesis focuses on developing optimization frameworks for RIS-assisted SWIPT-IoT systems, targeting the key performance metrics such as: data rate, harvested energy, EE, and transmit power. The work systematically investigates practical system model, including multiple RIS deployments with strategic selection schemes, RIS-user pairing, DPS constraints, and sigmoid function based NL-EH model. Subsequently, the RIS framework is extended to STAR-RIS for a full-space coverage by utilizing energy-splitting (ES) and mode switching (MS) protocols [19].

Through the application of advanced optimization techniques including alternating optimization (AO), fractional programming and convex relaxation methods, this thesis aims to bridge the gap between theoretical performance limits and practical constraints [20]. The insights derived from this work contribute to the robust design, scalable, and energy efficient next-generation wireless networks capable of supporting diverse IoT applications in the real-world environments.

1.2 Major Objectives of this thesis

The objective of this thesis is to explore and develop advanced optimization techniques to enhance the coverage, robustness, and overall performance of practically constraint RIS-assisted SWIPT-enabled IoT systems. The core objectives are listed as follows.

Objective 1: To design and optimize a multi-RIS assisted SWIPT-IoT system for enhanced performance.

Objective 2: To design and solve a fractional programming strategy for Rate-Energy (R-E) optimization in RIS-assisted SWIPT-IoT system with multiple RIS-user pair.

Objective 3: To design and solve a joint active-passive beamforming optimization in RIS-assisted SWIPT-IoT system with multiple users.

Objective 4: To design and optimize STAR-RIS aided SWIPT-IoT system.

The highlighted major contributions of the thesis will be discussed in next section.

1.3 Contributions and Main Highlights

In this thesis, we address several critical challenges, including low network coverage in the remote locations, limited operational lifetime of IoT devices, channel reliability issues, and constraints in resource allocation. To tackle these challenges, various system models are investigated encompassing multiple RIS deployments with selection strategies, RIS-user pairing, multi-user scenarios, multi-antenna systems with active beamforming, and practical RIS beamforming designs. These models are analyzed with the aim of optimizing key system parameters while maximizing or minimizing relevant performance metrics using advanced convex optimization techniques. All the designed system models involve practical sigmoid/logistic function based NL-EH analytical model. In this regard, a step-by-step highlights on main contributions of this work are provided in Fig.1.1. The summary of the principal contributions of this thesis are enumerated as follows.

Contribution I: The integration of multiple RIS units into SWIPT systems is studied in chapter 3. Three distinct objectives of data rate, EH and EE are maximized under the Time-Switching (TS) and Power-Splitting (PS) SWIPT protocols. Two types of RIS selection strategies, namely, exhaustive RIS approach (ERA), and optimal RIS approach (ORA), are analyzed and compared. The Karush-Kuhn-Tucker (KKT) conditions, alternating optimization-based algorithm, and fractional programming based Dinkelbach Transform is proposed to jointly optimize the TS or PS ratio and

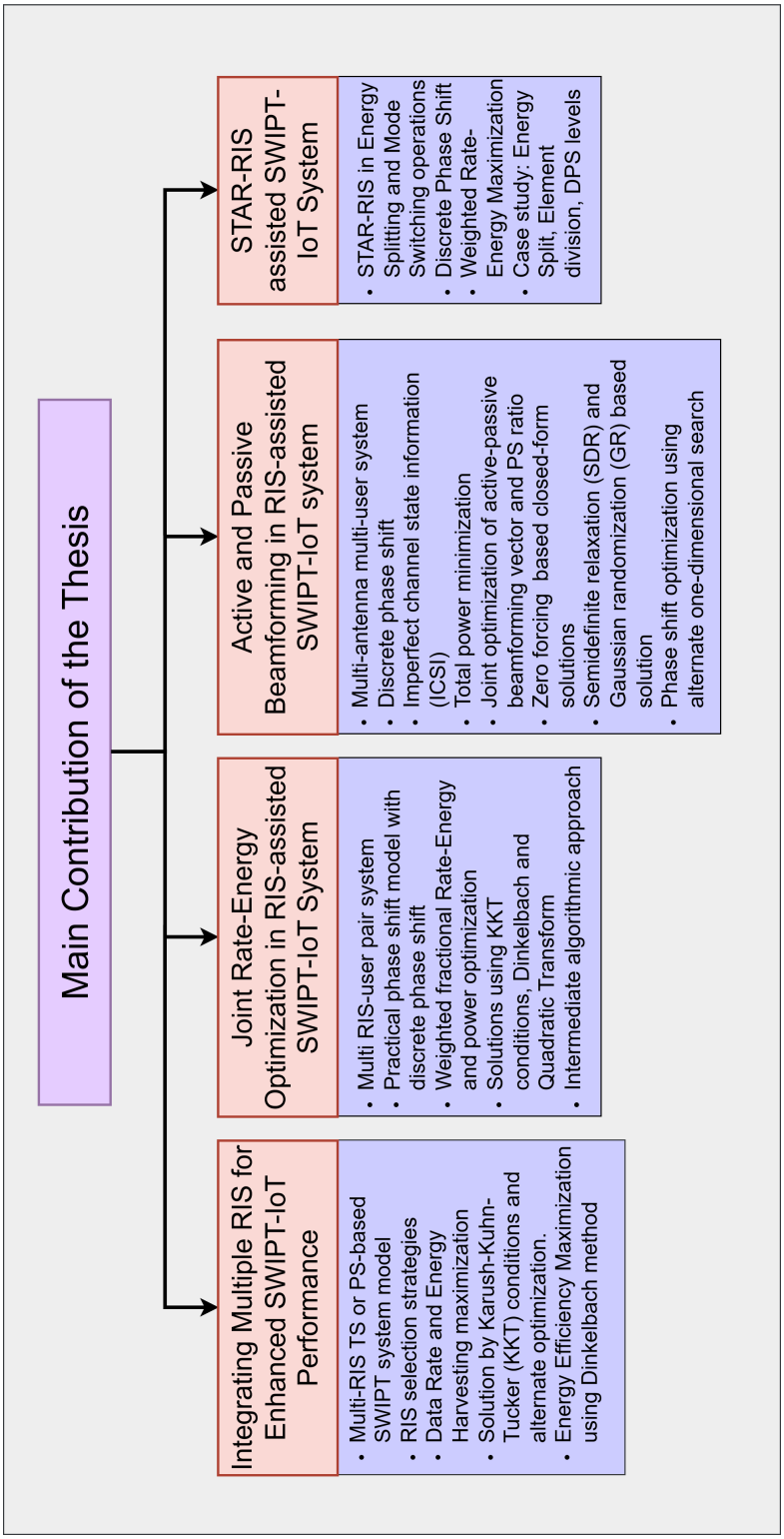


Figure 1.1: Main contributions of this thesis in a nut-shell.

the transmit power. Numerical simulations are conducted to evaluate the system performance highlight the R-E trade-off across different scenarios, considering factors such as surfaces count, element count, separation distance, EH and data rate demands. Additionally, the imperfect CSI is considered to analyze the performance of the proposed system.

Contribution II: The combination of conflicting metrics of data rate and EH in RIS-SWIPT systems is addressed in chapter 4 by introducing a weighted optimization objective, aiming to jointly maximize the fractional utility function of data rate, EH, and transmit power. This approach involves optimizing the PS ratios and transmit power under practical phase-dependent amplitude model for each RIS element reflectivity. To tackle these problems, fractional programming-based Dinkelbach and Quadratic transform algorithms are proposed and compared with KKT conditions based solutions. In addition, the impact of DPS on the RIS model is analyzed too. Numerical results show that deploying more RIS elements and placing them closer together enhances both the information rate and EH, whereas performance nearly saturates with incremental DPS levels.

Contribution III: Considering a smart farming scenario, the integrated RIS-SWIPT system is extended to support multi-antenna and multiple IoT users for enhanced coverage with the corresponding performance is presented in chapter 5. Temperature and moisture sensors use the PS-SWIPT protocol, while RIS performs passive beamforming with hardware-constrained DPS. We intend to minimize the transmit power by optimizing transmit beamforming, the RIS phase shift matrix, and the PS

factor under QoS constraints. The developed complex non-convex sub-problems are addressed using two methods: (i) a sub-optimal Zero-Forcing (ZF) approach, and (ii) an optimal solution based on Semidefinite Relaxation (SDR) with Gaussian Randomization (GR). An alternate one-dimensional search strategy is used for RIS phase shift optimization. The resulting sub-problems are iteratively solved through an Alternating Optimization (AO) approach. Finally, the numerical simulations validate the proposed framework in terms of performance and convergence. The results demonstrate robustness under imperfect channel state information (ICSI) and varying system parameters for next-generation IoT-enabled smart farming use-case.

Contribution IV: The limited half-space coverage of the reflect-only RIS is considered as an extension in chapter 6, wherein we introduce the STAR-RIS. In this work, we examine the STAR-RIS assisted SWIPT-IoT network for ES and MS operational mode, serving the Energy Receiver (ER) and Information Receiver (IR). For the considered DPS STAR-RIS reflectivity model, we aim to maximize the Weighted Rate-Energy (WRE) function, with certain QoS constraints by optimizing power parameters. An AO algorithm solves the complicated WRE maximization problem. Numerical results highlight the impact of varying the energy split ratio and element division on the performance, with the critical selection of DPS level (quantization bits) balancing device's bulkiness (phase control bits) and system efficiency.

1.4 Discussion on Optimization Problems and Techniques

Optimization techniques have become an essential mathematical tool for the design and analysis of modern wireless communication systems. Since, wireless communication sys-

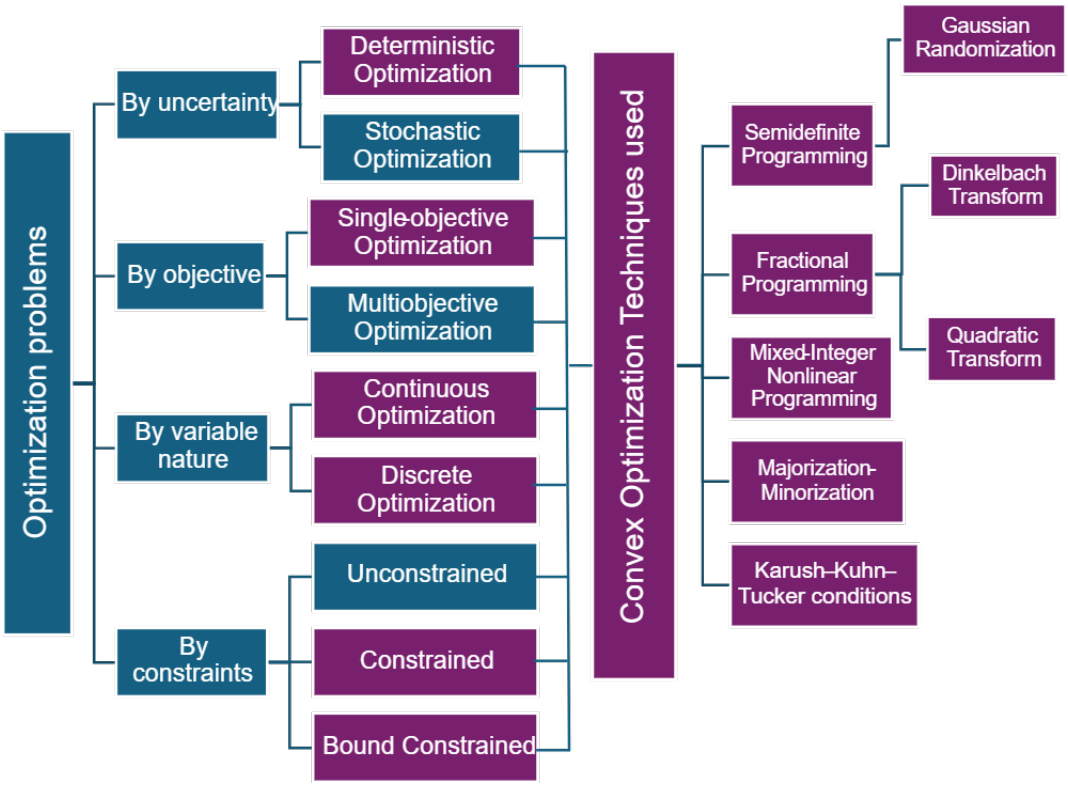


Figure 1.2: Taxonomy of optimization problems and list of convex optimization techniques used in this thesis.

tems involve multiple interacting parameters, optimization frameworks help in obtaining the best possible operating conditions under the given system limitations.

An optimization problem aims to determine the optimal values of decision variables that maximize or minimize a desired system performance metric while satisfying all the practical system constraints. It generally consists of an objective function, optimization variables, and a set of constraints, detailed as follows.

- **Objective Function:** The objective function represents the system performance metric that is required to be optimized. Depending on the communication protocols, the objective may involve either maximization or minimization of a function comprising certain performance parameter or a combination of several parameters together.

- **Optimization Variables:** These are referred to as decision variables or unknown

parameters, which represents the system parameters whose optimal values are determined during the optimization process.

- **Constraints:** These are the conditions (strict or relaxed) that must be met by the optimized solution. In other words, constraints define the feasible region of the optimization problem and impose practical limitations on the optimizing variable.

Following step in the optimization process is to identify the type of optimization problem, which help in seeking a tractable solution. To be specific, Fig. 1.2 gives a broad taxonomy of the various optimization problem categories. The specifically used optimization techniques in this thesis are explicitly marked in magenta. The final stage of the optimization framework involves employing suitable optimization techniques to obtain the desired solution. Subsequently, the obtained solution is validated via simulations and implementation using appropriate computational tools and software platforms like MATLAB©, Python and CVX©. Various optimization methods employed in this thesis for solving different categories of optimization problems are briefly discussed in Appendix A.

1.5 Organization of the thesis

This thesis is organized into seven Chapters. The title and short summary of the Chapters are structured as follows.

Chapter 1 (Introduction)

A comprehensive overview of the topic is presented herein, highlighting the motivations behind various problem formulations. Comprehensive chapter-wise objectives are discussed, followed by a brief summary of the major contributions of this work.

Chapter 2 (Review of RIS-SWIPT Systems)

This chapter presents an overview of the RIS-assisted SWIPT systems for future

Energy-Efficient IoT communications. Emerging RIS architectures such as STAR-RIS, BD-RIS, and hybrid active-passive RIS are discussed along with their advantages over conventional reflect-only RIS. The fundamentals and operational protocols of SWIPT are also reviewed. Furthermore, RIS-SWIPT integration is illustrated for improving coverage, spectral efficiency, EH, and communication reliability. A smart agriculture case study demonstrates the applicability of RIS-SWIPT for sustainable large-scale IoT deployments. The insights obtained from this chapter serves as the foundation for the RIS-assisted SWIPT-IoT frameworks developed in the subsequent Chapters of this thesis.

Chapter 3 (Integrating Multiple RIS for Enhanced SWIPT-IoT Performance)

In this chapter, we investigate a half-duplex SWIPT-enabled multi-RIS communication framework with two RIS utilization schemes, namely the ERA and ORA, analyzed under the TS and PS SWIPT architectures for achievable rate, EH, and EE optimization problems. Closed-form KKT solutions, alternating optimization, and Dinkelbach-based approaches are respectively developed and comparatively evaluated. The study highlights the benefits of intelligent RIS selection, increased RIS deployment, higher transmit power, and reduced communication distance in improving system performance. Finally, the imperfect CSI analysis confirms the robustness of the proposed framework.

Chapter 4 (Joint Rate-Energy Optimization in RIS-assisted SWIPT-IoT System)

This chapter evaluates a practical multiple RIS-user paired communication system employing PS-SWIPT with phase shift dependent RIS reflection amplitude. A unified utility function considering achievable rate, harvested energy, and transmit power consumption is optimized under QoS constraints. The KKT, Dinkelbach transform,

and Quadratic Transform based approaches are developed and comparatively analyzed, where the Dinkelbach method exhibited the fastest convergence performance. The study also validates the inherent R-E tradeoff in SWIPT systems and demonstrates that system performance improves with higher RIS elements, larger transmit power budgets, and shorter communication distances. Additionally, the impact of DPS resolution on RIS implementation complexity is highlighted.

Chapter 5 (Active and Passive Beamforming in RIS-assisted SWIPT-IoT System)

Herein, we discuss an RIS-assisted multi-input single-output (MISO) PS-SWIPT framework for supporting multiple IoT-enabled users in smart farming applications. A joint optimization framework for active beamforming, passive beamforming, and PS ratios is developed for the minimized transmit power with RIS quantized phase shift constraints. The strongly coupled complex optimization optimization problem is solved using ZF, SDR, GR, and alternate search-based optimization techniques within an AO framework. The numerical results demonstrate that the proposed framework effectively minimizes the transmit power while preserving as well as maintaining the robust system performance under ICSI and diversified network conditions including RIS element number, user densities, discrete levels of DPS, and signal-to-interference-plus-noise ratio (SINR) targets.

Chapter 6 (STAR-RIS assisted SWIPT-IoT System)

This chapter explores the STAR-RIS assisted SWIPT framework to evaluate the maximization of Weighted Rate and Energy metric with DPS based STAR-RIS phase model. Both ES and MS operational protocols are considered, where the selection depends on the reflection and transmission region's parameters. Consequently, the selection of the energy split ratio and STAR-RIS element allocation is essential for sys-

tem performance. Numerical results present the effective WRE improvements with increasing STAR-RIS element count, higher transmit power budgets, more resolution of DPS levels and superiority of STAR-RIS SWIPT system than the conventional reflect-only RIS architecture.

Chapter 7 (Conclusion and Future Directions)

In this chapter, we summarize the major conclusions of the thesis, and also outline potential directions for future research.

In this chapter, we have introduced problem statement and motivation behind carrying out this research. In subsequent Chapters, we discuss the RIS-assisted SWIPT-IoT systems in detail along with their corresponding analyses, respectively.

Chapter 2

Review of RIS-SWIPT Systems

Reconfigurable Intelligent Surface (RIS)-assisted Simultaneous Wireless Information and Power Transmission (SWIPT) has emerged as promising paradigm for enabling energy-efficient and sustainable wireless communication system for future sixth-generation (6G) enabled Internet-of-Things (IoT) networks. This chapter presents a comprehensive review of RIS-SWIPT system by discussing the fundamentals of RIS architecture, SWIPT receiver schemes, and practical Energy Harvesting (EH) models. Various RIS variants including Simultaneous Transmitting and Reflecting RIS (STAR-RIS), hybrid active-passive RIS and beyond diagonal RIS (BD-RIS) are examined with an emphasis on operational protocols and potential advantages. This chapter further depicted two basic RIS-SWIPT systems employing the time-switching (TS) and power-splitting (PS) SWIPT protocols, respectively, followed by the IoT user. SWIPT-RIS integration is advocated for enhanced spectral efficiency, coverage, EH capabilities and robust propagation environment. Finally, a use case of RIS-assisted SWIPT-IoT for smart agriculture is presented across multiple agricultural domains including smart farming, livestock tracking, storage management, and agri-logistics. It enables sustainable wireless communication, monitoring and action oriented future agricultural networks.

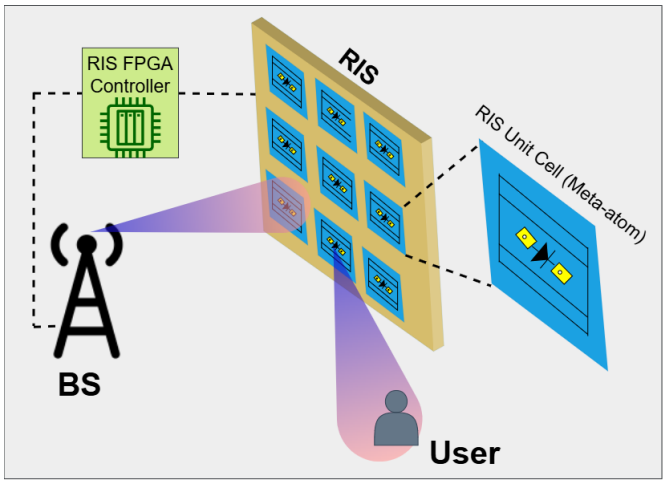


Figure 2.1: Basic structure of RIS.

The chapter is organized as follows. Section 2.1 provides an introduction to RIS and its variants. Section 2.2 describes SWIPT and various associated EH models. In Section 2.3, we present basic SWIPT-RIS system models. The case study related to smart agriculture is scripted in Section 2.4. The chapter finally rests with summary in Section 2.5.

2.1 Reconfigurable Intelligent Surfaces (RIS)

The notion of RIS refers to an upcoming technology in the realm of next-generation Wireless Communications [21]. This innovative solution offers numerous benefits including coverage, enhanced spectral efficiency, improved energy efficiency (EE), and reduced cost [22]. It is composed of multiple reflecting elements constructed with near-passive electromagnetic meta-material. The RIS has capabilities of controlling the scattering environment in a way that the electromagnetic wave impinging on its elements can be steered into desired direction. This is done by configuring each element's phase shift, reflectivity, directivity, and other related relevant parameters, with external stimuli circuit consisting of PIN diode, FPGA, microcontroller, etc., as shown in Fig. 2.1 [13, 23].

The debate concerning the already existing relay technology and the upcoming paradigm of RIS is poised more towards the fact that for high-rate transmissions scenarios, nearly-passive RIS can surpass the decode-and-forward (DF) relay considering the EE aspect. Additionally, the RIS elements require considerably lower power compared to the active relays. Though very large sized RIS are anticipated to increase the signal-to-noise ratio (SNR), the energy consumption for configuring phase shifts of each element cannot be ignored either. Moreover, the efficacy of RIS may notably be reduced by the hardware impairments like e.g., restricted resolution due to phase shift. A variant of RIS named as STAR-RIS, can perform transmission and reflection in two directions, fulfilling both the concerned half-spaces [17]. RIS too finds its application in the underwater, underground, industrial and disaster environments. In this context, there is a significant propagation loss due to electromagnetic wave absorption and heavy scattering, resulting in a poor signal strength at the receiver. RIS with its high directivity and passive beam forming works as a healer for such predicaments [24].

2.1.1 RIS and its variants

Technological advancements have extended reflect-only RIS to STAR-RIS and similar variants, as discussed below.

2.1.1.1 Reflect-only RIS

The conventional RIS can reflect the incident signals to serve the users/devices on the same side and covers only the half wave space. This reflect-only RIS is made up of numerous configurable meta-material elements on the opaque substrate, visualized as equally spaced chips arranged on a metal plate.

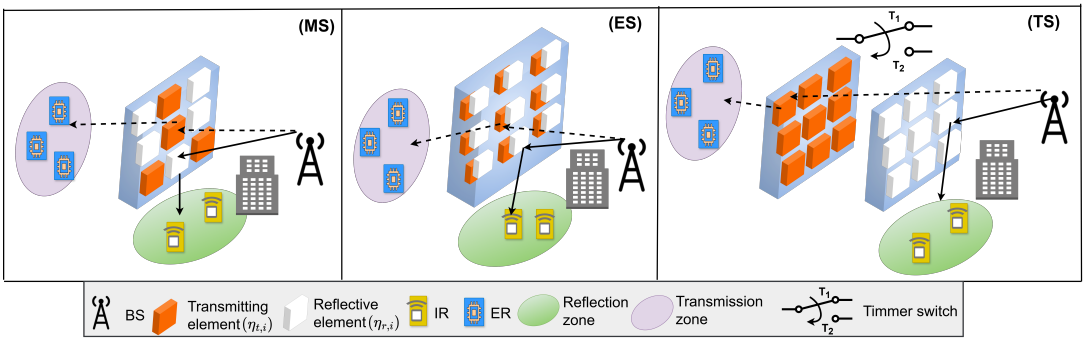


Figure 2.2: STAR-RIS operates via three main protocols, mode switching (MS), energy splitting (ES), and time switching (TS); serving the information receivers (IRs) in the reflection zone as well as energy receivers (ERs) in the transmission zone.

2.1.1.2 STAR-RIS

The π (half-space) coverage of reflect-only RIS can be extended to 2π (full-space) in the 2-D regime, by introducing STAR-RIS which can serve IoT devices not only on the same side (reflection side) but also on the transverse side (transmitting side). The STAR-RIS elements submerged in transparent substrate, can be visualized as ice-cubes in a glass of water (e.g., DOCOMO's smart glass) [11]. While several other patch-array based protocols exist in the literature, STAR-RIS operates using three protocols: energy splitting (ES), mode switching (MS), and time switching (TS), as illustrated in Fig. 2.2. In the ES mode, the incident energy on each element is split for transmission and reflection operation, identified by their respective coefficients guiding the split. Concerning the MS mode, each element is chosen to perform either reflection or transmission operation solely, but not both. In TS, complete STAR-RIS with all its elements can be reflect-only in one time frame while transmit-only in another frame. A detailed STAR-RIS communication system model will be studied in chapter 6. A similar variant to STAR-RIS is the Intelligent Reflecting and Refracting Surfaces (IR^{2}S), distinguished by providing decoupling of reflection and refraction operations, and providing individual control by exploiting the physical properties of an individually specific element [25]. Another variant is the multi-functional RIS (MF-

RIS) architecture, which overcomes the limitation of single operation RISs (reflect/transmit only RIS) by harvesting energy from RF signals to support the simultaneous reflection, refraction/transmission, and amplification of incident signals [26]. In the context of smart agriculture, STAR-RIS is well suited for low-power IoT deployments requiring dual-sided coverage, whereas MF-RIS is more appropriate for self-sustainable and data-intensive applications owing to its EH and signal amplification capabilities at the cost of higher hardware complexity.

2.1.1.3 Hybrid Active-Passive RIS

Hybrid RIS is comprised of both active and passive elements, to mitigate the signal attenuation and improved EE [11]. The fewer active elements are capable of signal processing for channel state information (CSI) estimation and amplifying the signal, while the majority of passive elements continue to give cost and power advantages. Autonomous RIS has multiple unit cells (UCs), in which a portion of the UCs is dedicated to beam steering, while the remaining UCs operate in energy-absorbing mode for EH from the incident signals. This clustering can be optimized for energy efficient system.

2.1.1.4 Beyond Diagonal RIS (BD-RIS)

Extensive research focus has been directed towards the utilization of traditional RIS employing diagonal phase shift matrices, such that there is no interconnection between the RIS element and they are independently connected to its ground load. The conventional RIS architecture restricts its ability to manipulate passive beamforming, therefore some researchers have analyzed the BD-RIS thus far [27]. The BD-RIS offers greater flexibility in manipulating both diagonal and non-diagonal elements of the scattering matrix, significantly enhancing the performance in various wireless systems. Consequently, while

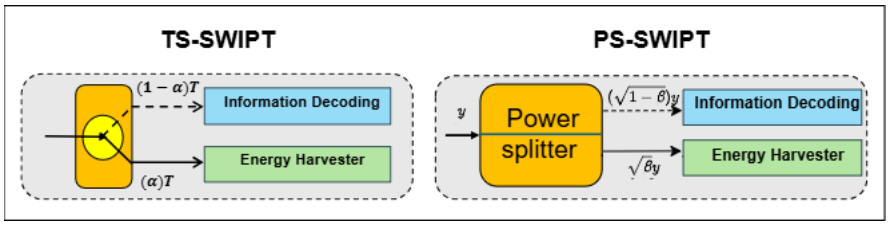


Figure 2.3: The TS and PS-SWIPT receiver architecture.

considering the RIS to have discrete values, BD-RIS provides increased proficiency. Even though, the conventional RIS covers only the half-space, the BD-RIS utilizing appropriate group-connected reconfigurable impedance network and antenna array arrangement can support the hybrid and multi-sector modes to realize a full-space coverage. It has advantages for simplifying practical deployments and enhancing the overall spectral efficiency. After counting for various advantages of the BD-RIS, it has greater issues from the viewpoints of equipment deployment, structural planning, RF deficiencies, signal analysis, and wideband modeling.

2.2 Simultaneous Wireless Information and Power Transmission (SWIPT)

SWIPT is regarded as a promising technology for sustainable (green) wireless communications because it enables the simultaneous transmission of information and energy using the same RF waveform, thereby improving spectrum utilization and reducing the dependence of energy-constrained IoT devices on batteries [8]. Although its end-to-end RF energy transfer efficiency is limited by propagation losses and RF-to-DC conversion efficiency, SWIPT can extend the operational lifetime of low-power sensor nodes, reduce battery replacement frequency, and lower the associated environmental impact, making it an attractive solution for sustainable IoT networks [28]. There exists four SWIPT approaches

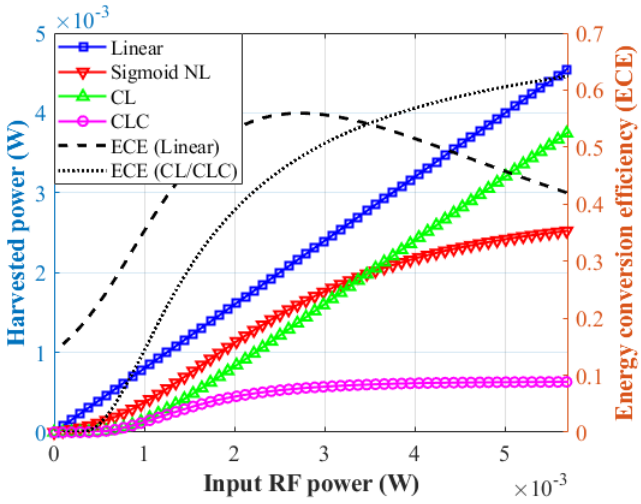


Figure 2.4: Power harvested by various models along with the energy conversion efficiency.

depending upon time, power, antenna, and space domain for signal switching between information decoding (ID) and EH. Out of the several existing architectures, TS and PS are widely adopted in the literature from an investigation viewpoint [29]. In the TS protocol, the overall time slot is divided between ID and EH. While in PS protocol, the received signal power is being split for the SWIPT operation. TS-SWIPT has benefit pertaining to higher SNR and simpler hardware architecture, whereas PS-SWIPT with complex receiver works perfectly for applications with data, EH, and delay constraints [8]. The receiver architecture for both the protocols are depicted in Fig. 2.3.

2.2.1 Energy Harvesting (EH) Models

After several decades of research in the field of wireless radio frequency (RF) power transfer, it is evident that the backbone of all the EH circuits is the rectenna, composed of an antenna and a rectifier. The standard approach involves converting the incoming wireless RF signal into a DC equivalent, using single or multiple diodes. These series of diodes introduces non-linearity to the system operation. It is crucial to closely or exactly model the non-linearity in the EH circuit, especially concerning SWIPT. The literature is served

Table 2.1: Comparison of existing literature and present work.

EH Model	**Harvested Power Expression**
Linear	$P_{lin}(P_{in}) = \zeta_{lin} P_{in}$
Constant Linear	$P_{CL}(P_{in}) = \begin{cases} 0, & P_{in} \in [0, P_{sen}) \\ \zeta_{CL}\left(P_{in} - P_{sen}\right), & P_{in} \in [P_{sen}, \infty] \end{cases}$
Constant-Linear-Constant	$P_{CLC}(P_{in}) = \begin{cases} 0, & P_{in} \in [0, P_{sen}) \\ \zeta_{CLC}\left(P_{in} - P_{sen}\right), & P_{in} \in [P_{sen}, P_{sat}) \\ \zeta_{CLC}\left(P_{sat} - P_{sen}\right), & P_{in} \in [P_{sat}, \infty] \end{cases}$
Sigmoid based non-linear	$P_{NL} = \frac{E'}{1-\chi}\left(\frac{1}{1+\exp\left(-aP_{in}+ab\right)} - \chi\right)$

with various types of linear and approximated non-linear type models listed in Table 2.1 and plotted in Fig. 2.4 [30, 31]. The detailed mathematical expressions are given as follows.[1]

- **Linear EH model:** The linear EH model stands out as the most basic and commonly employed in a significant portion of literature related to SWIPT. It expresses the harvested power as a linear function of input RF power (P_{in}) in the following manner

$$P_{lin} = \zeta_{lin} P_{in}, \tag{2.1}$$

  where $\zeta_{lin} \in (0, 1]$ is the constant energy conversion efficiency (ECE) of the linear EH receiver. The non-practicality of linear model is acknowledged by subsequent models.

- **Constant-Linear EH model:** The Constant-Linear (CL) model considers the sensitivity of the receiver (P_{sen}), a threshold below which RF conversion does not occur,

[1]Here, we use power and energy as interchangeable terms considering unit time.

given by

$$P_{CL} = \begin{cases} 0, & P_{in} \in [0, P_{sen}), \\ \zeta_{CL}(P_{in} - P_{sen}), & P_{in} \in [P_{sen}, \infty), \end{cases}$$

where $\zeta_{CL} \in (0, 1]$ is the fixed ECE of the CL-EH receiver. This model lacks in considering the input power saturation.

- **Constant-Linear-Constant EH model:** The Constant-Linear-Constant (CLC) model considers the sensitivity of the receiver (P_{sen}) as well as saturation power level (P_{sat}) represented as

$$P_{CLC} = \begin{cases} 0, & P_{in} \in [0, P_{sen}), \\ \zeta_{CLC}(P_{in} - P_{sen}), & P_{in} \in [P_{sen}, P_{sat}), \\ \zeta_{CLC}(P_{sat} - P_{sen}), & P_{in} \in [P_{sat}, \infty). \end{cases}$$

  In between the saturated and sensitivity power levels ($P_{sat} - P_{sen}$), linear operation of RF conversion is carried with a conversion efficiency of $\zeta_{CLC} \in (0, 1]$.

- **Non-Linear EH model:** The sigmoid/logistic function based non-linear (NL) EH model truly replicates NL behaviour of diodes, it is given by [32]

$$P_{NL} = \frac{E'}{1 - \chi} \left(\frac{1}{1 + \exp(-aP_{in} + ab)} - \chi \right), \tag{2.2}$$

  where $\chi = (1 + exp(ab))^{-1}$ guarantees a zero input for a zero output in the model. E' is the circuit's saturation point, a and b are related to the circuit's capacitor and diode turn-on voltage, respectively. A curve-fitting tool is used to analyze the experimental data and to find the values of the constant parameters (E', a, b) [32, 33].

Note: A different nomenclature is adopted by some authors while mentioning CLC model

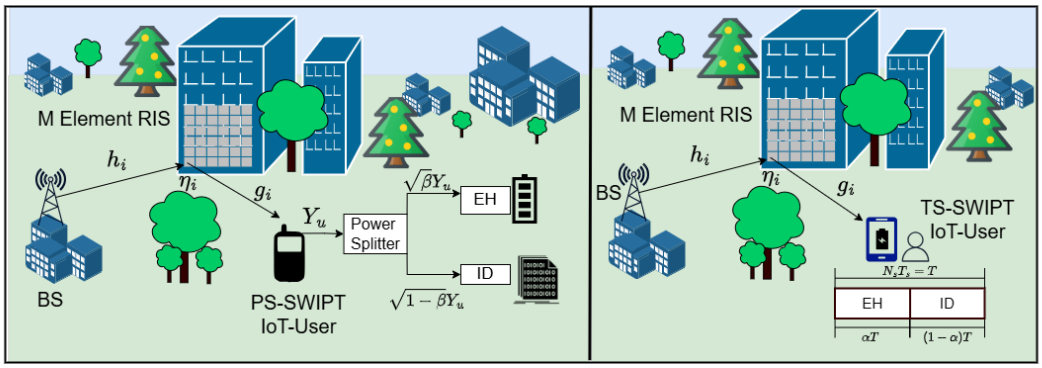


Figure 2.5: Basic system model for SISO RIS-assisted SWIPT-IoT system, considering PS-SWIPT and TS-SWIPT user receiver.

as NL or piece-wise NL model [34, 35, 36, 37]. However, we shall restrict our discussion to sigmoidal function based NL-EH model in this chapter and for the remainder of this thesis.

Figure 2.4 sketches the NL nature of ECE for the above mentioned models, i.e., $\zeta_k \forall k \in [lin, CL, CLC]$. ECE is considered to be a constant value for linear, CL and CLC models, which is not practical due to the non-linearity of circuits [38].

2.3 Amalgamation of RIS and SWIPT

In the conventional SWIPT systems, the performance is severely affected by the propagation losses, blockage effects and the conflicting requirements between the information rate and harvested energy. RIS effectively addresses these issues by intelligently reconfiguring the channel propagation environment through adjustable phase shifts of its reflector elements. By coherently combining the signal at the intended receiver, RIS enhances the received signal strength, thereby increasing the overall spectral efficiency and EH capabilities.

Correspondingly, the dual combination of SWIPT and RIS results in increased data transmission rates and coverage extension owing to its near-passive nature, while keeping the power consumption in check [8]. Specifically, the signal-to-noise ratio (SNR) of

information receivers (IRs) is enhanced via constructive reflection by the RIS, thereby reducing the outage probability. Concurrently, the focused beamforming capabilities increase the incident RF power at the energy receiver (ER), enabling efficient EH at the low-power IoT devices and sensor nodes. In the same context, Fig. 2.5 depicts the system model of a basic single-input single-output (SISO) RIS-assisted SWIPT-IoT system, considering block transmission of N_s transmitting symbols per block from BS for time duration $T = N_s T_s$ (seconds), where T_s is the symbol period. For PS-SWIPT, the received signal y is divided into two parts. A fraction of $\sqrt{\beta}y$ is used for EH, and remaining part of the received signal $\sqrt{1-\beta}y$ is used for ID. Here, β represents the PS factor. For TS-SWIPT, each block is divided into two phases of αT and $(1-\alpha)T$ duration. We define time switching (TS) factor as $\alpha \in [0, 1]$. The advanced system configuration with detailed analysis on system performance under strict constraints will be studied in the upcoming Chapters.

The integration of RIS with SWIPT also improves fairness among the users by enabling an optimized allocation of reflected energy and information beams according to channel conditions and Quality-of-Service (QoS) requirements. Through the joint optimization of transmit beamforming, power allocation, and RIS phase shifts, a desirable trade-off between the harvested energy and achievable rate is realized. Such capability becomes highly relevant for emerging 6G applications involving smart agriculture, intelligent transportation, industrial automation, and massive IoT networks, where sustainable operation of battery-constrained devices is a critical requirement.

2.4 Case Study: Smart Agriculture

Fig. 2.6 describes the smart agriculture use case, majorly divided into four subsystems: (i) advanced farming, (ii) animal husbandry, (iii) storage management, and (iv) agri-logistics. In each subsystem, the IoT sensor's data is transmitted through Wireless Sen-

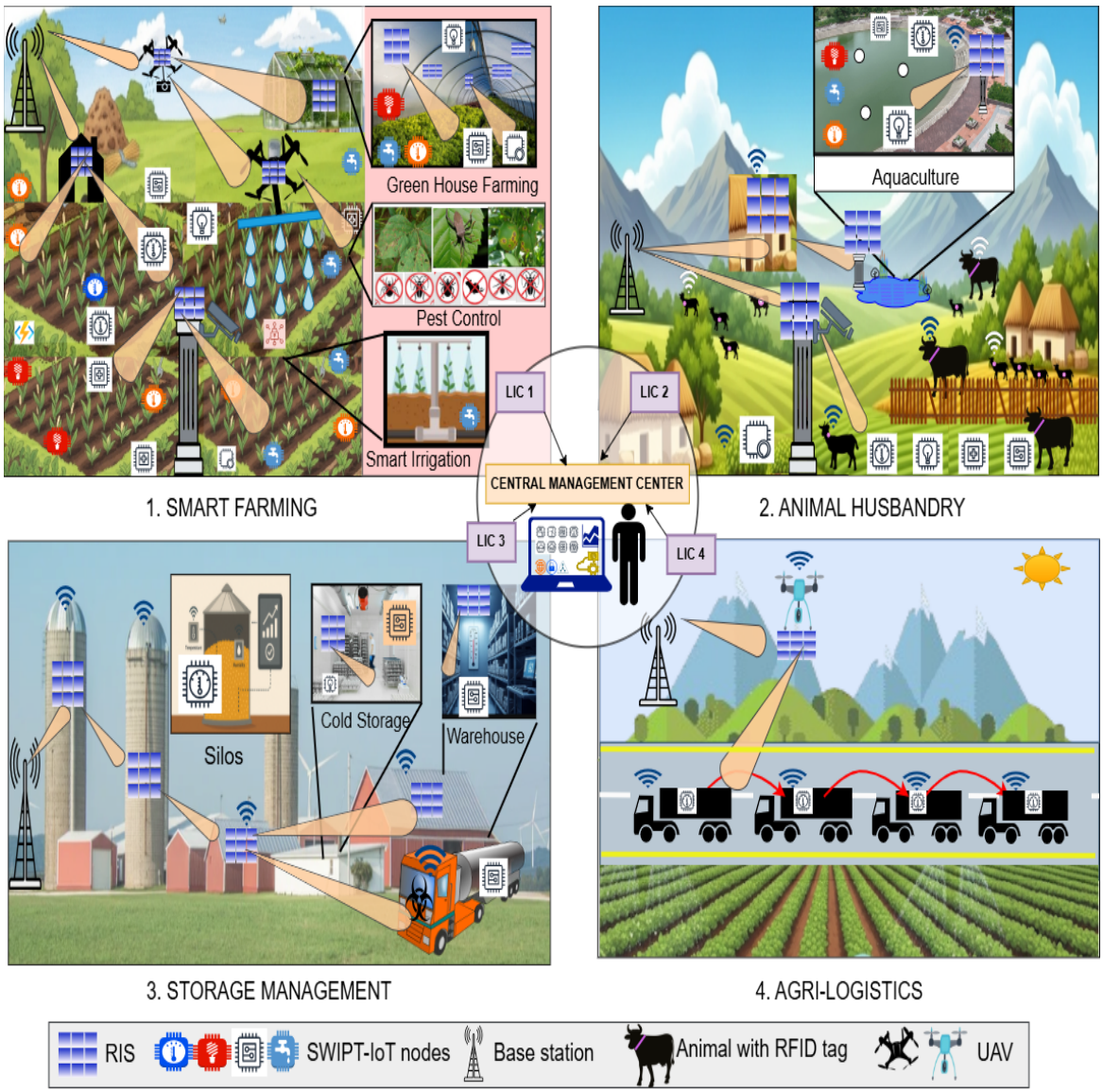


Figure 2.6: Identified areas of agriculture: advanced farming, animal husbandry, storage management and agri-logistics, with the showed impact of RIS-SWIPT in improving coverage and saving energy.

sor Networks (WSNs) to the local information centers, processed, and then forwarded to a central management center for optimized decision-making, which is controlled by the farmer [39]. To enable large-scale smart agriculture, numerous WSNs are needed, causing high energy consumption and signal degradation. To address this issue, RIS-assisted and SWIPT-enabled WSNs are proposed, wherein the RIS enhances the overall coverage and transmission efficiency by reflecting the signals toward SWIPT-IoT sensor nodes, which simultaneously harvest energy from RF signals for sustainable data transmission. This approach ensures energy-efficient, reliable, and green communication for smart agriculture. In the subsequent section, we assess *how and where can the integration of SWIPT-RIS be optimized to achieve energy-efficient and sustainable green communication in smart agriculture systems ?*

2.4.1 Advanced Farming

By strategically deploying the RIS units on poles, silos, nearby infrastructure, greenhouse panels, and irrigation sensors, the wireless environment can be reconfigured to provide uniform coverage maintaining a continuous field monitoring by SWIPT-IoT nodes despite physical obstructions over extended ranges. The inaccessible nodes are served by an Uncrewed Aerial Vehicle (UAV) integrated with RIS as well. Concurrently, SWIPT allows these energy-constrained devices to harvest power from RF signals, reducing dependence on batteries, solar panels, and wired connections. As a result, RIS-SWIPT based smart farming supports consistent crop yield and resource efficiency. It also supports adaptive irrigation scheduling, preventing over-watering or drought stress, while conserving water and energy resources. Moreover, the autonomous pest detection network enables targeted pesticide application, reducing the chemical usage and preventing crop damage.

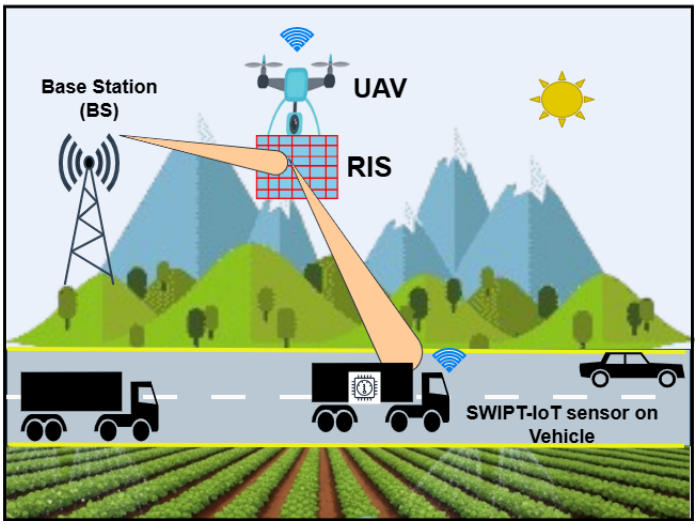


Figure 2.7: Integrated V2I-UAV-assisted communication system employing an RIS for enhanced coverage between a BS and a vehicle equipped with SWIPT-IoT sensor. The UAV positioned at a height performs EH to support its operation.

2.4.2 Animal Husbandry Management

RIS panels on barns, fences, poles, and aerial platforms dynamically direct energy to mobile livestock, ensuring reliable communication with wearable IoT devices. SWIPT enables RF-EH, while RIS acts as transceiver in integrated sensing and backscatter communication (ISABC) systems to alleviate the energy constraints of IoT sensors in tracker and to enable non Line-of-Sight (NLoS) sensing [40].

2.4.3 Storage Management

The integrated SWIPT-RIS system supports reliable monitoring of storage conditions, automatic ventilation or cooling adjustments, and reduced wastage, thereby improving food preservation and operational efficiency in post-harvest management.

2.4.4 Agri-logistics Monitoring

RIS-assisted Vehicle-to-Infrastructure (V2I) communication, integrated with SWIPT-enabled IoT nodes, can dynamically shape and direct wireless signals between moving vehicles, RIS-embedded UAVs, and roadside units, as illustrated in Fig. 2.7. This ensures uninterrupted tracking, condition monitoring, and real-time data exchange, thereby enhancing traceability, operational efficiency, and quality control throughout the agricultural supply chain [41]. Furthermore, Integrated Sensing and Communication (ISAC) optimizes the resource utilization by performing joint sensing and communication.

2.5 Summary

In this chapter, we provided a review on the evolution and integration of RIS and SWIPT technologies directed towards realizing energy efficient and intelligent Wireless Communication system for future IoT applications. The fundamentals of emerging RIS evolutions including STAR-RIS, BD-RIS, and hybrid active-passive RIS were discussed highlighting the differential improvement with respect to reflect-only RIS. Moreover, the importance of SWIPT and its operational protocols are highlighted. The RIS-SWIPT integration through a simple system model with TS-based and PS-based SWIPT-IoT has been demonstrated for enhanced coverage, spectral efficiency, EH capabilities, and communication reliability. A case study related to the RIS-assisted architecture with SWIPT-enabled IoT devices is proposed as a unified and energy-efficient solution for large-scale agricultural deployments, encompassing precision farming, agri-logistics, livestock monitoring, and storage management. This enables reliable, green, and self-sustaining wireless sensing and monitoring system. Based on some major insights from this chapter, we intend to develop the RIS-assisted SWIPT-IoT framework in the succeeding parts of this thesis.

Chapter 3

Integrating Multiple RIS for Enhanced SWIPT-IoT Performance

In this chapter, we study the integration of multiple Reconfigurable Intelligent Surfaces (RIS) units into Simultaneous Wireless Information and Power Transmission (SWIPT) enabled systems. We aim to optimize the performance of multi-RIS assisted SWIPT-IoT systems, focusing on maximizing three distinct objectives of data rate, energy harvesting (EH) and energy efficiency (EE), under Time-Switching (TS), and Power-Splitting (PS) SWIPT protocols. Herein, two types of RIS selection strategies, namely, exhaustive RIS approach (ERA), and optimal RIS approach (ORA) are analyzed, and compared. The Karush-Kuhn-Tucker (KKT) conditions, alternating optimization-based algorithm, and fractional programming based Dinkelbach Transform is proposed to jointly optimize the TS or PS ratio, and transmit power. Numerical simulations are conducted to evaluate the system performance highlighting the Rate and Energy trade-off across different scenarios, considering factors such as RIS surfaces count, element count, separation distance, EH, and data rate demands. Additionally, the proposed system has been analyzed while assuming an imperfect Channel State Information (CSI).

The chapter is organized as follows. Section 3.1 provides introduction, research gap, and

contributions, followed by discussion system setup in Section 3.2 encapsulating signal modeling, RIS selection, and SWIPT. Section 3.3, 3.4, 3.5 presents optimization problem and related solution of data rate, EH, and EE respectively. The results and related discussions are scripted in Section 3.6. The chapter finally rests with summary in Section 3.7.

3.1 Introduction to Multi-RIS assisted SWIPT-IoT Systems

RIS with SWIPT has emerged as a transformative technology for 6G networks, addressing the bottle-neck of the massive and seamless IoT connectivity while simultaneously supporting energy-efficient and battery-saving communication paradigms [42]. Time switching (TS) SWIPT offers relatively simpler receiver design while power splitting (PS) SWIPT achieves superior data rate and EH performance, particularly in highly resource-constrained environment [8].

The amalgamation of RIS-SWIPT has been explored in the literature with the adoption of EH modeling as linear or linear-type variants, i.e., constant-linear, piece-wise linear, and constant-linear-constant [36, 37, 43]. A limited number of studies have considered practical non-linear EH (NL-EH) by partitioning single RIS into separate groups (unit segments) dedicated either to perform EH or reflection operation [14], thereby enabling autonomous operation of RIS without requiring external power supply. Along the similar lines, authors in [44] divide RIS cells into two operational modes namely, 'S' mode, which performs simultaneous reflection and amplification and the 'H' mode, exclusive to EH process.[1] Advancing further, multiple RIS-assisted communication frameworks have been explored to enhance the coverage and resilient information signal delivery to the user node. Such distributed RIS

[1]The EH and signal relay mode are depicted as 'H' and 'S' mode, respectively.

Table 3.1: General survey based on recent RIS-SWIPT frameworks.

Ref.	**EH Model**	**SWIPT architecture**	**RIS**	**Objective Function**	**Imperfect CSI**
[36, 37]	CLC	Hybrid TS-PS	Single	Performance Analysis	X
[45]	NL-EH	Hybrid TS-PS	Multiple	Performance Analysis	X
[46, 47]	Linear	WPCN	Multiple	Performance Analysis	X
[34, 48]	X	X	Multiple	Performance Analysis	X
[16]	X	X	Multiple	Number of elements in each RIS	X
[49]	X	X	Multiple	Energy Efficiency	X
[50]	X	X	Multiple	SNR Maximization	X
[43]	Linear	PS	Single	Weighted sum of rate and EH	X
[14]	NL-EH	WPCN	Single	SNR Maximization	X
[51]	Linear	PS	Single	Weighted utility function of rate, EH, and total power consumption	X
[52]	NL-EH	TS	Multiple	Rate and EH maximization	X
[53]	NL-EH	PS	Single	Rate, EH maximization, and Power minimization	X
[54]	NL-EH	TS	Single	Weighted function of rate, EH, and transmit power	X
[55]	NL-EH	PS	Multiple	Weighted function of rate, EH, and transmit power	X
[44]	NL-EH	Separated IR and ER	Single	Sum rate maximization	X
[56]	Linear	Separated IR and ER	Single	Power Minimization	✓
This work	NL-EH	TS and PS	Multiple	Rate, EH, and Energy Efficiency maximization	✓

deployments naturally introduce the requirement of efficient RIS selection strategies.

Authors in [45] use all the RIS surfaces and related elements for communication purposes, with limited-to-no mention of SWIPT operation. To further reduce the resource consumption in multiple-RIS scenarios, selection planning of the RIS is given by authors in [52] for Vehicular Communication based on the highest end-to-end instantaneous SNR between road-side source to vehicle destination. Similarly, the authors in [50] developed location based selection approach considering product-scaling and sum-scaling path loss models, to provide maximized end-to-end SNR. The elevated EE performance through dynamic ON-OFF controlling of multiple RISs, jointly optimizing RIS phase shifts and beamforming

design has been investigated in [49]. Furthermore, a Wireless Powered Communication Network (WPCN) framework for distributed RIS systems is studied in [47], where the device first harvests energy from the access point (AP) through one RIS, and later utilizes the harvested energy to transmit information back to the AP via another RIS. However, the EH is modeled as a linear function and the study primarily focuses on performance analysis. In addition, a weighted objective function involving the data rate, EH, and transmit power is optimized with respect to the TS ratio for a single RIS case in [54], and with respect to PS factor in distributed RIS systems under NL-EH in [55]. A comparable objective is used in [51] with linear EH model. Moreover, the authors in [56] assessed a SWIPT architecture with separate information resource (IR) and energy resource (ER) users under the assumption of imperfect Channel State Information (CSI) analysis, while adopting a linearly modeled EH at the ER.

The existing literature suggests a scarcity of works exploring practically accurate NL-EH models in the RIS-assisted SWIPT-IoT systems. Limited works addresses the SWIPT protocol (TS and PS inclusive) for the multi-RIS configured system, under accurate EH model for optimization of EH, achievable data rate, and EE in the presence of imperfect CSI, as highlighted in Table. 3.1. Motivated by these research shortcomings, this chapter focuses on addressing these challenges, with the main contributions listed below.

- *Practical EH modeling:* The considered IoT device operates using either the TS or PS based SWIPT architecture while adopting a logistic non-linear EH model. Unlike conventional linear, piece-wise linear, or constant-linear-constant (CLC) models that assume simplified harvesting behavior, the adopted model more accurately reflects the practical non-linear characteristics of RF-to-DC energy conversion circuits.

- *Distributed multi-RIS framework:* To capture the realistic deployment scenarios, the study considers non-identically and independently distributed (ni.i.d.) channels

among multiple RISs. Within this framework, two RIS utilization strategies, namely, the ERA and ORA, are investigated and compared. In the ERA scheme, the signals from all RISs and their reflecting elements are received at user, whereas ORA selects the most suitable RIS for communication out of all.

- *Optimization framework and solution:* Three separate optimization problems corresponding to achievable rate, EH, and EE maximization are formulated respectively for both TS and PS protocols. The optimization jointly considers transmit power allocation and TS or PS ratio design under the associated system constraints. To solve maximization of rate and EH, the Karush-Kuhn-Tucker (KKT) conditions gives closed-form expressions for the optimal variables, and an alternating optimization-based framework is developed. The proposed method leverages a divide-and-conquer strategy to simplify the originally challenging optimization problem into tractable sub-problems. For the fractional EE maximization problem, the Dinkelbach transformation is utilized to obtain an efficient solution.

- *Performance evaluation and insights:* A comparative analysis between the TS or PS SWIPT architectures and RIS selection strategies is presented in terms of achievable rate, EH, and EE repectively. Detailed insights are obtained by varying the number of RISs, number of reflecting elements per RIS, separation distance, maximum transmit power, target EH and rate. In addition, the impact of imperfect CSI is thoroughly examined through CSI error analysis, highlighting its influence on the system performance for both the TS and PS schemes.

3.2 System Model

We consider a half-duplex (HD) communication network consisting of a single antenna base station (BS), a single antenna IoT user equipment (UE) node, and a set of N RISs deployed at random locations from each other. The BS and UE exists in the far field region from all the RISs [34]. Each RIS is denoted by $\{R_n\}_{n=1}^{N}$ having a total of $\{M_n\}_{n=1}^{N}$ reflecting elements. It is noteworthy that the direct communication between the BS and UE is obstructed. Fig. 3.1 depicts the communicating signal path from the BS, directed to i^{th} element of the n^{th} RIS (R_n) $\{i \in [1, M_n]\}$, and received at the UE. A low-mobility deployment scenario is considered in this work, where the RISs are well distant strategically mounted on structures such as building walls and billboards to provide a reliable connectivity in the coverage-deficient regions. The SWIPT-IoT UE node concurrently harvest energy and decodes data in accordance with either the TS or PS-SWIPT receiver architecture. However, for the considered scenario[2] the inter-RIS interference is significantly weak as compared to the intended RIS-assisted signal, such that it does not much contribute to either EH or data rate at UE.[3]

We consider α and β as TS and PS ratios, respectively. In the TS receiver, EH is performed for a time period (α) followed by ID for the remaining period $(1 - \alpha)$. Whereas in the case of PS protocol, the received power is divided for EH and ID, such that the former receives $\sqrt{\beta}$ times the power while rest is dedicated for the latter. It is important to note that for both the architectures sigmoid/logistic function based NL-EH model is utilized for its practical relevance in the context of RF-to-direct current energy conversion. The literature has proved its closeness to the practical model on several instances, while maintaining sev-

[2]Example of such scenarios is when one RIS can be installed on a building facade and another on a high-altitude roadside structure (billboard), which leads to large spatial separation.

[3]The same assumption holds good in the rest of the chapter for analytical and simulation part as well [34, 47, 49].

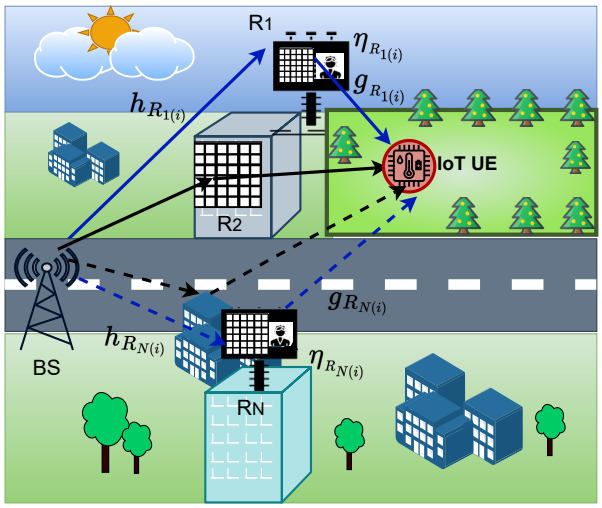


Figure 3.1: System model of IoT UE employing SWIPT in multi-RIS scenario.

eral reasons for other linear-like models to fail. Subsequently, we present the mathematical signal model in the next section.

3.2.1 Signal Modeling

We define the signal received from BS $\rightarrow i^{th}$ element of R_n RIS as $\tilde{h}_{R_{n(i)}}$ and i^{th} element of R_n RIS $\rightarrow$ UE as $\tilde{g}_{R_{n(i)}}$, where $i = 1, 2, \ldots M_n$. The channel coefficients are assumed to be the identical and independently distributed (i. i. d.) complex values, having magnitude of $h_{R_{n(i)}}$ and $g_{R_{n(i)}}$, with $e^{j\phi_{R_{n(i)}}}$ and $e^{j\psi_{R_{n(i)}}}$ as the phase angles respectively. The RIS surfaces are assumed to be sufficiently separated, resulting in the channels associated with them to be ni. i. d [34]. For instance, $\tilde{h}_{R_{1(i)}}$ and $\tilde{h}_{R_{n(i)}}\, \forall\, n{=}\{2, \cdots, N\}$ are ni. i. d. The received signal at the UE via integrated reflected signals from all M_n elements of n^{th} RIS (R_n) is given by

$$y_n = \sqrt{P_b}\left(\sum_{i=1}^{M_n} \tilde{g}_{R_{n(i)}}\, \eta_{R_{n(i)}}\, e^{j\theta_{R_{n(i)}}}\, \tilde{h}_{R_{n(i)}}\right) s + w_n, \tag{3.1}$$

where $\eta_{R_{n(i)}}$ denotes the amplitude of the reflection coefficient, whose value lies between 0 to 1, and $\theta_{R_{n(i)}} \in [-\pi, \pi]$ represents adjustable phase shift by the i^{th} element of R_n RIS. The phase tuning plays essential role in focusing reflected signal to the intended user, making it

a key distinguishing characteristic of RIS. The transmitting signal is s with unit power and P_b is the power available at the BS for transmission. The associated i. i. d. additive white Gaussian noise (AWGN) at UE is $w_n \sim \mathcal{CN}(0, W_0^2)$ with zero mean and W_0^2 variance. The related Signal-to-Noise ratio (SNR) at the UE is mathematically represented as

$$\Gamma_n = \frac{P_b}{W_0^2} \left| \sum_{i=1}^{M_n} g_{R_{n(i)}} \eta_{R_{n(i)}} h_{R_{n(i)}} e^{j(\theta_{R_{n(i)}} + \phi_{R_{n(i)}} + \psi_{R_{n(i)}})} \right|^2 . \tag{3.2}$$

The perfect CSI is assumed to be present globally, which will be ruled out in section 3.6 as an extensive ICSI analysis. In order to enhance the signal reception at the UE by maximizing the end-to-end SNR is by tuning the RIS phase adjustment reconfigurable controller in such a way that the total phase is nullified, i.e., $\theta_{R_{n(i)}} + \phi_{R_{n(i)}} + \psi_{R_{n(i)}} = 0$ [22, 36, 57]. The maximized SNR is

$$\Gamma_n = \frac{P_b}{W_0^2} \left| \sum_{i=1}^{M_n} g_{R_{n(i)}} \eta_{R_{n(i)}} h_{R_{n(i)}} \right|^2 = \frac{P_b Z_n}{W_0^2}. \tag{3.3}$$

Rewriting (3.3), the summation part consists of channel coefficients of all M_n RIS elements termed as the 'channel term' is written as $Z_n = \left| \sum_{i=1}^{M_n} g_{R_{n(i)}} \eta_{R_{n(i)}} h_{R_{n(i)}} \right|^2$. If a negligible direct BS-UE link exists, the received signal is the superposition of the direct and RIS-reflected components [4]. However, the direct link is assumed to be severely attenuated and its contribution to the received signal is negligible compared with the RIS-assisted link and

[4]The received signal at the UE consists of the superposition of the direct BS-UE signal ($h_{BU} e^{j\phi_{BU}}$) and the RIS-reflected signals, is given as [58][47]

$$y_n = \sqrt{P_b} \left(h_{BU} e^{j\phi_{BU}} + \sum_{i=1}^{M_n} g_{R_{n(i)}} \eta_{R_{n(i)}} h_{R_{n(i)}} e^{j(\theta_{R_{n(i)}} + \phi_{R_{n(i)}} + \psi_{R_{n(i)}})} \right) s + w_n, \tag{3.4}$$

The corresponding maximized SNR with perfectly matched phase i.e., ($\theta_{R_{n(i)}} = \phi_{BU} - \phi_{R_{n(i)}} - \psi_{R_{n(i)}}$), is expressed as

$$\Gamma_n = \frac{P_b}{W_0^2} \left| h_{BU} + \sum_{i=1}^{M_n} g_{R_{n(i)}} \eta_{R_{n(i)}} h_{R_{n(i)}} \right|^2 . \tag{3.5}$$

is therefore ignored for analytical tractability [16, 34].[5]

The main system concerns are threefold as follows: *(i) How these RIS surfaces are to be selected ? (ii) How it is being processed ? (iii) What will be the precursors on the system performance ?* We will address these issues in the subsequent section.

3.2.2 Multi-RIS Selection Strategies

When multiple RISs are nearby, selecting the best among them becomes crucial for an optimal performance. In this context, two potential methods for RIS selection are ERA and ORA [34], which are discussed below.

3.2.2.1 Optimal RIS Approach (ORA)

The ORA approach utilizes only the most appropriate RIS for transmitting the signal s, rather than employing all RISs $\left\{\left\{R_{n(i)}\right\}_{i=1}^{M_n}\right\}_{n=1}^{N}$. In order to achieve an optimum performance, the selection of the RIS surface yielding the highest SNR at the UE will be the wise decision to go with. Considering (3.3), the SNR depends majorly on the channel term (Z_n) involving n^{th} RIS surface for a fixed transmit power. Hence, the selection criteria being highest SNR, in fact implies stronger channel condition for the suitable RIS with maximum channel term. To achieve the said criteria, initially 'channel term' for all RIS surfaces are assumed to be known at the UE by the channel estimation techniques (ie., perfect CSI assumption). The selection process undertaken by the UE is mathematically given by

$$\widehat{Z}_{n^*} = \max_{n=1,\ldots,N} \left\{ \left| \sum_{i=1}^{M_n} g_{R_{n(i)}} \eta_{R_{n(i)}} h_{R_{n(i)}} \right|^2 \right\}. \tag{3.6}$$

[5]This interesting problem of direct link is left for future work, where the proposed method can be extended to more complex physical models.

The received signal and SNR with the selected RIS ($n^* = arg(\widehat{Z}_{n^*})$), is modified to

$$y_{n^*}=\sqrt{P_b}\left(\sum_{i=1}^{M_{n^*}} \tilde{g}_{R_{n^*(i)}}\eta_{R_{n^*(i)}}e^{j\theta_{R_{n^*(i)}}}\tilde{h}_{R_{n^*(i)}}\right)s+w, \quad \widehat{\Gamma}_{n^*}=\frac{P_b\widehat{Z}_{n^*}}{W_0^2}. \tag{3.7}$$

Herein, the transmit power at BS is assumed to be P_b, circuit power of BS is $\check{P}_{BS}$ and at the UE, it is $\check{P}_{UE}$, along with dynamic $\bar{P}_{RIS}$ and static power $\bar{\bar{P}}_{RIS}$ consumption at selected RIS R_{n^*} constitutes total power consumption given by

$$\widehat{P}_T = P_b + \check{P}_{BS} + \check{P}_{UE} + \bar{\bar{P}}_{RIS} + \bar{P}_{RIS}M_{n^*} \tag{3.8}$$

3.2.2.2 Exhaustive RIS Approach (ERA)

In this method, all RISs and their respective elements, $\left\{\{R_{n(i)}\}_{i=1}^{M_n}\right\}_{n=1}^{N}$, aid in transmitting the signal from the BS to the UE on the same time-frequency resource. Each RIS is designed to enhance the SNR at UE by skillfully directing the incoming signals (multiple copies from the BS) towards UE. This approach assumes there is no interference between the RISs, as noted in [34, 59]. The modified channel parameter and SNR for ERA case are mathematically represented as

$$\overline{\mathbb{Z}} = \left|\sum_{n=1}^{N}\sum_{i=1}^{M_n} g_{R_{n(i)}}\eta_{R_{n(i)}}h_{R_{n(i)}}\right|^2, \quad \overline{\Gamma}=\frac{P_b\overline{\mathbb{Z}}}{W_0^2}. \tag{3.9}$$

The total power in ERA case is

$$\overline{P_T} = P_b + \check{P}_{BS} + \check{P}_{UE} + \sum_{n=1}^{N}(\bar{\bar{P}}_{RIS} + \bar{P}_{RIS}M_n). \tag{3.10}$$

Remark: In the subsequent discussion, the channel parameter is denoted by $Z_n \in [\widehat{Z}_{n^*}, \overline{\mathbb{Z}}]$, the SNR as $\Gamma_n \in [\widehat{\Gamma}_{n^*}, \overline{\Gamma}]$ and total power consumption as $P_T \in [\widehat{P}_T, \overline{P_T}]$ depending on the ORA (3.7), (3.8) or ERA (3.9), (3.10) approach.

3.2.3 Simultaneous Wireless Information and Power Transmission (SWIPT)

The UE is capable of SWIPT operation being equipped with either the TS or PS based receiver. We shall compare and analyze both the architectures and later concludes the best among them for the considered multi-RIS scenario. The respective information rate for $(1-\alpha)$ time duration in the TS scenario, and for PS it is $\sqrt{\beta}$ times of received power, mathematically given as [31, 60].

$$R_u^T = (1-\alpha)\log_2(1+\Gamma_n), \quad R_u^P = \log_2(1+(1-\beta)\Gamma_n). \tag{3.11}$$

The sigmoid/logistic function based practical EH model capturing the non-linear energy conversion efficiency (RF to battery current) represents the TS or PS-based EH part [32, 60], represented as follows

$$E_h^T = \frac{\alpha E'}{1-\chi}\left(\frac{1}{1+\exp(-aP_bZ_n+ab)}-\chi\right), E_h^P = \frac{E'}{1-\chi}\left(\frac{1}{1+\exp(-\beta aP_bZ_n+ab)}-\chi\right), \tag{3.12}$$

where χ depends on electronic circuit elements a and b, associated with the capacitor and diode turn-ON voltage respectively. Specifically, it is defined as $\chi = (1+\exp(ab))^{-1}$. The constant E' represents the maximum harvested energy when the EH circuit is operating in saturation. The values of the constant parameters (E', a, b) are typically determined through the utilization of a curve-fitting tool applied to the analytical data, as discussed in [31]. It is worth noting that the given sigmoid NL-EH model is for far-field propagation [32].

The EE is the ratio of data rate to the total combined power consumption by BS, RIS and UE. It is respectively defined for the TS and PS protocols as

$$\Xi^T = \frac{R_u^T(\alpha, P_b)}{P_T}, \quad \Xi^P = \frac{R_u^P(\beta, P_b)}{P_T}. \tag{3.13}$$

To improve the clarity of notation, we present the following quad (rate, EH, EE, and TS or PS ratio) (3.14) in the rest of the discussions, i.e., for TS ($\Phi = \alpha$) and for PS ($\Phi = \beta$), as follows.

$$(R_u, E_h, \Xi, \Phi) := \begin{cases} (R_u^T, E_h^T, \Xi^T, \alpha) : \text{ For TS} \\ (R_u^P, E_h^P, \Xi^P, \beta) : \text{ For PS.} \end{cases} \tag{3.14}$$

In the subsequent section, we articulate the primary problem concerning the maximization of rate, EH, and EE distinctly.

3.3 Data Rate Maximization

We formulate the rate maximization problem while optimizing the transmit power and TS or PS factor along with the constraints on rate, EH, maximum transmit power ($\mathcal{P}_{max}$), and available range of TS or PS ratio. The overall optimization problem is mathematically expressed as

$$\text{(P1): } \underset{\Phi, P_b}{\text{maximize}} \quad R_u(\Phi, P_b) \tag{3.15}$$

$$\text{subject to :} \quad R_u \geq \mathcal{R}_{th}, \tag{3.16}$$

$$E_h \geq \xi_{th}, \tag{3.17}$$

$$0 < P_b \leq \mathcal{P}_{max},\ 0 \leq \Phi \leq 1, \tag{3.18}$$

where the demanded rate and EH are $\mathcal{R}_{th}$ and ξ_{th}, respectively, which confirms the satisfactory data rate and varying energy demands in context to environmental changes. The choice of TS or PS is taken care of by the notations and the expressions related to (3.14).

3.3.1 Optimized solution for TS

Herein, we address the problem (P1) for the TS receiver by invoking (3.14)-(3.18). This problem is a non-linear programming challenge that entails simultaneous computation of α and P_b, making it difficult to obtain an exact solution. Given that the constraints exhibit partial convexity when the other variables are held constant, we consider employing the KKT conditions to address this issue [20]. For KKT, the initial step is to find the Lagrangian dual of (P1) for the TS case, given by

$$L(\alpha, P_b; \mathbf{\Lambda}) = R_u^T + \lambda_1(R_u^T - \mathcal{R}_{th}) + \lambda_2(E_h^T - \xi_{th}) + \lambda_3(\mathcal{P}_{\max} - P_b) + \lambda_4(1-\alpha). \quad (3.19)$$

To achieve (local or global) optimality, it is necessary for $\Delta L(\alpha, P_b; \mathbf{\Lambda}) = 0$ to be satisfied. Consequently, we express the equations that ensures the fulfillment of the optimal conditions as follows

$$\frac{\partial L(\alpha, P_b; \mathbf{\Lambda})}{\partial P_b} = \frac{\partial L(\alpha, P_b; \mathbf{\Lambda})}{\partial \alpha} = 0, \quad (3.20)$$

$$\frac{(1-\alpha) Z_n (1+\lambda_1)}{(W_0^2 + P_b Z_n)\ln(2)} + \left(\frac{\lambda_2 \alpha E'(a Z_n \exp(\Sigma))}{(1-\chi)(1+\exp(\Sigma))^2}\right) - \lambda_3 = 0, \quad (3.21)$$

$$-\log_2\left(1 + \frac{P_b Z_n}{W_0^2}\right)(1+\lambda_1) + \left(\frac{\lambda_2 E'}{(1-\chi)}\left(\frac{1}{1+\exp(\Sigma)} - \chi\right)\right) - \lambda_4 = 0. \quad (3.22)$$

Here $\Sigma = -aP_bZ_n + ab$. The feasible conditions include: $R_u^T - \mathcal{R}_{th} \geq 0$, $E_h^T - \xi_{th} \geq 0$, $\mathcal{P}_{\max} - P_b \geq 0$, and $1 - \alpha \geq 0$. The complimentary slackness conditions are stated as $\lambda_1(R_u^T - \mathcal{R}_{th}) = 0$, $\lambda_2(E_h^T - \xi_{th}) = 0$, $\lambda_3(\mathcal{P}_{\max} - P_b) = 0$, and $\lambda_4(1-\alpha) = 0$. The Lagrangian variables along with optimizing variables must be a positive quantity, i.e., $\mathbf{\Lambda}, \alpha,$ and $P_b > 0$. From all the KKT complementary slackness conditions, it is obvious that λ_4 must be zero, implying $\alpha \neq 1$. This leaves us with eight different possibilities (see Appendix B.1) for seeking an optimal solution, out of which the final (potential) solutions are provided in

Theorem 1 and Theorem 2, discussed below.

Theorem 1: If $\lambda_1 = 0 \Rightarrow (R_u^T - \mathcal{R}_{th}) \neq 0$; $\lambda_2 \neq 0 \Rightarrow (E_h^T - \xi_{th})=0$; $\lambda_3 \neq 0 \Rightarrow (\mathcal{P}_{\max} - P_b)=0$, and the optimal values are

$$P_b^* = \mathcal{P}_{\max}, \quad \alpha^* = \frac{\xi_{th}(1-\chi)}{E'\left(\frac{1}{1+exp(-aP_bZ_n+ab)} - \chi\right)}. \tag{3.23}$$

Proof: See Appendix B.1

Theorem 2: If $\lambda_1 \neq 0 \Rightarrow (R_u^T - \mathcal{R}_{th})=0$; $\lambda_2 \neq 0 \Rightarrow (E_h^T - \xi_{th})=0$; $\lambda_3 \neq 0 \Rightarrow (\mathcal{P}_{\max} - P_b)=0$, and the optimal values are

$$P_b^\dagger = \mathcal{P}_{\max}, \quad \alpha^\dagger = \min(\alpha_1, \alpha_2), \tag{3.24}$$

where

$$\alpha_1 = 1 - \frac{\mathcal{R}_{th}}{\log_2\left(1 + \frac{P_bZ_n}{W_0^2}\right)}, \quad \alpha_2 = \frac{\xi_{th}(1-\chi)}{E'\left(\frac{1}{1+exp(-aP_bZ_n+ab)} - \chi\right)}. \tag{3.25}$$

Proof: See Appendix B.1.

It is worth noting that a KKT point may not only represent a local optimum but could also denote a saddle point or even a point of maximum value.

The following section provides an optimized solution for the considered PS case to maximize the rate.

3.3.2 Optimized solution for PS

We tackle the problem (P1) for the PS mechanism, referring to equations (3.14) through (3.18). To address the complex non-convex problem, we propose employing the KKT-based solutions for determination of optimized β and P_b. The Lagrangian dual for problem (P1)

in the PS case is

$$L(\beta, P_b; \boldsymbol{\nu})=R_u^P+\mu_1(R_u^P-\mathcal{R}_{th})+\mu_2(E_h^P-\xi_{th})+\mu_3(\mathcal{P}_{\max}-P_b)+\mu_4(1-\beta). \quad (3.26)$$

The local optimality is satisfied by $\Delta L(\beta, P_b; \boldsymbol{\nu})=0$ given by

$$\frac{\partial L(\beta, P_b; \boldsymbol{\nu})}{\partial P_b} = \frac{\partial L(\beta, P_b; \boldsymbol{\nu})}{\partial \beta} = 0, \quad (3.27)$$

$$\frac{(1-\beta)\Sigma'(1+\mu_1)}{\ln(2)}+\left(\frac{\mu_2\beta E'\Sigma''}{(1-\chi)}\right)-\mu_3=0, \quad (3.28)$$

$$-\frac{W_0^2 P_b\Sigma'}{\ln(2)}(1+\mu_1)+\left(\frac{\mu_2 E' P_b\Sigma''}{(1-\chi)}\right)-\mu_4=0. \quad (3.29)$$

Here $\Sigma' = \frac{Z_n}{W_0^2+(1-\beta)P_b Z_n}$ and $\Sigma'' = \frac{aZ_n \exp(-a\beta P_b Z_n+ab)}{(1+\exp(-a\beta P_b Z_n+ab))^2}$. The feasibility conditions include: $R_u^P-\mathcal{R}_{th} \geq 0$, $E_h^P-\xi_{th} \geq 0$, $\mathcal{P}_{\max}-P_b \geq 0$, and $1-\beta \geq 0$. The complimentary slackness conditions are: $\mu_1(R_u^P-\mathcal{R}_{th})=0$, $\mu_2(E_h^P-\xi_{th})=0$, $\mu_3(\mathcal{P}_{\max}-P_b)=0$, and $\mu_4(1-\beta)=0$. The variables $\boldsymbol{\nu}, \beta, P_b$ must be positive, considering all the KKT conditions gives $\mu_4 = 0$ and $\beta \neq 1$. All the possibilities are given in Appendix B.1 with concise solution provided herein in the form of Theorem 3 and Theorem 4, respectively discussed as follows.

Theorem 3: If $\mu_1 = 0 \Rightarrow (R_u^P-\mathcal{R}_{th}) \neq 0$; $\mu_2 \neq 0 \Rightarrow (E_h^P-\xi_{th})=0$; $\mu_3 \neq 0 \Rightarrow (\mathcal{P}_{\max}-P_b)=0$, and the optimal values are

$$P_b^* = \mathcal{P}_{\max}, \quad \beta^* = \frac{1}{\mathcal{P}_{\max} Z_n}\left(b-\frac{1}{a}\ln\left(\frac{(1-\chi)(E'-\xi_{th})}{\xi_{th}(1-\chi)+\chi E'}\right)\right). \quad (3.30)$$

Proof: See Appendix B.1.

Theorem 4: If $\mu_1 \neq 0 \Rightarrow (R_u^P-\mathcal{R}_{th})=0$; $\mu_2 \neq 0 \Rightarrow (E_h^P-\xi_{th})=0$; $\mu_3 \neq 0 \Rightarrow (\mathcal{P}_{\max}-P_b)=0$, and the optimal values are

$$P_b^\dagger = \mathcal{P}_{\max}, \quad \beta^\dagger = \min(\beta_1, \beta_2). \quad (3.31)$$

where

$$\beta_1 = 1 - \frac{W_0^2(2^{\mathcal{R}_{th}} - 1)}{\mathcal{P}_{\max} Z_n}, \quad \beta_2 = \frac{1}{\mathcal{P}_{\max} Z_n} \left(b - \frac{1}{a} \ln \left(\frac{(1-\chi)(E' - \xi_{th})}{\xi_{th}(1-\chi) + \chi E'} \right) \right). \tag{3.32}$$

Proof: See Appendix B.1.

Considering the solutions for Problem (P1) provided in Theorems 1 and 2 for TS, and Theorems 3 and 4 for PS, the maximized information rate is given by optimized variables $P_b^\dagger$ and $\Phi^\dagger \in [\alpha^\dagger, \beta^\dagger]$ as $R_u(\Phi^\dagger, P_b^\dagger) \in [R_u^T(\alpha^\dagger, P_b^\dagger), R_u^P(\beta^\dagger, P_b^\dagger)]$. The classical trade-off between rate and EH for SWIPT will be explained in next section, where we maximize the EH for both TS and PS protocols.

3.4 Harvested Energy Maximization

We define the problem of maximizing EH while optimizing the transmit power and the TS or PS ratio. This is performed under various constraints, including those related to rate, EH, $\mathcal{P}_{max}$, and the permissible range of TS or PS ratio. This formulation is expressed as

$$\text{(P2): } \underset{\Phi, P_b}{\text{maximize}} \quad E_h(\Phi, P_b) \tag{3.33}$$

$$\text{subject to :} \quad (3.16) - (3.18) \tag{3.34}$$

The constraints for (P2) remain the same as for Problem (P1). The determination of the TS or PS is managed through the notations and expressions associated with (3.14).

3.4.1 Optimized solution for TS

This section addresses (P2) for the TS receiver considering (3.14), (3.33)-(3.34). The problem is non-convex in nature due to the non-linear sigmoid objective function and finding an exact solution for it, is quite cumbersome. The KKT conditions have proven to provide

near-optimal solutions for such non-convex problems, hence we utilize it for solving (P2). As an initial step, we need to find the Lagrangian dual for the TS case in (P2), given by

$$\mathcal{L}(\alpha, P_b; \mathbf{\Lambda}) = E_h^T + \lambda_1(R_u^T - \mathcal{R}_{th}) + \lambda_2(E_h^T - \xi_{th}) + \lambda_3(\mathcal{P}_{\max} - P_b) + \lambda_4(1-\alpha). \quad (3.35)$$

The optimality condition, whether local or global, is fulfilled by $\Delta\mathcal{L}(\alpha, P_b; \mathbf{\Lambda}) = 0 \Rightarrow \frac{\partial\mathcal{L}(\alpha,P_b;\mathbf{\Lambda})}{\partial P_b} = \frac{\partial\mathcal{L}(\alpha,P_b;\mathbf{\Lambda})}{\partial\alpha} = 0$. Solving further

$$\left(\frac{e^{\Sigma}(1+\lambda_1)\alpha E' a Z_n}{(1-\chi)(1+e^{\Sigma})^2}\right) + \frac{\lambda_2(1-\alpha)Z_n}{(W_0^2 + P_b Z_n)\ln(2)} - \lambda_3 = 0, \quad (3.36)$$

$$\frac{(1+\lambda_1)E'}{(1-\chi)}\left(\frac{1}{1+\exp(\Sigma)} - \chi\right) - \lambda_2 \log_2\left(1 + \frac{P_b Z_n}{W_0^2}\right) - \lambda_4 = 0. \quad (3.37)$$

The feasibility and complementary conditions are : $R_u^T - \mathcal{R}_{th} \geq 0$, $E_h^T - \xi_{th} \geq 0$, $\mathcal{P}_{\max} - P_b \geq 0$, and $1-\alpha \geq 0$; $\lambda_1(R_u^T - \mathcal{R}_{th})=0$, $\lambda_2(E_h^T - \xi_{th})=0$, $\lambda_3(\mathcal{P}_{\max} - P_b)=0$, and $\lambda_4(1-\alpha)=0$; respectively. The variables $\mathbf{\Lambda}, \alpha, P_b$ should be positive in nature. For all the above stated conditions to be satisfied, λ_4 must be zero, thereby resulting in $\alpha \neq 1$. The Theorems 5 and 6 represents the cases which satisfies the above conditions and provide a sub-optimal (or optimal) solution.

Theorem 5: If $\lambda_1 \neq 0 \Rightarrow (R_u^T - \mathcal{R}_{th})=0$; $\lambda_2=0 \Rightarrow (E_h^T - \xi_{th}) \neq 0$; $\lambda_3 \neq 0 \Rightarrow (\mathcal{P}_{\max} - P_b)=0$, the the optimal values are

$$P_b^* = \mathcal{P}_{\max}, \quad \alpha^* = 1 - \frac{\mathcal{R}_{th}}{\log_2\left(1 + \frac{P_b Z_n}{W_0^2}\right)}, \quad (3.38)$$

Proof: See Appendix B.2.

Theorem 6: If $\lambda_1 \neq 0 \Rightarrow (R_u^T - \mathcal{R}_{th})=0$; $\lambda_2 \neq 0 \Rightarrow (E_h^T - \xi_{th})=0$; $\lambda_3 \neq 0 \Rightarrow$

$(\mathcal{P}_{\max} - P_b)=0$. Optimal values are

$$P_b^{\dagger} = \mathcal{P}_{\max}, \quad \alpha^{\dagger} = \max(\alpha_1, \alpha_2) \tag{3.39}$$

where α_1 and α_2 have values from (3.25).

Proof: See Appendix B.2.

In the upcoming section, we provide optimized solution for considered PS case for EH maximization.

3.4.2 Optimized solution for PS

Herein, we handle (P2) for the PS receiver by solving it using KKT, as (P2) is inherently non-convex in nature. As a preliminary step, we derive the Lagrangian dual for the PS case of (P2) as follows.

$$\mathcal{L}(\beta, P_b; \boldsymbol{\nu})=E_h^P+\mu_1(R_u^P - \mathcal{R}_{th})+\mu_2(E_h^P - \xi_{th})+\mu_3(\mathcal{P}_{\max} - P_b)+\mu_4(1 - \beta). \tag{3.40}$$

For Step 2, following condition should be meet.

$$\Delta\mathcal{L}(\beta, P_b; \boldsymbol{\nu})=0 \Rightarrow \frac{\partial\mathcal{L}(\beta, P_b; \boldsymbol{\nu})}{\partial P_b}=\frac{\partial\mathcal{L}(\beta, P_b; \boldsymbol{\nu})}{\partial \beta}=0, \tag{3.41}$$

which further solves to

$$\frac{(1 - \beta)\Sigma'(1 + \mu_1)}{\ln(2)}+\left(\frac{\mu_2\beta E'\Sigma''}{(1 - \chi)}\right) -\mu_3=0, \tag{3.42}$$

$$-\frac{W_0^2 P_b\Sigma'}{\ln(2)}(1 + \mu_1)+\left(\frac{\mu_2 E' P_b\Sigma''}{(1 - \chi)}\right) -\mu_4=0. \tag{3.43}$$

Expressions for Σ' and Σ'' are the same as given in Section 3.3.2. As a part of the KKT, the feasible conditions and complimentary slackness conditions include, $R_u^P - \mathcal{R}_{th} \geq 0$, $E_h^P - \xi_{th} \geq 0$, $\mathcal{P}_{\max} - P_b \geq 0$, and $1 - \beta \geq 0$; $\mu_1(R_u^P - \mathcal{R}_{th})=0$, $\mu_2(E_h^P - \xi_{th})=0$,

$\mu_3(\mathcal{P}_{\max}-P_b)=0$, and $\mu_4(1-\beta)=0$, respectively. The always positive quantities are $\boldsymbol{\nu}, \beta, P_b$. The above conditions are satisfied only when $\mu_4 = 0$ and $\beta \neq 1$. The rest of the cases count to eight (Appendix B.2), out of which, Theorems 7 and 8 represent the satisfied cases leading to an optimal solution.

Theorem 7: If $\mu_1 \neq 0 \Rightarrow (R_u^P - \mathcal{R}_{th})=0$; $\mu_2=0 \Rightarrow (E_h^P - \xi_{th}) \neq 0$; $\mu_3 \neq 0 \Rightarrow (\mathcal{P}_{\max} - P_b)=0$. Following provides optimal values

$$P_b^* = \mathcal{P}_{\max}, \quad \beta^* = 1 - \frac{W_0^2(2^{\mathcal{R}_{th}} - 1)}{\mathcal{P}_{\max} Z_n}. \tag{3.44}$$

Proof: See Appendix B.2.

Theorem 8: If $\mu_1 \neq 0 \Rightarrow (R_u^P - \mathcal{R}_{th})=0$; $\mu_2 \neq 0 \Rightarrow (E_h^P - \xi_{th})=0$; $\mu_3 \neq 0 \Rightarrow (\mathcal{P}_{\max} - P_b)=0$. The optimal values are

$$P_b^\dagger = \mathcal{P}_{\max}, \quad \beta^\dagger = \max(\beta_1, \beta_2). \tag{3.45}$$

where β_1 and β_2 is similar to (3.32).

Proof: See Appendix B.2.

Taking into account the solutions for combined Problem (P2) furnished by Theorems 5 and 6 for TS; and Theorems 7 and 8 for PS, the maximized EH is provided by optimized variables $P_b^\dagger$ and $\Phi^\dagger := \{\alpha^\dagger, \beta^\dagger\}$ as $E_h(\Phi^\dagger, P_b^\dagger) := \{E_h^T(\alpha^\dagger, P_b^\dagger), E_h^P(\beta^\dagger, P_b^\dagger)\}$ In the next section we pursue the algorithmic aspect for providing solution to Problems (P1) and (P2).

3.4.3 Algorithmic Solution for Rate and EH Maximization

Based on the aforementioned analysis, we were able to obtain reasonable solutions via KKT methodology. This section provides algorithmic solution to the inter-twinned optimizing variables Φ (i.e., α or β) and P_b of the primal problems (P1) for rate maximization and (P2) for EH maximization. Since both the problems have the same set of constraints, we will

define a new notation $\mathcal{Z}_x \forall x \in [t,p]$ that takes either TS $\big(\mathcal{Z}_t(\alpha, P_b)\big)$ or PS $\big(\mathcal{Z}_p(\beta, P_b)\big)$ case at a time. The case for TS or PS is further divided into two cases of rate or EH maximization objective function at a time. Thus, (3.46) facilitates four cases, i.e., EH maximization with TS or, TS for rate maximization or, PS for EH maximization, or rate maximization with PS, out of which only one will be considered at a time. The overall encapsulated form is defined as follows

$$\underset{\forall x\in[t,p],\Phi\in[\alpha,\beta]}{\mathcal{Z}_x(\Phi, P_b)}=\begin{cases}\mathcal{Z}_t(\alpha, P_b)=\begin{cases}R_u^T(\alpha, P_b) : \text{Rate for TS}\\ E_h^T(\alpha, P_b) : \text{EH for TS}\end{cases}\\ \mathcal{Z}_p(\beta, P_b)=\begin{cases}R_u^P(\beta, P_b) : \text{Rate for PS}\\ E_h^P(\beta, P_b) : \text{EH for PS}\end{cases}\end{cases} \tag{3.46}$$

A commonly developed primal problem that takes into account both (P1) and (P2) given by

$$\text{(P3): } \underset{\Phi, P_b}{\text{maximize}} \qquad \mathcal{Z}_x(\Phi, P_b) \ \ \forall x \in [t,p], \Phi \in [\alpha, \beta] \tag{3.47}$$

$$\text{subject to :} \qquad (3.16) - (3.18). \tag{3.48}$$

The problem (P3) encapsulates four distinct cases of rate maximization for TS or PS (i.e., $R_u^T(\alpha, P_b)$ or $R_u^P(\beta, P_b)$) resembling (P1) in (3.15), and EH maximization for TS or PS (i.e., $E_h^T(\alpha, P_b)$ or $E_h^P(\beta, P_b)$) akin to (P2) as in (3.33). Due to presence of Φ and P_b in both constraints and objective function(s), (P3) becomes non-convex problem. Here, we will adopt the divide-and-conquer (DAC) approach by breaking the primal problem (P3)

involving $\mathcal{Z}_t$ into sub-problems $(P3)_a$ and $(P3)_b$ for TS. It is mathematically given as follows

$$(P3)_a : \underset{\alpha}{\text{maximize}} \quad \mathcal{Z}_t(\alpha, P_b) \tag{3.49}$$

$$\text{subject to :} \quad \alpha \leq 1 - \frac{\mathcal{R}_{th}}{\log_2\left(1 + \frac{P_b Z_n}{W_0^2}\right)}, \tag{3.50}$$

$$\alpha \geq \frac{\xi_{th}(1-\chi)}{E'\left(\frac{1}{1+\exp(-aP_bZ_n+ab)} - \chi\right)}, \tag{3.51}$$

$$0 \leq \alpha \leq 1. \tag{3.52}$$

$$(P3)_b : \underset{P_b}{\text{maximize}} \quad \mathcal{Z}_t(\alpha, P_b) \tag{3.53}$$

$$\text{subject to :} \quad P_b \geq \frac{W_0^2}{Z_n}\left(2^{\frac{\mathcal{R}_{th}}{(1-\alpha)}} - 1\right), \tag{3.54}$$

$$P_b \geq \frac{b}{Z_{n^*}} - \frac{1}{aZ_{n^*}} \ln\left(\frac{(1-\chi)(\alpha E' - \xi_{th})}{\xi_{th}(1-\chi) + \chi\alpha E'}\right), \tag{3.55}$$

$$0 < P_b \leq \mathcal{P}_{\max}. \tag{3.56}$$

Similar DAC approach gives sub-problems concerning PS and $\mathcal{Z}_p$ as follows

$$(P3)_c : \underset{\beta}{\text{maximize}} \quad \mathcal{Z}_p(\beta, P_b) \tag{3.57}$$

$$\text{subject to :} \quad \beta \geq \frac{1}{P_b Z_n}\left(b - \frac{\ln \Sigma'''}{a}\right), \tag{3.58}$$

$$\beta \leq 1 - \frac{W_0^2}{P_b Z_n}(2^{\mathcal{R}_{th}} - 1), \tag{3.59}$$

$$0 \leq \beta \leq 1. \tag{3.60}$$

$$(P3)_d : \underset{P_b}{\text{maximize}} \quad \mathcal{Z}_p(\beta, P_b) \tag{3.61}$$

$$\text{subject to :} \quad P_b \geq \frac{1}{\beta Z_n}\left(b - \frac{\ln \Sigma'''}{a}\right), \tag{3.62}$$

$$P_b \geq \frac{W_0^2}{(1-\beta)Z_n}(2^{\mathcal{R}_{th}} - 1), \tag{3.63}$$

$$0 < P_b \leq \mathcal{P}_{\max}. \tag{3.64}$$

where $\Sigma''' = \frac{(1-\chi)(E'-\xi_{th})}{\xi_{th}(1-\chi)+\chi E'}$. Inspired by the AOA [61], Algorithm 3.1 regulates the above stated sub-problems $(P3)_a$ as in (3.49) and $(P3)_b$ as in (3.53) for TS, and $(P3)_c$ as in (3.57) and $(P3)_d$ as in (3.61) for PS, respectively. We shall be writing Algorithm 3.1 for equivalent primal problem (P3), which takes care of all the associated four subordinate cases (3.46). We commence by initializing an array $\mathcal{Z}_x(\Phi, P_b)\forall x \in [t, p], \Phi \in [\alpha, \beta]$, along with the variable P_b, which is assigned two similar feasible values. The procedure unfolds as follows: First, we set P_b at a constant value and calculate ($\Phi = \alpha$) as part of sub-problem $(P3)_a$ as in (3.49) for TS, on the other hand for PS evaluates ($\Phi = \beta$) using $(P3)_c$ as in (3.57). Subsequently, we determine the value of P_b in $(P3)_b$ as in (3.53) or $(P3)_d$ as in (3.61) using the $\Phi = \alpha$ or β obtained from solving the preceding sub-problem $(P3)_a$ or $(P3)_c$, respectively. We then utilize the found values of P_b and Φ to address $\mathcal{Z}_x(\Phi, P_b)$. If the current value of $\mathcal{Z}_x(\Phi, P_b)$ is lower than the previous value or the iteration reaches its upper limit k', we terminate the loop. Otherwise, we preserve the current value and continue the iteration until we reach a lower value. This iterative process ultimately yields the optimized value of P_b^* and Φ^* with maximized objective function. The proposed Algorithm 3.1 is presented as follows

Algorithm 3.1 Maximization Algorithm based on AOA

1: **Initialize variables:** $\mathcal{Z}_x^{(1)}=\mathcal{Z}_x^{(2)}\forall x \in [t, p], \Phi \in [\alpha, \beta]$, $P_b^{(1)}=P_b^{(2)}$, k', k=2.
2: *For TS:* Solve (3.49) with given $P_b^{(k)}$ and find $\alpha^{(k+1)}$.
3: *For PS:* Solve (3.57) with given $P_b^{(k)}$ and find $\beta^{(k+1)}$.
4: *For TS:* Solve (3.53) with obtained $\alpha^{(k+1)}$ from step 2 and find $P_b^{(k+1)}$.
5: *For PS:* Solve (3.61) with obtained $\beta^{(k+1)}$ from step 2 and find $P_b^{(k+1)}$.
6: Evaluate $\mathcal{Z}_x^{(k+1)}$ with $\Phi^{(k+1)}$ and $P_b^{(k+1)}$ obtained from step 2 and 3 respectively.
7: **If** $\mathcal{Z}_x^{(k+1)} \geq \mathcal{Z}_x^{(k)}$ **and** $k \leq k'$, **then** Go to step 2 with updated $P_b^{(k+1)}$ and $k = k + 1$.
8: **If** $\mathcal{Z}_x^{(k+1)} < \mathcal{Z}_x^{(k)}$ **or** $k > k'$, **then** loop stops. Go to step 7.
9: **Output:** $\mathcal{Z}_x^{(k-1)}$, $P_b^* \leftarrow P_b^{(k-1)}$, $\Phi^* \leftarrow \Phi^{(k-1)}$.

Initiating $\mathcal{Z}_x$ with an initial feasible value is essential to ensure that subsequent values are obtained while maintaining the condition $\mathcal{Z}_x^{(k+1)} \geq \mathcal{Z}_x^{(k)}$. The convergence plot is given in Fig. 3.2.

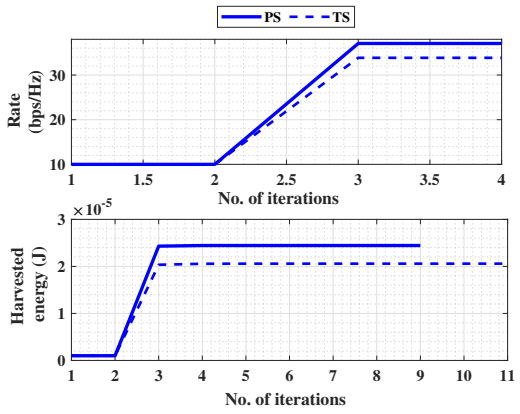


Figure 3.2: Convergence plot of Algorithm 3.1 for rate and EH maximization with TS or PS cases.

The computation complexity for solving step 2 of Algorithm 3.1 is $\kappa_1(NM^2)$ and step 3 is $\kappa_2(NM^2)$, also it takes A_I iterations for the maximization of $\mathcal{Z}_x$. The overall asymptotic complexity of Algorithm 3.1 is $\mathcal{O}\Big(A_I\big(\kappa_1(NM^2) + \kappa_2(NM^2)\big)\Big)$, which grows with the RIS elements and surfaces in the vicinity. Apart from the circuits of BS and UE, the nearly passive RIS surface too utilizes some power for its phase reconfiguration. In the next section, we demonstrate how this power consumption impacts the data rate and how the system parameters are optimized to make the system robust.

3.5 Maximization of Energy Efficiency (EE)

Another performance metric to evaluate the practical implementation and robustness of the multi-RIS SWIPT system is the EE. In this section, we will define the EE maximization problem (P4) for optimized TS or PS ratio and transmit power with the set of constraints on data rate, EH, transmit power and TS or PS ratio $\Phi := \{\alpha, \beta\}$. The overall optimization

problem is mathematically expressed as

$$\text{(P4): } \underset{\Phi, P_b}{\text{maximize}} \quad \Xi(\Phi, P_b) = \frac{R_u(\Phi, P_b)}{P_T} \tag{3.65}$$

$$\text{subject to :} \quad (3.16) - (3.18). \tag{3.66}$$

The Problem (P4) takes both the TS and PS scenarios into consideration and the related rate and EH. The non-convex fractional nature of (P4) requires to find solution using fractional programming techniques.

3.5.1 Dinkelbach based Solution

The Problem (P4) is fraction of concave-convex type problem which can be solved by the Dinkelbach based transform from the concepts of fractional programming. In this we convert the fraction into a substractive parametric form with q as an auxiliary variable, the transformed problem is given as [55]

$$\Xi_d(q) = \underset{\{\Phi, P_b\} \in \mathcal{D}}{\text{maximize}} \quad R_u(\Phi, P_b) - qP_T(P_b). \tag{3.67}$$

The domain $\mathcal{D}$ comprises the values of $\{\Phi, P_b\}$ which satisfies the constraints (3.16)-(3.18). The optimized values of original problem (P4) are $\{\Phi^*, P_b^*\}$ can be obtained if and only if it satisfies the following condition for an optimized auxiliary variable $q^* = \frac{R_u(\Phi^*, P_b^*)}{P_T(P_b^*)}$, stated as

$$\Xi_d(q^*) = \underset{\{\Phi, P_b\} \in \mathcal{D}}{\text{maximize}} \quad R_u(\Phi, P_b) - q^* P_T(P_b) \tag{3.68}$$

$$= R_u(\Phi^*, P_b^*) - q^* P_T(P_b^*) = 0 \tag{3.69}$$

The Dinkelbach's iterative process yields a globally optimal solution with super-linear speed. The optimized solution of q^* is the solution to original objective of Problem (P4).

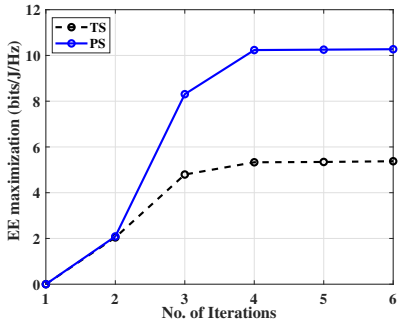


Figure 3.3: Convergence plot of Algorithm 3.2 utilizing Dinkelbach Transform.

The Algorithm 3.2 describes the iterative steps of Dinkelbach based transform for EE maximization, enumerated as follows

Algorithm 3.2 EE Maximization Algorithm based on DT

1: **Initialize:** $\{\Phi^{(1)}, P_b^{(1)}\} \in \mathcal{D}, q^{(1)}=0, j=1, \epsilon$: threshold error.
2: Solve (3.67) for optimal $\Phi^{(j+1)}$ and $P_b^{(j+1)}$.
3: **If** $R_u\left(\Phi^{(j+1)}, P_b^{(j+1)}\right) - q^{(j)} P_T\left(P_b^{(j+1)}\right) \leq \epsilon$, **then** loop stops, go to step 5.
4: **Else** set $q^{(j+1)}=\frac{R_u\left(\Phi^{(j+1)}, P_b^{(j+1)}\right)}{P_T\left(P_b^{(j+1)}\right)}$, $j=j+1$, go to step 2.
5: **Output:** $q^* \leftarrow q^{(j)}$, $\Phi^* \leftarrow \Phi^{(j+1)}$, $P_b^* \leftarrow P_b^{(j+1)}$.

The convergence plot of Algorithm 3.2 is given in Fig. 3.3 for both TS and PS case. If Algorithm 3.2 takes I_1 iterations to converge and step 2 solves with I_2 execution time, then overall computation complexity is $\mathcal{O}(I_1 I_2)$.

The impact of EE and the comparison of Algorithm 3.1 solutions with the KKT results for two distinct objectives of rate and EH maximization, respectively while considering both the TS and PS cases, are discussed in next section of this chapter.

3.6 Results and Discussion

In this section, we assess the effectiveness of the system proposed in this chapter based on the solutions presented. We utilize the ITU-R P.1411-9 site general model for Urban

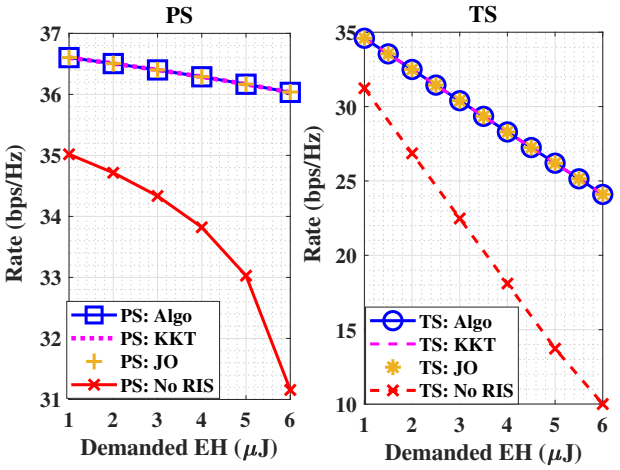


Figure 3.4: Comparison of distinct solutions for rate maximization with demanded EH.

or Sub-urban propagation environment [60, 62] for deriving variance parameter of channels provided in Section 3.2.1. The channel magnitudes follow Rayleigh distribution, while phase angles following uniform distribution of $[-\pi, \pi]$ [22, 57, 60]. The algorithmic results following Algorithm 3.1 are obtained using MATLAB's *fmincon*$(\cdot)$ non-linear solver for averaged 500 Monte-Carlo channel realizations. The validation of the Algorithm 3.1 is proved by the convergence plot given in Fig. 3.2. The specific values of other parameters unless stated are N=3, $\{\eta_{R_{n(i)}}\}_{n,i=1}^{N,M_n}$=$\eta$=0.8, $\mathcal{R}_{th}$=10 bps/Hz, $\mathcal{P}_{\max}$=5W, ξ_{th}=1μJ, E'=2.8mJ, a=1500, b=0.0022. The distance between BS to n^{th} RIS to UE is assumed to be same as d_{BS-R_n}=d_{R_n-UE}=d=5m, RIS's array size $\{M_n\}_{n=1}^{N}$=M=50 or 100 and carrier frequency f = 0.915 GHz ensuring far-field propagation $(d>1m)$ [63]. The effective noise power at UE receiver is W_0^2= $-$ 120 dBm [64]. The considered frequency favors higher power transfer capabilities [60, 65].

Fig. 3.4 and Fig. 3.5 presents the three different types of solutions along with the comparison of TS and PS protocol for maximization of rate and EH respectively. The former belongs to KKT solutions provided in section 3.3 and 3.4, whereas the latter, solution corresponds to the proposed Algorithm 3.1 for solving Problem (P3), depicted as 'Algo' in the

plots. The third solution belongs to the solution by the joint optimization (JO) methodology, in which multiple optimization variables are computed simultaneously. Consequently, for Problem (P3) the dependent variables Φ and P_b are optimized together for selected objective at a time out of four cases of $\mathcal{Z}_x \forall x \in [t, p], \Phi := \{\alpha, \beta\}$ (3.46). This process is complex and provides sub-optimal solution since the adjustment to one variable leads to the compensatory fixtures in other, so as to maximize the objective function. The outcome derived from the joint optimization of parameters could exhibit sub-optimal conditions and is highly reliant on the selection of a feasible initial point. The argument of sub-optimal solution difference is supported by Fig. 3.5 where Algorithm 3.1 and KKT solutions are better than JO solutions. While all three solutions have very negligible difference for the rate case, which implies that all three solutions reach their respective optimality or the problem becomes convex for the selected constant parameters.

In addition, the TS performs inferior to the PS protocol for both rate and EH. As for PS, SWIPT operations are performed for the complete time period with the split in transmit power. For the information rate, this difference in the performance for both the protocols becomes more pronounced at the higher demanded EH. On the other hand, for the EH case this difference is not significant. Fig. 3.4 shows rate and EH trade-off. Fig. 3.5 depicts the appreciation in EH with the maximum allowed transmit power ($\mathcal{P}_{\text{max}}$). Furthermore, the study involves comparison of the outcomes for a scenario denoted as 'No RIS,' which represents the absence of RIS. In the simulations for rate and EH maximization, we consider the absence of RIS by simulating reflections from a concrete wall with a reflectivity of 0.45 [53, 60]. It is worth noting that Algorithm 3.1 is applied with comparable channel coefficients to optimize parameters in the 'No RIS' scenario for both TS and PS. The necessity of intelligent reflections by RIS is highlighted in Fig. 3.4 and 3.5, where 'No RIS' yields least performance for the distinct TS and PS cases, respectively.

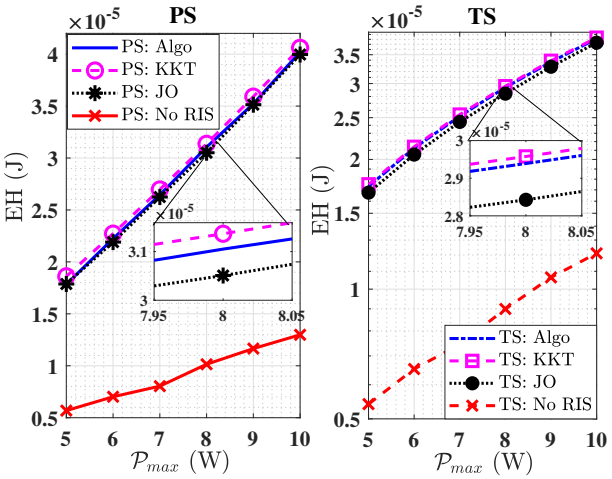


Figure 3.5: Comparison of distinct solutions for EH maximization with maximum transmit power.

In Fig. 3.6, EE maximization is compared for both selection schemes (i.e., ERA and ORA) with EH threshold ξ_{th}. We assume equal elements $\{M_n\}_{n=1}^{N}{=}M$ for all RISs $(N{=}3)$. We observe that ERA selection scheme contributing more to power consumption as all RISs remain ON whereas there will be an increment in channel parameter leading to lesser fading of the signal at UE. The cumulative effect of these two factors for the optimized transmit power and TS or PS ratio, leads to a lesser EE for ERA case than ORA with single 'suitable RIS' selection, as depicted in Fig. 3.6. Again the PS performs better than the TS due to higher data rate delivery and henceforth higher EE. The increase in element from $(M{=}100)$ to $(M{=}150)$ has twin effect on increased P_T, and channel parameter leading to increased rate, which in turn increases the EE. This is because the more elements enable higher data rate which overpowers the negligible circuit power consumption by increased RIS elements. Additionally, EE decreases for higher harvested energy needs which is applicable for all cases.

Fig. 3.7(a) shows higher rate and EH with the increasing number of elements, provided all RIS surfaces $(N{=}3)$ have equal number of elements $(M{=}50$ or $100)$. The increasing M affects the summation in 'channel term' (Z_n) and hence increment in rate and EH. The same

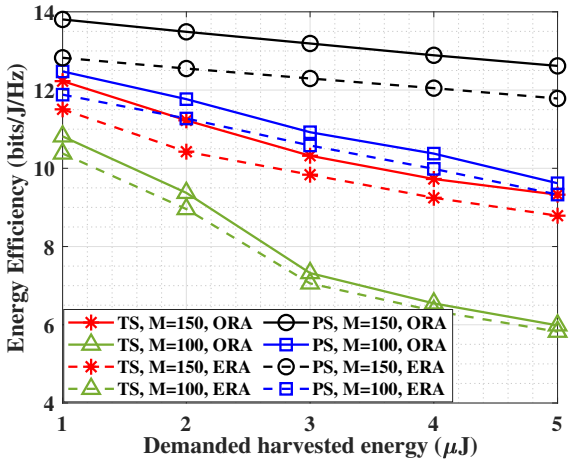
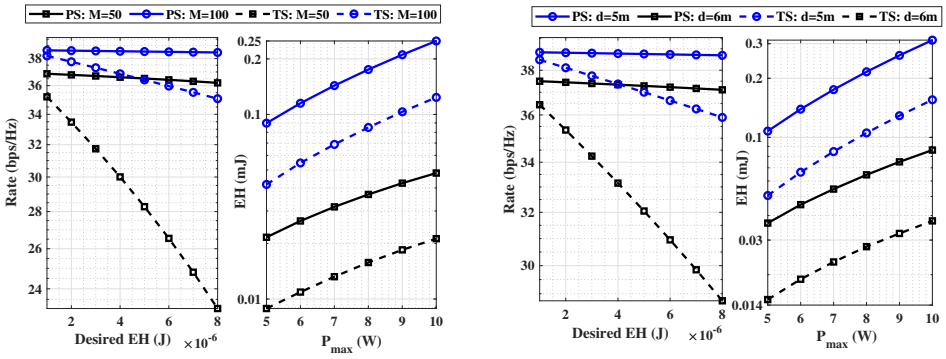


Figure 3.6: ERA and ORA schemes are compared for EE maximization with maximum transmit power to see the impact of increasing RIS elements.



(a) (b)

Figure 3.7: Comparative Rate and EH maximization plots for TS and PS with the variation of (a) Number of RIS elements (assumed to be same for all RIS surfaces) (b) BS $-$ R_n $=$ R_n $-$ UE $=$ d distance.

condition stands true for lower BS-RIS$_n$ or RIS$_n$-UE distance as depicted by Fig. 3.7(b). In the varying network condition due to changed RIS elements or separation distance, the Rate-Energy trade-off stands unaltered. The performance of PS, which is superior to TS, is supported by Fig. 3.7(a)-3.7(b). Variations of distance and elements is huge for the TS rate maximization with demanded EH than for EH maximization.

Fig. 3.8 compares EH for increasing RIS surfaces for different demanded rate. The ERA approach provides significant changes in the EH with surfaces since all are going to

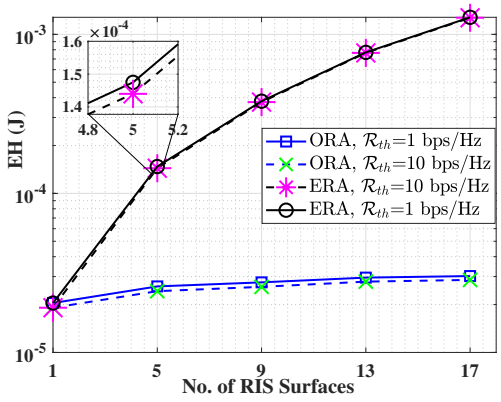


Figure 3.8: EH variations with increased RIS surfaces for ERA and ORA schemes highlighting $\mathcal{R}_{th}$ differences.

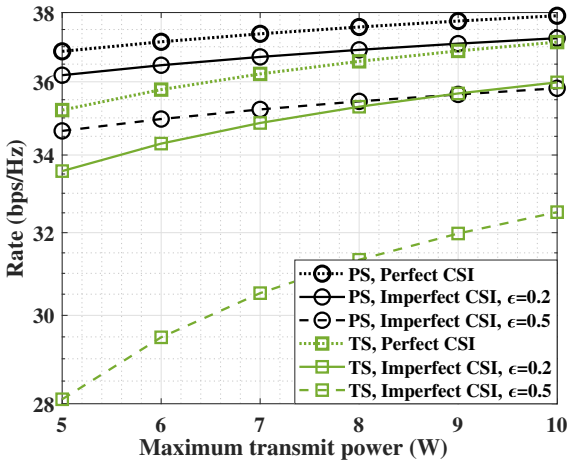


Figure 3.9: Effect of imperfect CSI on rate maximization for both TS and PS.

contribute to the channel parameter. While this change is little less profound for ORA case, yet inlines with the trend of EH increases with more RIS surfaces. The R-E trade-off is again validated for the desired rate of $\mathcal{R}_{th} \in [1, 10]$ bps/Hz.

To assess the robustness of the multi-RIS SWIPT system and associated algorithm to imperfect channel state information, we relax the assumption of perfect channel estimation. Due to the environmental conditions and pilot training overhead the accuracy of CSI estimation can be hampered greatly, leading to imperfect CSI. The small scale channel fading coefficients in (3.1) are $\tilde{g}_{R_{n(i)}}$ and $\tilde{h}_{R_{n(i)}}$. The associated imperfect CSI of these channels are

characterized with Gauss-Markov uncertainty model as [19]

$$\hat{g}_{R_{n(i)}} = \sqrt{1-\epsilon}\,\tilde{g}_{R_{n(i)}} + \sqrt{\epsilon}\,u_{R_{n(i)}}, \quad \hat{h}_{R_{n(i)}} = \sqrt{1-\epsilon}\,\tilde{h}_{R_{n(i)}} + \sqrt{\epsilon}\,v_{R_{n(i)}}. \tag{3.70}$$

The $v_{R_{n(i)}}$ and $u_{R_{n(i)}}$ are i.i.d. complex Gaussian random variables with zero mean and unit variance, showcasing the error variable. Another CSI error parameter is $\epsilon \in [0, 1]$ which indicates the accuracy of the CSI estimation. The unity value of ϵ, implies zero correlation between $\left(\hat{g}_{R_{n(i)}} - \tilde{g}_{R_{n(i)}}\right)$ and $\left(\hat{h}_{R_{n(i)}} - \tilde{h}_{R_{n(i)}}\right)$, while null value is for perfect CSI estimation ($\hat{g}_{R_{n(i)}} = \tilde{g}_{R_{n(i)}}$) and ($\hat{h}_{R_{n(i)}} = \tilde{h}_{R_{n(i)}}$). Fig. 3.9 shows the impact of imperfect CSI on rate maximization for various $\mathcal{P}_{max}$ values for both the TS and PS SWIPT receivers. The amount of rate degrades with increasing value of error factor ϵ from 0.2 to 0.5 by 19% at $\mathcal{P}_{max} = 5$ W. The perfect CSI with $\epsilon = 0$, performs the best with PS receiver. It is worth noting that TS is significantly affected by increasing the CSI error in comparison to the PS, due to high dependency of rate on channel parameter.

3.7 Summary

This chapter investigated a HD SWIPT-enabled multi-RIS communication framework incorporating a practical NL-EH model at the IoT UE. Two RIS utilization strategies, namely, the ERA and ORA, were comparatively analyzed. Separate optimization problems for achievable rate, EH, and EE were formulated for both TS and PS based SWIPT architectures by jointly optimizing the transmit power and TS or PS ratio under the considered system constraints. For rate and EH maximization, closed-form optimal solutions were derived using the KKT conditions. In addition, an alternating optimization-based algorithm was developed, and its performance was compared with the obtained KKT solutions as well as the jointly optimized parameter solutions. The fractional EE maximization prob-

lem was addressed using the Dinkelbach transformation technique. The obtained results demonstrated that all three optimization approaches achieve nearly identical performance in terms of achievable rate, whereas the KKT-based solution provides slightly superior EH performance compared to the other methods. The analysis also highlights the impact of RIS power consumption and demonstrated the resource-saving capability of the ORA scheme through an intelligent RIS selection. Furthermore, the study revealed that higher throughput and improved harvested energy can be achieved by increasing the number of RIS surfaces, increasing the number of RIS elements, allowing higher transmit power limits while reducing the separation distance between communicating entities. An imperfect CSI analysis was also carried out to evaluate the robustness of the proposed framework under practical channel estimation errors. As a possible extension of this work, the ideal continuous phase-shift assumption may be replaced with practical discrete phase-shift modeling. Moreover, the considered framework can be extended to multi-user scenarios with user scheduling and resource allocation strategies for further investigation.

Chapter 4

Joint Rate-Energy Optimization in RIS-assisted SWIPT-IoT System

In this chapter, we address the conflicting objectives, namely, data rate and energy harvesting (EH), in Simultaneous Wireless Information and Power Transmission (SWIPT) systems with Reconfigurable Intelligent Surface (RIS) by introducing a weighted optimization objective, aiming to jointly maximize data rate, EH, and transmit power utilization. This approach involves optimizing power splitting (PS) ratios and transmit power under practical phase-dependent amplitude model for each RIS element reflectivity. To tackle this, fractional programming-based Dinkelbach and Quadratic transform-related algorithms are proposed and compared with Karush-Kuhn-Tucker (KKT) conditions based solutions. Impact of discrete phase shift (DPS) RIS model has been analyzed as well. Numerical results show that deploying more RIS elements and placing them closer together enhances both information rate and EH, whereas it nearly saturates with increasing DPS levels.

The chapter is organized as follows: Section 4.1 provides an introduction to the considered framework and Section 4.2 gives the description of the system model encapsulating the signal modeling and phase shift models. Section 4.3 presents maximization problem of UF and related solutions. The results and related discussions are scripted in Section 4.4. The

chapter finally rests with concluding remarks in Section 4.5.

4.1 Introduction to Fractional Programming Strategy in RIS-assisted SWIPT-IoT Systems

With the proliferation of IoT devices across various sectors like agriculture and healthcare, there is a pressing need for sustainable systems with reliable data throughput and low energy consumption. SWIPT systems, capable of harvesting RF energy for both data transfer and power, can address these demands effectively [8]. Integration of SWIPT with RIS holds great potential to serve as autonomous green communication systems for future IoT applications [66]. SWIPT systems inherently face a trade-off between data rate and EH, prompting the need for of this study. Table 4.1 highlights the recent works on RIS-SWIPT systems and their distinguished features regarding used EH model (linear or non-linear EH model), objective function (maximization or minimization problem statement), SWIPT architecture used (TS, PS, or separated EH and information decoding users) and the phase shift model.

It is observed that most works ([67],[69]-[51],[15]-[72]) considering multiple objective functions (or weighted sum of objectives) have assumed linear EH model, which lacks practical implementation. As the very basic component of EH circuit, the rectenna (rectifier plus antenna) is assumed to have a linear energy conversion efficiency when estimated via linear EH models. It contrasts with the presence of non-linear element rectifier (having diode) which questions the suitability of the model. To the contrary the sigmoid or logistic based non-linear EH (NL-EH) model practically justifies the RF-to-DC conversion of EH module [32, 53], therefore this chapter utilizes the same sigmoidal model. However, due to the complicated mathematical representation of sigmoid NL-EH model, it brings non-convexity to

Table 4.1: Recent studies on RIS-SWIPT systems.

Ref.	**EH Model**	**Objective Function**	**SWIPT architecture**	**Phase shift model**
[67]	Linear	Sum power maximization	Separated EH-ID users	Continuous
[68]	NL-EH	Rate Maximization	PS	Continuous
[69]	Linear	Multi-objective optimization (MOO) for rate and EH	PS	No RIS
[70]	Linear	EE maximization	Separated EH-ID users	Continuous
[43]	Linear	weighted rate and EH	PS	Practical*
[51]	Linear	EE maximization	PS	Continuous
[45]	NL-EH	Performance analysis	TS/PS	Discrete
[15]	Linear	Maxmin SNR	Separated EH-ID users	Discrete
[71]	Linear	Sum rate Maximization	Separated EH-ID users	Discrete
[72]	Linear	MOO rate and EH	Separated EH-ID users	Continuous
[73]	NL-EH	Total energy Maximization	PS	Continuous
[44]	NL-EH	Sum rate Maximization	-	Continuous
Present work	NL-EH	Weighted rate, EH, and power	PS	Practical* + Discrete

* Phase shift dependent reflection amplitude practical model.

the optimization problem involved and the direct solution is not easy to achieve. Another notable contribution is incorporation of the practical phase shift model with discrete phase shift. In the practical circuit implementations, the characteristics of the amplitude and phase responses of the RIS reflecting elements are inter-dependent, i.e., the reflection amplitude response $\{\eta_i(\theta_i) \in (0, 1]\}$ varies across different phase shifts $\{\theta_i \in [-\pi, \pi)\}$. This is due to the non-uniform nature of lumped circuit comprising the capacitor, inductor, and resistor, thereby modeling individual reflecting element of RIS, and thus affecting the respective reflection coefficient's amplitudes as well as phases. The existing works [67], [68], [70], [51], [44, 72, 73] on RIS-SWIPT communications are mainly based on the assumption of continuous phase shifts at its reflecting elements. However in practice, this is difficult to realize since manufacturing of each reflecting element with more levels of phase shifts incurs a relatively higher cost, which may not be scalable since the number of elements for RIS

is usually very large. This does not only make the element design more challenging due to its limited size, but also requires extra controlling pins at the RIS controller to invoke more PIN diodes. Hence we take the practical case where each element of the RIS has only a finite number of discrete phase shifts. Later, we analyze the impact of the number of phase shift levels required to achieve desired objective function.

Moreover, the present chapter considers three problems together as their weighted versions of rate, EH, and transmit power, termed as utility function (UF). It is defined as a fraction of weighted sums of Rate-EH over Power, which is the reflection of energy efficiency (EE) metric. This formulated objective function is unique in a way that results can be inferred from the view point of EE, individual rate, individual EH or sum of rate, and EH just by adjusting the weights accordingly. Whereas in literature such kind of weighted objective problems are tackled by only very limited works [70].

This chapter bridges the aforementioned gap by exploring realistic non-linear EH (NL-EH) models in SWIPT communication with RIS for weighted joint optimization problem addressing rate, EH, and transmit power together, listed below.

- At the IoT user, the PS-SWIPT protocol incorporates a logistic or sigmoid-based NL-EH model. Additionally, a functional phase shift model that depicts the amplitude variation dependent on phase in the design of element-wise reflection is incorporated.

- Three different solution strategies are proposed for the weighted maximization problem. First solution type involves the Karush-Kuhn-Tucker (KKT) conditions. Other two are fractional programming (FP) based Dinkelbach and Quadratic transform algorithms. We additionally analyze the impact of the DPS levels on the system performance.

- The proposed algorithmic results are analytically compared for their efficient and fast

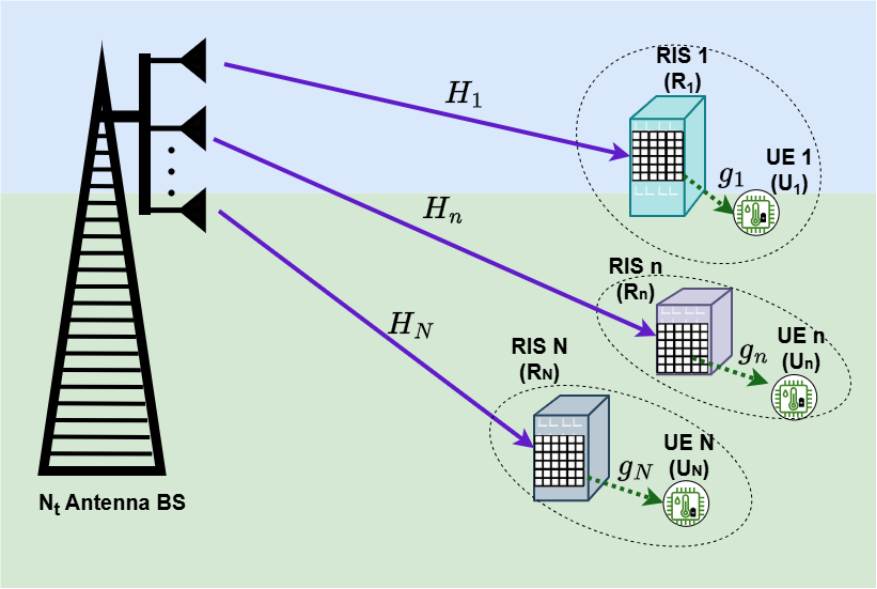


Figure 4.1: System model for RIS assisted PS-SWIPT communication.

convergence. Inferences are drawn based on the variation of the number of RIS elements, separation distance, maximum allowed transmit power, desired rate and DPS levels.

4.2 System Model

The system model depicted in Fig. 4.1 illustrates N_t antenna base station (BS) communicates with a N single antenna PS-SWIPT operated IoT user equipment (UE) ($U_n, n = 1, 2, \ldots, N$). [1] To facilitate the communication process to the secluded UE, each one is supported by an M element RIS, such that there are N RIS-UE pairs. Each antenna is assumed be active for an equal fraction of overall transmission time serving each RIS-UE pair. The direct communication path between BS and U_n is assumed to be obstructed. Let us assume that all the RISs have equal elements, i.e., $M_1{=}\ldots{=}M_n{=}\cdots{=}M_N{=}M$. The channel from

[1]The present system model can be taken as a specific case where a dedicated RIS is communicating with a user group (UG), from which any one UE is selected (as shown in Fig. 4.1) using random scheduling, making a RIS-user pair with no interference. However, it can be further extended when BS is broadcasting or multicasting to all the UEs of a UG.

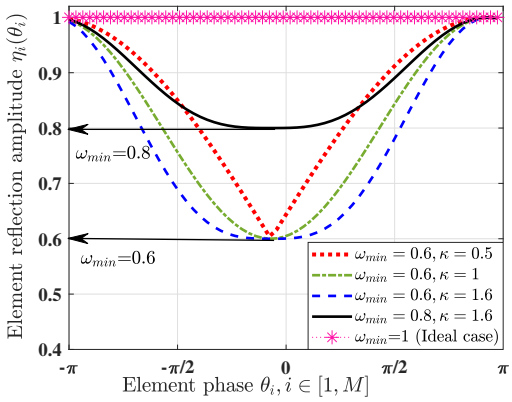


Figure 4.2: Reflection amplitude dependency on phase with circuit constants.

BS to n^{th} RIS is $\mathbf{H}_n = [\mathbf{h}_1^n, \ldots, \mathbf{h}_{n_t}^n, \ldots, \mathbf{h}_{N_t}^n] \in \mathbb{C}^{M \times N_t}$ where $\mathbf{h}_{n_t}^n = [h_{n_t,1}^n, \ldots, h_{n_t,M}^n]^T$. The channel between n^{th} RIS-UE pair is $\mathbf{g}_n = [g_1^n, \ldots, g_M^n] \in \mathbb{C}^{1 \times M}$. Let $\{|h_{nt,i}^n|, \phi_i\}$ and $\{|g_i^n|, \psi_i\}$ for $i \in [1, \ldots, M]$ denote the set of related channel magnitude and phases.

4.2.1 Practical Phase Shift Model

In the practical circuit implementations, the non-uniformity of lumped circuit models influence each RIS reflecting element, impacting both the amplitude $\{\eta_i \in (0, 1]\}$ and the phase $\{\theta_i \in [-\pi, \pi)\}$ of their respective reflection coefficients. The phase dependent reflection coefficient amplitude for the i^{th} RIS element is analytically provided as follows [74]

$$\eta_i(\theta_i) = (1 - \omega_{min})(0.5(\sin(\theta_i - \varpi) + 1))^{\kappa} + \omega_{min}. \tag{4.1}$$

For all M elements of the RIS, the circuit parameters: $\omega_{min}, \varpi, \kappa$ are non-negative constants. The reflection amplitude is illustrated in Fig. 4.2 for different phase values, as derived from equation (4.1). Here, ω_{min} represents the minimum amplitude, and κ characterizes the slope of the curve. When the phase is π or $-\pi$, the reflectivity reaches its maximum amplitude of unity, whereas it attains least value (ω_{min}) at $\theta_i = 0$.

The desired phase condition, where all individual reflection coefficients $\eta_i(\theta_i)$ equal 1

for i ranging from 1 to M, can be achieved by setting either $\kappa = 0$ or $\omega_{min} = 1$.

4.2.2 Signal Model

In this section, we introduce the mathematical rigor considering the received signal, SNR, data rate, and harvested energy by the respective UE(s). Following (4.1), the phase shift matrix is given as $\mathbf{\Theta}_n = \text{diag}[\eta_1(\phi_1)e^{j\phi_1}, \ldots, \eta_M(\phi_M)e^{j\phi_M}]$, $\eta_i(\theta_i) = (1-\omega_{min})(0.5(\sin(\theta_i - \varpi)+1))^{\kappa} + \omega_{min}$ is a function determining the relationship between the phase and amplitude of the reflection coefficient [74]. Assuming equal weights at all BS antennas, it transmits $\mathbf{x} = \sum_{n=1}^{N} \mathbf{P}_n s_n$ signal, where $\mathbf{P}_n = \sqrt{\frac{P_b}{N_t}}[1, \ldots, 1]_{N_t \times 1}$ represents the precoding vector for n^{th} RIS-UE pair with a total BS power represented by P_b. The related transmitting symbol is denoted by s_n with $\mathbb{E}[|s_n|^2] = 1$. The signal received at U_n via intelligent reflections from R_n is $y_n = \mathbf{g}_n \mathbf{\Theta}_n \mathbf{H}_n \mathbf{x} + w_n$, where $w_n \sim \mathcal{CN}(0, W_0^2)$ is the (i. i. d.) additive white Gaussian noise (AWGN). To avoid interference, each BS antenna is tuned to any one RIS-UE pair, which makes $N_t = N$. The present signal model is simplified to replicate a single-input single output (SISO) system, with single antenna BS having a power represented as a fraction of P_b to N_t (i.e., P_b/N_t) for communicating with single antenna UE via single RIS. Henceforth, refined received signal y_n is given by

$$y_n = \left(\sum_{i=1}^{M} g_i^n h_{n_t,i}^n \eta_i(\theta_i) e^{j(\theta_i + \phi_i + \psi_i)} \right) \sqrt{\frac{P_b}{N_t}} \sum_{j=1}^{N} s_j + w_n. \tag{4.2}$$

The ideal phase shift $\theta_i^* = -(\phi_i + \psi_i)$ for the i^{th} RIS element aligns with channel phases, enhancing SNR at U under the assumption of perfect CSI, detailed in [22] as follows[2]

$$\Gamma_n = \frac{P_t}{W_0^2} \left| \sum_{i=1}^{M} |g_i^n||h_{n_t,i}^n| \eta_i(\theta_i^*) e^{j(\theta_i^*)}) \right|^2 = \frac{P_t Z_n}{W_0^2}, \tag{4.3}$$

[2] $\theta_i^* = -(\phi_i + \psi_i)$ is for continuous phase shift (CPS), while there exists quantization error for DPS such that $\theta_i^* = \Delta\theta_i$, where $\Delta\theta_i \in \mathcal{U}(-\pi/L, \pi/L)$ for levels $L = 2^b$ and b bits.

where $P_t = P_b/N_t$ is defined as the power at each BS antenna serving related RIS-user pair. The n^{th} user U_n is equipped with PS-SWIPT architecture having a PS factor β. The practical sigmoid function based NL-EH and data rate are respectively given by [53]

$$E_h = \frac{E'}{1-\chi}\left(\frac{1}{1+\exp(-\beta a P_t Z_n + ab)} - \chi\right), \tag{4.4}$$

$$R_u = \log_2(1 + (1-\beta)\Gamma_n). \tag{4.5}$$

The values of the constant parameters (E', a, b) are typically determined through the utilization of a curve-fitting tool applied to the analytical data, as discussed in [31], with $\chi = (1+\exp(ab))^{-1}$. In the subsequent section, we formulate the primary problem concerning the overall maximization of weighted joint objective function.

4.2.2.1 Discrete Phase Shift Model

While the theoretical model considers CPS with an infinite number of levels, practical hardware implementations use PIN diodes to facilitate phase changes and beamforming. Each PIN diode represents a bit b, with the number of discrete phase shift levels L given by $L = 2^b$. As L increases, so does the number of elements in $\mathcal{S}$, which becomes infinite for CPS. Using a large number of PIN diodes (more than 100) for phase adjustment makes the RIS module bulky and challenging to implement. Thus unlike the CPS model, the practical DPS level requires finite control bits for providing distinct phases at each RIS element. The discrete levels belong to the set $\mathcal{S} = \{0, 2\pi/L, \ldots, 2\pi(L-1)/L\}$ [15]. For each reflecting element, the optimum phase shift $\theta_i^* = -(\phi_i + \psi_i)$ value is mapped to its nearest set $\mathcal{S}$ element $(\hat{\theta}_i)$. The evident effect on channel parameter by the phase error $\Delta\theta_i = \hat{\theta}_i - \theta_i^*$ is given by

$$Z_n = \left| \sum_{i=1}^{M} |g_i^n||h_{nt,i}^n|\eta_i(\Delta\theta_i)e^{j(\Delta\theta_i)}) \right|^2. \tag{4.6}$$

A DPS model with many levels approximates a CPS model with zero phase error ($\Delta\theta_i = 0$).

4.3 Problem Formulation and Proposed Solution

We formulate a problem with a weighted utility function (UF) to collectively optimize the data rate, EH, and transmit power. This fractional UF $\mathcal{J}(\beta, P_t)$ has been used in literature as an interpretation to effective efficiency for information transfer (EEIT) or effective energy efficiency transmission (EEET) which is the ratio of rate to power or EH to power, an important QoS metric [43, 75].[3] This optimization aims to guarantee that both the demanded data rate and EH at the UE exceed specified thresholds. The comprehensive optimization problem analytically expressed as

$$\text{(P1): } \underset{\beta, P_t}{\text{maximize}} \qquad \mathcal{J}(\beta, P_t) = \frac{w_r R_u(\beta, P_t) + w_e E_h(\beta, P_t)}{w_p P_t} \tag{4.7}$$

$$\text{subject to :} \qquad \text{(C1): } R_u \geq \mathcal{R}_{th}, \quad \text{(C2): } E_h \geq \xi_{th}, \tag{4.8}$$

$$\text{(C3): } P_t \leq \mathcal{P}_{max}, \quad \text{(C4): } 0 \leq \beta \leq 1. \tag{4.9}$$

where the demanded rate and EH are $\mathcal{R}_{th}$ and ξ_{th}, respectively. $\mathcal{P}_{max}$ denotes the power limit on each antenna. The constants w_r, w_e, and w_p represent the weighting factors associated with the data rate, EH, and transmit power, respectively. These non-negative weights are decided by the network operator based on the pricing which controls the trade-off depends on the priority for ID or EH [43]. As w_r is indicative of currency units/bps/Hz normalized by per bps/Hz units of spectral efficiency (data rate). The weight factor w_e indicates currency units/μJ, normalized by per μJ units of energy. Even though there is no exact pricing metric for the EH in practice, however the related works on SWIPT at IoT user provided typical range of EH between μJ or nJ. Thus, we anticipate that the future pricing metric for har-

[3] As an alternative, same fractional objective function can be equivalently represented as a tractable Quadratic transform [76] which is discussed in subsequent subsection.

vested energy will be close to our assumption of w_e [77]. The power weight w_p is taken as unity which helps to convert the objective function to EE problem (ratio of rate and power) by adjusting weights [51]. Considering the objective function, in pursuit of the crucial Rate-Energy (R-E) trade-off in SWIPT systems, the optimizer aims to find an equilibrium point between the two metrics, namely data rate and EH, ensuring both are maximized according to the stringent constraints. Subsequently, we seek potential solution(s) of (P1), with (some) relevant possibilities as discussed in the following parts.

4.3.1 KKT Conditions based Solution

The problem (P1) is difficult to solve since it has a non-convex form; therefore we employ KKT based solution characterization and identify the locally optimal or stationary candidate solutions under considered constraints [20]. Therefore, as the initial step to obtain an analytical solution for the joint objective optimization problem in (P1), we represents the corresponding Lagrangian function as follows.

$$L(\beta, P_t; \mathbf{\Lambda}) = \mathcal{J}(\beta, P_t) + \lambda_1(R_u - \mathcal{R}_{th}) + \lambda_2(E_h - \xi_{th}) + \lambda_3(\mathcal{P}_{\max} - P_t) + \lambda_4(1-\beta). \quad (4.10)$$

The expression $\Delta\mathcal{L}(\beta, P_t; \mathbf{\Lambda}) = 0$, ensures the fulfillment of the (local or global) optimal conditions $\frac{\partial\mathcal{L}(\beta,P_t;\mathbf{\Lambda})}{\partial P_t} = \frac{\partial\mathcal{L}(\beta,P_t;\mathbf{\Lambda})}{\partial\beta} = 0$.

$$(1-\beta)Z'\Sigma_r + \beta Z''\Sigma_e - \frac{w_r R_u}{w_p P_t^2} - \frac{w_e E_h}{w_p P_t^2} - \lambda_3 = 0, \quad (4.11)$$

$$-P_t Z'\Sigma_r + P_t Z''\Sigma_e - \lambda_4 = 0, \quad (4.12)$$

where $Z' = \frac{Z_n}{\log(2)(W_0^2 + P_t(1-\beta)Z_n)}$, $\Sigma_r = \left(\frac{w_r}{w_p P_t} + \lambda_1\right)$, $Z'' = \left(\frac{E'}{1-\chi}\right)\left(\frac{aZ_n \exp(-a\beta P_t Z_n + ab)}{(1+\exp(-a\beta P_t Z_n + ab))^2}\right)$ and $\Sigma_e = \left(\frac{w_e}{w_p P_t} + \lambda_2\right)$. Feasible conditions encompass $R_u - \mathcal{R}_{th} \geq 0$, $E_h - \xi_{th} \geq 0$, $\mathcal{P}_{\max} - P_t \geq 0$, and $1 - \beta > 0$. Complementary slackness conditions are expressed as

Table 4.2: KKT cases for UF maximization.

KKT cases	**Sol.**	**Remark**
$\lambda_1{=}0{\Rightarrow}R_u(\beta,P_t){\neq}\mathcal{R}_{th}$; $\lambda_2{=}0{\Rightarrow}$ $E_h(\beta,P_t){\neq}\xi_{th}$; $\lambda_3{=}0{\Rightarrow}(\mathcal{P}_{\max}-P_t){\neq}0$	$\mathbf{\Lambda}=-\text{ve}$	not possible
$\lambda_1{=}0{\Rightarrow}R_u(\beta,P_t){\neq}\mathcal{R}_{th}$; $\lambda_2{=}0{\Rightarrow}$ $E_h(\beta,P_t){\neq}\xi_{th}$; $\lambda_3{\neq}0{\Rightarrow}(\mathcal{P}_{\max}-P_t){=}0$	$\mathbf{\Lambda}=-\text{ve}$	not possible
$\lambda_1{=}0{\Rightarrow}R_u(\beta,P_t){\neq}\mathcal{R}_{th}$; $\lambda_2{\neq}0{\Rightarrow}$ $E_h(\beta,P_t){=}\xi_{th}$; $\lambda_3{=}0{\Rightarrow}(\mathcal{P}_{\max}-P_t){\neq}0$	$\mathbf{\Lambda}=-\text{ve}$	not possible
$\lambda_1{=}0{\Rightarrow}R_u(\beta,P_t){\neq}\mathcal{R}_{th}$; $\lambda_2{\neq}0{\Rightarrow}$ $E_h(\beta,P_t){=}\xi_{th}$; $\lambda_3{\neq}0{\Rightarrow}(\mathcal{P}_{\max}-P_t){=}0$	$\mathbf{\Lambda}=-\text{ve}$	not possible
$\lambda_1{\neq}0{\Rightarrow}R_u(\beta,P_t){=}\mathcal{R}_{th}$; $\lambda_2{=}0{\Rightarrow}$ $E_h(\beta,P_t){\neq}\xi_{th}$; $\lambda_3{=}0{\Rightarrow}(\mathcal{P}_{\max}-P_t){\neq}0$	$\mathbf{\Lambda}=-\text{ve}$	not possible
$\lambda_1{\neq}0{\Rightarrow}R_u(\beta,P_t){=}\mathcal{R}_{th}$; $\lambda_2{=}0{\Rightarrow}$ $E_h(\beta,P_t){\neq}\xi_{th}$; $\lambda_3{\neq}0{\Rightarrow}(\mathcal{P}_{\max}-P_t){=}0$	P_{t1} (4.13) β_1	possible
$\lambda_1{\neq}0{\Rightarrow}R_u(\beta,P_t){=}\mathcal{R}_{th}$; $\lambda_2{\neq}0{\Rightarrow}$ $E_h(\beta,P_t){=}\xi_{th}$; $\lambda_3{=}0{\Rightarrow}(\mathcal{P}_{\max}-P_t){\neq}0$	P_{t2} (4.14) β_2	possible
$\lambda_1{\neq}0{\Rightarrow}R_u(\beta,P_t){=}\mathcal{R}_{th}$; $\lambda_2{\neq}0{\Rightarrow}$ $E_h(\beta,P_t){=}\xi_{th}$; $\lambda_3{\neq}0{\Rightarrow}(\mathcal{P}_{\max}-P_t){=}0$	P_{t3} β_3	possible

$\lambda_1(R_u-\mathcal{R}_{th})=0$, $\lambda_2(E_h-\xi_{th})=0$, $\lambda_3(\mathcal{P}_{\max}-P_t)=0$, and $\lambda_4(1-\beta)=0$. Lagrangian and optimizing variables must be positive, i.e., $\{\mathbf{\Lambda},\beta,P_t\}>0$. Considering the KKT complementary slackness conditions, it is evident that λ_4 must be zero, implying $\beta\neq 1$. Analyzing (4.11)-(4.12) for UF maximization, all the feasible solution of KKT are tabulated in Table 4.2. It takes a total of eight cases among which three viable cases exists and its solution is provided in detailed Lemma $1{-}3$.

Lemma 1: If $\lambda_1{\neq}0{\Rightarrow}(R_u-\mathcal{R}_{th}){=}0$; $\lambda_2{=}0{\Rightarrow}(E_h-\xi_{th}){\neq}0$; $\lambda_3{\neq}0{\Rightarrow}(\mathcal{P}_{\max}-P_t){=}0$, and the optimal values are

$$P_{t_1}=\mathcal{P}_{\max},\ \ \beta_1=1-\frac{W_0^2(2^{\mathcal{R}_{th}}-1)}{\mathcal{P}_{\max}Z_n}. \qquad \blacksquare \qquad (4.13)$$

Lemma 2: If $\lambda_1{\neq}0{\Rightarrow}(R_u-\mathcal{R}_{th}){=}0$; $\lambda_2{\neq}0{\Rightarrow}(E_h-\xi_{th}){=}0$; $\lambda_3{=}0{\Rightarrow}(\mathcal{P}_{\max}-P_t){\neq}0$, and

the optimal values are

$$P_{t_2} = \frac{W_0^2(2^{\mathcal{R}_{th}} - 1) + b}{Z_n} - \frac{\ln(\Sigma)}{a}, \quad \beta_2 = \frac{ab - \ln(\Sigma)}{aW_0^2(2^{\mathcal{R}_{th}} - 1) + ab - \ln(\Sigma)}, \tag{4.14}$$

where $\Sigma = \left(\frac{(1-\chi)(E'-\xi_{th})}{\xi_{th}(1-\chi)+\chi E'}\right)$. ■

Lemma 3: If $\lambda_1 \neq 0 \Rightarrow (R_u - \mathcal{R}_{th}) = 0$; $\lambda_2 \neq 0 \Rightarrow (E_h - \xi_{th}) = 0$; $\lambda_3 \neq 0 \Rightarrow (\mathcal{P}_{\max} - P_t) = 0$, and the optimal values are

$$P_{t_3} = \mathcal{P}_{\max}, \;\; \beta_3 = \max\left(\beta_1, \frac{1}{\mathcal{P}_{max} Z_n}\left(b - \frac{\ln(\Sigma)}{a}\right)\right). \quad ■ \tag{4.15}$$

To summarize the solutions given in Lemma 1-3, we introduce the following Algorithm 4.1, termed as UF maximization with KKT solutions, aimed at maximizing the weighted UF (P1). The execution-complexity of Algorithm 4.1 is $\mathcal{O}(M^2)$.

Algorithm 4.1 UF maximization with KKT solutions

1: **Input:** $Z_n, a, b, E', W_0^2, \mathcal{R}_{th}, \xi_{th}, \mathcal{P}_{max}$.
2: Compute P_{t_1} and β_1 (4.13), hence find $\mathcal{J}_1(P_{t1}, \beta_1)$.
3: Compute P_{t_2} and β_2 (4.14), subsequently find $\mathcal{J}_2(P_{t2}, \beta_2)$.
4: Compute P_{t_3} and β_3 (4.15), thereby find $\mathcal{J}_3(P_{t3}, \beta_3)$.
5: **Output:** $\mathcal{J}_{opt}$ = max$(\mathcal{J}_1, \mathcal{J}_2, \mathcal{J}_3)$.

4.3.2 Dinkelbach based Solution

As previously mentioned, the primary problem (P1) entails a non-linear FP problem, which is non-convex and poses challenges for direct solution. In such a case, the Dinkelbach transform (DT) proves useful for tackling this difficulty. Hence, we convert the objective function from its fractional form to a difference of numerator and quasi-denominator form [76]. We define

$$\mathcal{J}_N(\beta, P_t) = w_r R_u(\beta, P_t) + w_e E_h(\beta, P_t), \quad \mathcal{J}_D(P_t) = w_p P_t, \tag{4.16}$$

$$\mathcal{Q}(\beta, P_t) = \frac{\mathcal{J}_N(\beta, P_t)}{\mathcal{J}_D(P_t)}. \tag{4.17}$$

The transformed problem (P1) for a given auxiliary variable q with iterative adaptation is represented as

$$\text{(P2): } \underset{\beta, P_t}{\text{maximize}} \quad \mathcal{J}_N(\beta, P_t) - q\mathcal{J}_D(P_t) \tag{4.18}$$

$$\text{subject to :} \quad \text{(C1) - (C4).} \tag{4.19}$$

The proposed Algorithm 4.2 solves the DT based FP problem while solving dual variables employing divide-and-conquer (DAC) approach [78].

Algorithm 4.2 Dinkelbach based Algorithm

1: **Initialize:** $\{\beta^{(1)}, P_t^{(1)}\} \in \mathcal{D}, q^{(1)} = \mathcal{Q}(\beta^{(1)}, P_t^{(1)}), i = 1, \epsilon_r$: threshold error.
2: Solve (P2) in (5.18) to find optimal $\beta^{(i+1)}$ and $P_t^{(i+1)}$ using Algorithm 4.4.
3: **If** $\mathcal{J}_N\left(\beta^{(i+1)}, P_t^{(i+1)}\right) - q^{(i)}\mathcal{J}_D\left(P_t^{(i+1)}\right) \leq \epsilon_r$, **then** loop stops, go to step 5.
4: **Else** set $q^{(i+1)} = \mathcal{Q}(\beta^{(i+1)}, P_t^{(i+1)})$, $i = i + 1$, go to step 2.
5: **Output:** $q^* \leftarrow q^{(i)}$, $\beta^* \leftarrow \beta^{(i+1)}$, $P_t^* \leftarrow P_t^{(i+1)}$.

The initial values of $\{\beta, P_t\}$ lie within the domain $\mathcal{D}$ defined by constraints (C1) - (C4) (4.19). However, due to the ongoing non-convexity of the problem in (P2), obtaining an optimal solution directly through joint optimization is challenging. Thus, it is advisable to explore alternative approaches to find a suitable solution. One effective strategy involves optimizing a single parameter while keeping the others fixed, which often leads to convexity in the problem. This alternating parameter-based optimization technique has shown effectiveness in solving individual rate, EH, or transmit power-related objective functions [53]. Consequently, an AO based Algorithm (step 2) is provided in Algorithm 4.4, which decomposes the complex problem into sub-problems and solves them using the DAC approach.

4.3.3 Quadratic Transform based Solution

The Quadratic Transform (QT), inspired by DT, introduces an additional optimization variable to the FP based solution, ensuring the objective function remains unchanged [76].

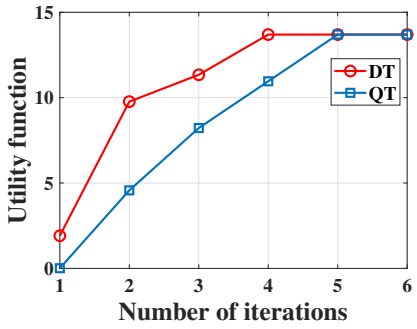


Figure 4.3: Convergence plot of UF maximization by DT and QT approach, utilizing Algorithms 4.2 and 4.3, respectively.

Unlike DT, which yields an optimal value at q^*, QT presents a more interpretable solution through its enhanced objective function, offering the optimum value. This transformation of (P1) is evident in the modified problem formulation (P3), which incorporates an additional variable s in alignment with the principles of QT.

$$\text{(P3): } \underset{\beta,P_t,s}{\text{maximize}} \quad 2s\sqrt{\mathcal{J}_N(\beta,P_t)} - s^2\mathcal{J}_D(P_t) = G(\beta,P,s) \tag{4.20}$$

$$\text{subject to:} \quad \text{(C1) - (C4)}, \ s \in \mathbb{R}. \tag{4.21}$$

The QT problem (P3) is concave maximization problem over $\{\beta, P_t\}$. Algorithm 4.3 efficiently deals with finding the optimal $\{\beta, P_t\}$, summarized below.

Algorithm 4.3 Quadratic transform based Algorithm

1: **Initialize:** $\{\beta, P_t\} \in \mathcal{D}$.
2: **REPEAT**
3: Update $s = \frac{\sqrt{\mathcal{J}_N(\beta,P_t)}}{\mathcal{J}_D(P_t)}$.
4: Solve (P3) with fixed s from step 3 for optimal $\{\beta, P_t\}$ using Algorithm 4.4.
5: Until **CONVERGENCE**

Similar to Algorithm 4.2 (step 2), for solving the complex (P3), an intermediate AO Algorithm 4.4 is invoked (step 4), which satisfactorily solves via DAC approach. From Fig. 4.3, a comparison is made between the DT approach following Algorithm 4.2, and QT by Algorithm 4.3, for maximizing the UF. It is notable that the DT demonstrates faster conver-

gence (i.e., nearly 4 iterations) as claimed to be converging at super-linear rate [76], while QT is little slower (converging in approximately 5 iterations). This observation aligns with the convergence rate analysis presented in [76]. The computation time for Algorithm 4.4 with I_A iteration is $(I_A\big(\kappa_1(M^2)+\kappa_2(M^2))))$. The iterations required for DT and QT are I_D and I_Q, respectively. Thus overall asymptotic polynomial time computation complexity for Algorithms 4.2 and 4.3 are $\mathcal{O}(I_D I_A(\kappa_1(M^2)+\kappa_2(M^2)))$ and $\mathcal{O}(I_Q I_A(\kappa_1(M^2)+\kappa_2(M^2)))$, respectively.

4.3.4 Intermediate Algorithmic Solution

The intermediate AO based algorithm involved in solving the Algorithms 4.2 and 4.3 involves divide-and-conquer approach. Since transformed Problem (P2) and (P3) still poses non-convexity due to interlinked dual variables β and P_t, thus to solve either of them iteratively, we break complex optimization problem into two single variable sub-problem(s). Since both (P2) and (P3) have the same set of constraints, we define a metric $\mathcal{Z}_x$ which takes either the objective function of (P2) as in (5.18) or (P3) as in (5.53) at once.

$$\underset{\forall x\in[d,q]}{\mathcal{Z}_x(\beta,P_t)}:=\begin{cases}\mathcal{Z}_d=\mathcal{J}_N(\beta,P_t)-q\mathcal{J}_D(P_t) & :\text{ for (P2)}\\ \mathcal{Z}_q=2s\sqrt{\mathcal{J}_N(\beta,P_t)}-s^2\mathcal{J}_D(P_t) & :\text{ for (P3)}\end{cases} \tag{4.22}$$

The sub-problems are defined respectively as.

$$\text{(P4): } \underset{\beta}{\text{maximize}} \quad \mathcal{Z}_x(\beta,P_t)\ \forall x\in[d,q] \tag{4.23}$$

$$\text{subject to :} \quad \beta\geq\frac{1}{P_tZ_n}\left(b-\frac{\ln\Sigma}{a}\right), \tag{4.24}$$

$$\beta\leq 1-\frac{W_0^2}{P_tZ_n}(2^{\mathcal{R}_{th}}-1), \tag{4.25}$$

$$0\leq\beta\leq 1. \tag{4.26}$$

$$\text{(P5): maximize}_{P_t} \quad \mathcal{Z}_x(\beta, P_t)\ \forall x \in [d, q] \tag{4.27}$$

$$\text{subject to :} \quad P_t \geq \frac{1}{\beta Z_n}\left(b - \frac{\ln \Sigma}{a}\right), \tag{4.28}$$

$$P_t \geq \frac{W_0^2}{(1-\beta)Z_n}(2^{\mathcal{R}_{th}} - 1), \tag{4.29}$$

$$0 < P_t \leq \mathcal{P}_{\max}. \tag{4.30}$$

Algorithm 4.4 initializes arrays for $\mathcal{Z}_x$ (where x represents different objectives: $\mathcal{Z}_d$ for objective function (P2) or $\mathcal{Z}_q$ for objective function (P3)) and P_t with two feasible values. Initially, P_t remains fixed, while β is computed for the sub-problem (P4) as in (4.23). Then, P_t is determined for (P5) as in (4.27) using the previously obtained β. The optimized values of P_t and β are utilized to solve $\mathcal{Z}_x$. If the current value of $\mathcal{Z}_x$ is lower than the previous value or the iteration reaches its upper limit j', then the iteration halts. Otherwise, the values are saved, and the iteration continues until a lower value is found. This iterative process yields the optimized set $\{\beta, P_t\}$, which is then employed in Algorithm 4.2 or Algorithm 4.3. The Algorithm 4.4 is presented as

Algorithm 4.4 Maximization Algorithm based on AOA

1: **Initialize variables:** $\mathcal{Z}_x^{(1)}$=$\mathcal{Z}_x^{(2)}\forall x \in [d, q]$, $P_t^{(1)}$=$P_t^{(2)}$, j=2, j': Iteration limit.
2: Solve (P4) with given $P_t^{(j)}$ and find $\beta^{(j+1)}$.
3: Solve (P5) with obtained $\beta^{(j+1)}$ from step 2 and find $P_t^{(j+1)}$.
4: Evaluate $\mathcal{Z}_x^{(j+1)}$ with $\beta^{(j+1)}$ and $P_t^{(j+1)}$ obtained from step 2 and 3 respectively.
5: **If** $\mathcal{Z}_x^{(j+1)} \geq \mathcal{Z}_x^{(j)}$ **and** $j \leq j'$, **then** go to step 2 with updated $P_t^{(j+1)}$ and $j = j + 1$.
6: **If** $\mathcal{Z}_x^{(j+1)} < \mathcal{Z}_x^{(j)}$ **or** $j > j'$, **then** loop stops. Go to step 7.
7: **Output:** optimized $\{\beta^{(j-1)}, P_t^{(j-1)}\}$.

It is crucial to initialize $\mathcal{Z}_x$ carefully to ensure that subsequent values meet the condition $\mathcal{Z}_x^{(j+1)} \geq \mathcal{Z}_x^{(j)}$.

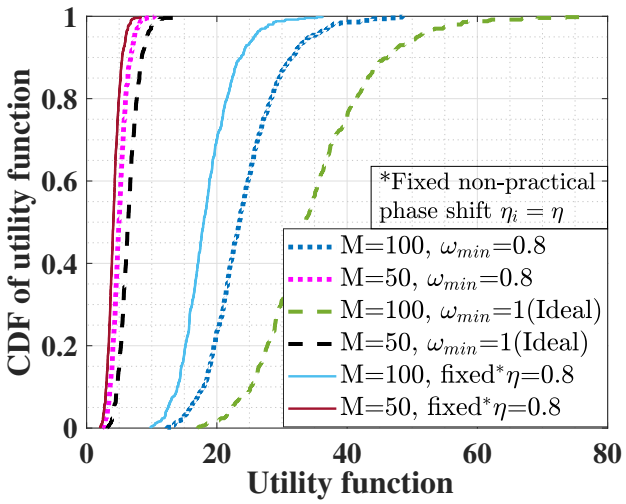


Figure 4.4: CDF plot of UF for number of RIS elements and ideal phase shift condition.

4.4 Results and Discussion

Herein, we assess the effectiveness of the system proposed in this chapter based on the solutions presented. We utilize the ITU-R P.1411-9 site general model for Urban or Sub-urban propagation environment [53] for deriving channels provided in Section 4.2. The algorithmic result(s) are obtained for averaged 500 Monte-Carlo channel realizations. Rayleigh fading is considered for all channels in use. The specific values of other parameters unless stated are d=5m, M=100, N_t=2, $\mathcal{R}_{th}$=10 bits per channel use (bpcu), $\mathcal{P}_{\max}$=5W, ξ_{th}=1μJ, E'=2.8mJ, a=1500, b=0.0022, ϖ=0.43π, ω_{min}=0.8, κ=1.6 [74]. The effective receiver noise level is -70 dBm [2, 79]. The considered central frequency is 0.915 GHz for its favorable EH capabilities. The weights are selected as w_r=0.01 units, w_e=10^6 units and w_p=1 units [31]. The CDF plot in Fig. 4.4 demonstrates a clear correlation, indicating higher UF with increased RIS elements. This observation holds true under ideal conditions of unity phase shift (ω_{min}) as well as under a non-practical scenario where all elements possess the same reflection coefficient amplitude $\{\eta_i\}_{i=1}^{M} = \eta = 0.8$.

In Fig. 4.5, the study compares three solution methodologies: KKT, DT, and QT against a baseline solution and a scenario without RIS involvement ('No RIS' case). Employing

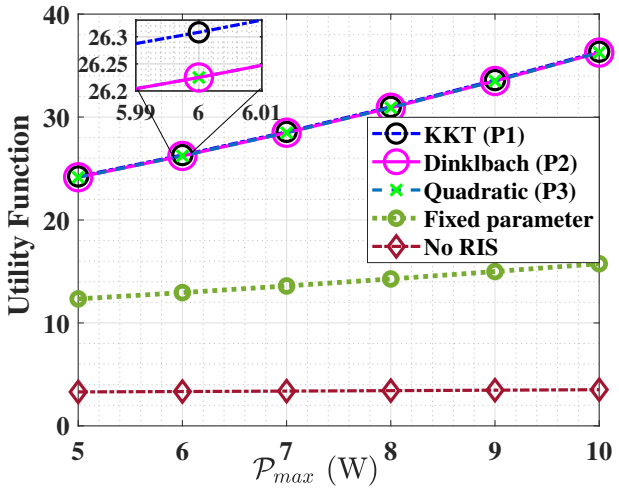


Figure 4.5: Comparative analysis of various solution types for UF vs $\mathcal{P}_{\max}$.

a fixed parameter analysis transforms the multi-variable optimization problem into a single variable one, albeit at the cost of precision for expedited solutions. Adopting DT, with β=0.6 and transforming the problem into one with varying transmit power (P_t). Obtaining closed form solutions via KKT are analytically cumbersome. Hence, DT (being computationally faster than QT), emerges as the preferred Algorithm for further analyses due to its efficacy in addressing the joint optimization problem.

Furthermore, the study explores the joint consideration of rate, EH, and transmit power, revealing that adjusting weights can decompose the problem into individual rate or EH maximization tasks. For rate maximization, weights $\{w_r, w_e, w_p\} := \{1, 0, 1\}$ are utilized, while for EH maximization, weights $\{w_r, w_e, w_p\} := \{0, 1, 1\}$ are applied, thereby maximizing the UF through DT [4]. Fig. 4.6 converts the UF into separate rate (EEIT) and EH (EEET) maximization problems and shows the R-E trade-off i.e., by increasing the EH requirement leads to a reduction in the achievable rate and vice-versa. The results quantify how the achievable rate and harvested energy vary with the corresponding QoS requirements and

[4]By adjusting weights $\{w_r, w_e, w_p\}$:=$\{1, 0, 1\}$ we would rather get normalized rate or EEIT metric as objective. Similarly, with weights $\{w_r, w_e, w_p\}$:=$\{0, 1, 1\}$, we get normalized energy or EEET. Both the metrics can be later converted to extract rate or EH by simply multiplying UF with optimized transmit power as $\mathcal{J}(\beta^*, P_t^*) \times P_t^*$.

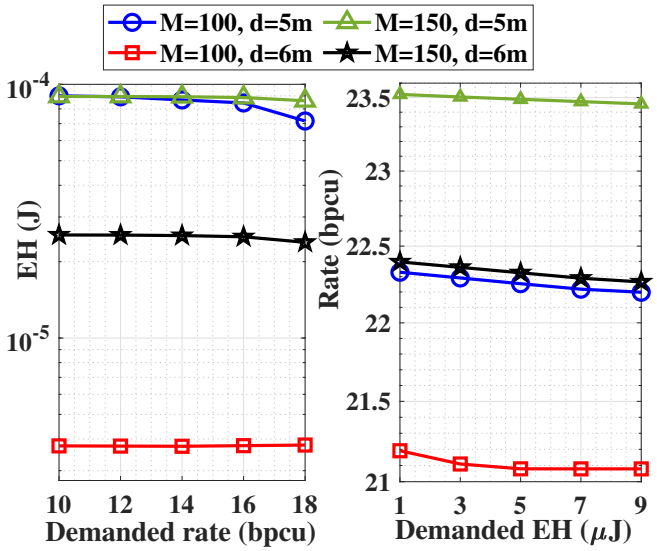


Figure 4.6: R-E trade-off by converting UF to either rate/EH maximization problem for RIS elements and BS-RIS-U separation distance ($d_{br} = d_{ru} = d$).

RIS deployment parameters. Increasing the number of RIS elements from $M = 100$ to $M = 150$ and reducing the BS–RIS–UE separation from $d = 6$ m to $d = 5$ m improve both rate and EH, demonstrating the benefit of RIS dimensioning and favorable deployment geometry. Thus, rather than merely confirming an expected trend, Fig. 4.6 provides useful design insight into how RIS size and placement can be selected according to the desired rate-energy operating point. This characterization is particularly relevant for SWIPT systems in which the network operator must determine an appropriate balance between information delivery and energy transfer. As an improvement, the fixed weights can be taken as variable for further studies.

To ensure a fair comparison, confidence intervals are computed for the results, and corresponding error bars are depicted in Fig. 4.7, illustrating the maximized UF against the number of RIS elements for required rate and BS-RIS-U separation distance. A common 95% confidence level is utilized for this analysis. It becomes evident that the rate threshold ($\mathcal{R}_{th}$) primarily influences the UF at lower RIS element counts. However, with an increase in the number of RIS elements, the impact of higher demands on UF maximization dimin-

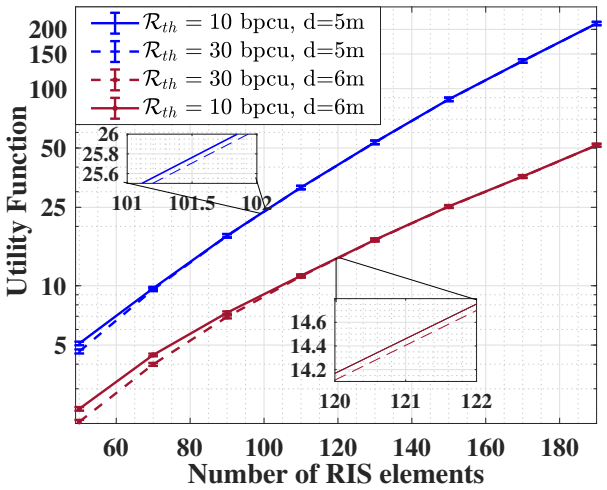


Figure 4.7: UF comparison with number of RIS elements and demanded rate.

ishes indicating the feasibility of meeting elevated demands. In this analysis, the role of EH demands (ξ_{th}) is negligible, thus not incorporated. Moreover, the UF exhibits an increase with reduced BS-RIS-U separation distance ($d_{br} = d_{ru} = d$) for the given parameters.

Fig. 4.8 illustrates the variation of the UF with the number of DPS levels for different transmit power levels. Although the UF is expected to increase with phase resolution, the results reveal an important diminishing-return behavior: a substantial improvement is obtained when the DPS level increases from $L = 2$ to $L = 4$, whereas the gain becomes progressively smaller at higher resolutions and the UF nearly saturates beyond 64-128 (6-7 bits) levels. For example, at $P_{\max} = 5$ W, approximately 5-bit phase resolution ($L = 32$) already provides a UF close to 50, indicating that further increasing the phase resolution may provide limited utility improvement relative to the additional RIS hardware and control complexity. As each resolution bit $L = 2^b$ corresponds to the PIN/varactor diode used at each RIS element for phase control. Consequently, higher RIS elements implies more phase bits and make RIS bulky possessing deployment challenges. Thus, the results help to identify a practically meaningful DPS resolution and avoid unnecessary hardware complexity.

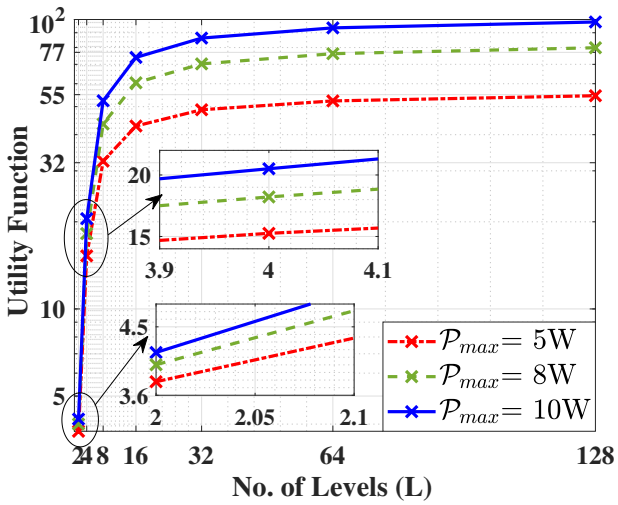


Figure 4.8: UF variations with number of DPS levels for different transmit power levels. Tremendous change in UF is observed from $L = 2$ to $L = 4$ and its saturation after $L = 64$.

The analysis favors DT as the quickest and most efficient method for solving the weighted joint optimization problem. Although QT is slightly slower, it retains the equivalent objective function, offering enhanced readability. However, the KKT closed-form solution outperforms the others but entails intricate analytic computations. By adjusting the weights proposed previously, the defined UF can be repurposed for individual rate or EH maximization problems accordingly. Achieving higher UF necessitates increasing the upper limit of transmit power, augmenting RIS elements, and narrowing the BS-RIS-U separation distance. The practical implementation which rules out CPS at each RIS element and demands for DPS levels, the deciding factor becomes the optimized level (or bits) required to have satisfactory UF.

4.5 Summary

The chapter investigates a practical multi-antenna BS assisted multiple RIS-user paired communication system employing PS-SWIPT with NL-EH model at the UE. Unlike idealized assumptions, the work incorporates a practical phase shift dependent RIS reflection

amplitude model. A unified UF maximization problem, jointly considering the achievable data rate, EH, and transmit power consumption, is formulated under QoS constraints. The optimization is performed with respect to the PS ratio and BS transmit power. To solve the formulated non-convex optimization problem, three different approaches, namely, KKT conditions, Dinkelbach transform, and quadratic transform, are employed and comparatively analyzed. The KKT-based framework provides valuable closed-form insights into the optimal resource allocation structure, while the QT-based method improves interpretability of the fractional objective formulation. Among the considered approaches, DT demonstrates superior convergence characteristics with super-linear and faster convergence behavior, making it the most computationally efficient solution for the proposed system model. Further analysis of the unified UF by decomposing it into individual rate and energy harvesting components validates the classical rate-energy (R-E) trade-off observed in the SWIPT systems. Numerical results reveal that the UF improves significantly with an increase in the number of RIS reflecting elements, higher transmit power budgets, and reduced communication distances. Additionally, the study highlights the importance of the DPS resolution level, as it directly impacts the number of control bits required for configuring practical RIS elements, thereby influencing implementation complexity and signaling overhead. As a future extension, this work can be further enhanced by incorporating joint active and passive beamforming optimization, imperfect channel state information (CSI), channel estimation errors, hardware impairments, and mobility-aware scenarios to evaluate the robustness and applicability of the proposed optimization framework in next-generation wireless networks.

Chapter 5

Active and Passive Beamforming in RIS-assisted SWIPT-IoT system

In this chapter, we consider a smart farming scenario where the Reconfigurable Intelligent Surfaces (RIS) with Simultaneous Wireless Information and Power Transmission (SWIPT) system is extended to support multi-antenna and multiple Internet-of-Thing (IoT) users for enhanced coverage and performance. Temperature and moisture sensors use the power splitting (PS) SWIPT protocol with non-linear energy harvesting (NL-EH) model, while RIS performs passive beamforming with hardware-constrained discrete phase shift (DPS). The goal of this chapter is to minimize transmit power by optimizing transmit beamforming, the RIS phase shift matrix, and the PS factor under Quality-of-Service (QoS) constraints. The developed complex non-convex sub-problems are addressed using two methods: a sub-optimal Zero-Forcing (ZF) approach and an optimal solution based on Semi-Definite Relaxation (SDR) with Gaussian Randomization (GR). An alternate one-dimensional search strategy is used for RIS phase shift optimization. The resulting sub-problems are iteratively solved through an alternating optimization approach. Finally, numerical simulations are conducted to validate the proposed framework in terms of performance and convergence. The results demonstrate robustness under imperfect channel

state information (ICSI) and varying system parameters for the next-generation IoT-enabled smart farming use-case.

The organization of this chapter is as follows. Section 5.1 outlines the introduction of the topic, research gap and key contributions. Section 5.2 describes the system model including signal modeling and channel imperfections. The optimization problem along with the different optimal or sub-optimal solutions are presented in Section 5.3. The comparative analysis based on the simulation results and related observations are discussed in Section 5.4. Finally, the chapter is summarized in Section 5.5.

5.1 Introduction to Joint Active-Passive Beamforming Optimization in RIS-assisted SWIPT-IoT System with DPS

Next generation 6G network are expected to support massive machine type communication (mMTC) by enabling intelligent connectivity among billions of IoT devices. In the same context, smart agriculture ecosystem utilizes an interconnection of sensors responsible for real-time humidity monitoring, soil nutrient balance, weather predictions, and smart irrigation systems. This data-driven agricultural management is essential for increasing farm productivity. Although, the larger farm poses challenges in terms of reliable network connectivity and long-term operation of low-power IoT devices (sensors).

RIS-SWIPT has emerged as a reliable, low-cost, and efficient solution for the imposed challenge of the smart-agricultural systems. RIS provides aid to the non-Line-of-Sight (NLoS) environments commonly found in the rural landscapes by intelligently adjusting the phase shifts of incident signals to focus towards specific IoT node without active power consumption [13, 41]. On the other hand, SWIPT eliminates the dependency on wired

power infrastructure or conventional energy harvesting (EH) means by enabling continuous energy replenishment thorough radio frequency (RF). It allows the simultaneous transmission of data and power over the same RF signal, enabling energy-constrained IoT devices to harvest energy while receiving information.

Early investigations in the RIS-assisted communications mainly concentrated on beamforming and reflection optimization for communication-centric objectives. In particular, the weighted sum-rate maximization and energy efficiency (EE) maximization problems were studied in [80] and [81], respectively, where the optimization variables included active beamforming vectors and RIS reflection matrices. Subsequently, power minimization under QoS constraints was addressed in [18] through the joint optimization of beamforming and reflection coefficients. However, these works neither considered SWIPT operation nor practical EH models.

The integration of SWIPT with RIS-assisted systems has further expanded the research direction. In [43], a linear EH model with PS-SWIPT architecture was investigated for jointly optimizing beamforming vectors, RIS reflection matrices, and PS ratios while considering weighted rate-energy objectives. Similarly, weighted sum-rate optimization for separated EH and information decoding users was explored in [82], whereas [83] focused on the performance analysis under a linear EH model. In [84], a NL-EH model was incorporated for separated users with the objective of transmit power minimization through optimal beamforming design. Weighted sum-power maximization at energy users (EUs) was further analyzed in [85] using joint beamforming and RIS optimization.

Several studies have also investigated rate and EE enhancement in RIS-assisted SWIPT systems. For instance, [86] considered an NL-EH based PS-SWIPT framework and maximized achievable data rate through joint optimization of beamforming vectors, RIS phase shifts, and PS ratios. EE maximization under a linear EH model was addressed

in [87] using a similar optimization framework. Furthermore, ICSI was incorporated in [88, 89, 90, 91, 92, 93], where robust optimization techniques were developed for objectives such as power minimization, max-min EE problem, average harvested energy maximization, and received power enhancement. These works highlighted the importance of robust beamforming and RIS optimization under the Channel State Information (CSI) uncertainty.

More recently, practical RIS hardware considerations have been incorporated through DPS modeling. In [15] and [94], DPS-based RIS systems were investigated for total power minimization, and maximization of the minimum signal-to-interference-plus-noise ratio (SINR) optimization, respectively. However, these studies neither consider SWIPT operation nor the practical EH characteristics. A more comprehensive framework was presented in [55], where an NL-EH enabled PS-SWIPT system with DPS modeling was investigated using weighted fractional programming for optimizing transmit power and PS ratio. Nevertheless, the work did not consider CSI imperfections and joint optimization of beamforming and RIS reflection coefficients.

Although RIS-assisted SWIPT systems have been widely investigated, several research gaps still exist in the literature, as tabulated in Table. 5.1. Early works mainly focused on communication-centric objectives such as the Sum-Rate maximization, EE enhancement, and power minimization without considering the SWIPT operation and practical EH behavior. Later studies incorporated SWIPT architectures; however, most adopted the ideal linear EH models and continuous RIS phase shifts, which are impractical for real hardware implementation. Although a few works considered NL-EH models, wherein the DPS-based RIS operation and imperfect CSI conditions were generally ignored. Moreover, the existing DPS-enabled RIS studies either neglected the SWIPT operation or considered limited optimization variables. Therefore, the joint investigation of practical DPS-based RIS, nonlinear EH modeling, and imperfect CSI remains largely unexplored in the existing literature.

Table 5.1: Recent works on MISO multi-user RIS systems.

Ref.	**EH Model**	**SWIPT system**	**DPS Model**	**ICSI analysis**	**Objective Function**	**Optimizing variable**
[80]	-	X	X	X	Weighted sum rate maximization	Beamforming vector and reflection matrix
[81]	-	X	X	X	Energy efficiency (EE) maximization	Beamforming vector and reflection matrix
[18]	-	X	X	✓	Power minimization	Beamforming vector and reflection matrix
[43]	Linear	PS-SWIPT	X	X	Weighted rate and energy	Beamforming vector, reflection matrix and PS ratio
[82]	Linear	Separated users	X	X	Weighted sum rate	Beamforming vector and reflection matrix
[83]	Linear	PS-SWIPT	X	X	Performance analysis	-
[84]	NL-EH	Separated users	X	X	Power minimization	Optimal beamforming
[85]	Linear	Separated users	X	X	Weighted sum power maximization at ERs	Beamforming vector and reflection matrix
[86]	NL-EH	PS-SWIPT	X	X	Data rate maximization	Beamforming vector, reflection matrix and PS ratio
[87]	Linear	PS-SWIPT	X	X	EE maximization	Beamforming vector, reflection matrix and PS ratio
[88]	Linear	Separated users	X	✓	Power minimization	Beamforming vector and reflection matrix
[89]	Linear	Separated users	X	✓	Max-min EE maximization	Beamforming vector, reflection matrix and PS ratio
[90]	Linear	Separated users	X	✓	Power minimization	Beamforming vector, reflection matrix and sparse code multiple access (SCMA) index
[91]	NL-EH	Separated users	X	✓	Max-min average harvested energy	Precoding vector
[92]	NL-EH	PS-SWIPT	X	✓	Power minimization	Beamforming vector, reflection matrix and PS ratio
[93]	Linear	Separated users	X	✓	Max-min received power for ERs	Beamforming vector and reflection matrix
[15]	-	X	✓	X	Total power minimization	Beamforming vector and reflection matrix
[94]	Linear	Separated users	✓	X	Max-min signal-to-interference-plus-noise ratio (SINR)	Beamforming vector and reflection matrix
[55]	NL-EH	PS-SWIPT	✓	X	Weighted fractional programming	Transmit power and PS ratio
This work	NL-EH	PS-SWIPT	✓	✓	Total transmit power minimization	Beamforming vector, reflection matrix and PS ratio

The present work bridges these research gaps by contributing following points for a comprehensive practical RIS-assisted PS-SWIPT framework for multi-user MISO systems.

- *Practical EH model:* The IoT nodes adopt a PS-SWIPT protocol integrated with a logistic NL-EH model. In contrast to the traditional linear models—such as linear, piecewise, or CLC models—that assume fixed energy conversion behavior, the logistic NL-EH model provides a more realistic representation of the inherently non-linear and dynamic response of RF-EH circuits.

- *DPS Model:* The continuous phase shift (CPS) model for RIS element phase control is impractical to implement due to the limitations of high-resolution hardware. Therefore, a DPS model with a finite number of quantization levels is adopted instead.

- *Algorithmic insights:* The problem is formulated as the minimization of the total transmit power subject to QoS constraints, with tri-optimization variables, viz., active beamforming (transmit precoding) vectors, RIS phase-shift matrix, and PS factor. Due to the non-convex nature of the objective function, we devise suitable algorithms inspired from the ZF, SDR, and GR techniques for optimizing transmit beamforming vectors and PS ratio for all users. Phase shift matrix is optimized by alternate one-dimensional search based Algorithm. Furthermore, an alternate optimization (AO)-based Algorithm is developed to achieve overall total power minimization.

- *Numerical analysis:* A comparison of the developed algorithms is presented with respect to the computational speed and performance. The system's behavior for minimized transmit power is checked for variations in the key parameters, including the number of antennas, RIS element count, number of users, BS-RIS or RIS-users separation distance, quantization levels, target SINR, and EH requirements. Adherence to optimizing RIS phase shifts in order to improve the system performance has also

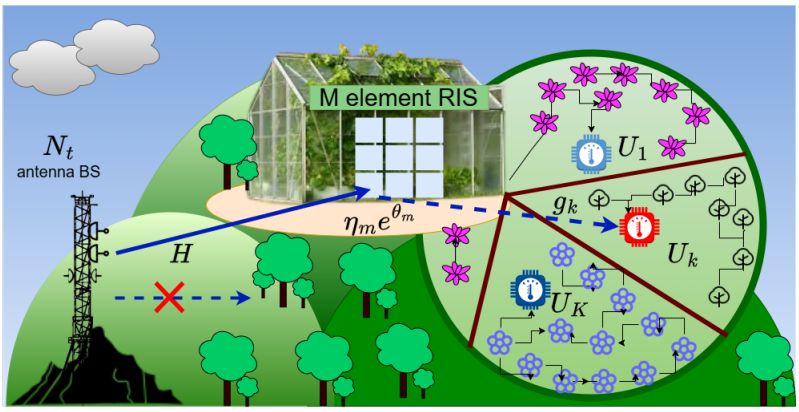


Figure 5.1: System model for RIS assisted PS-SWIPT communication.

been emphasized. Additionally, the perfect CSI assumption has been ruled out with ICSI error analysis showing system's robustness.

5.2 System Model

We consider a downlink MISO smart agriculture system, consisting of K single antenna IoT users $\{U_1, \ldots, U_k, \ldots, U_K\}$ communicating with a base station (BS) with N_t antennas with the aid of M element nearly passive RIS over available single carrier narrowband frequency, as depicted in Fig. 5.1. The RIS is installed on a building, such as greenhouse, from where it is directing signals to the IoT devices or users with SWIPT architecture, thereby collecting information about soil moisture, ambient temperature, soil pH, etc., while additionally harvesting energy in parallel. The communicating channels are assumed to be quasi-static in nature with flat-fading. The baseband (BB) channel from BS to RIS is $\widetilde{\mathbf{H}} \in \mathbb{C}^{M \times N_t}$ and from RIS to k^{th} user is $\widetilde{\mathbf{g}}_k^H \in \mathbb{C}^{1 \times M}$. All channels experience both small-scale Rician fading due to the presence of Line-of-Sight (LoS) and large-scale fading. We assume that BS N_t antennas form half-wavelength and RIS's M-elements form quarter-wavelength uniform linear array (ULA) response vector with $\varrho \in [0, 2\pi]$ as angle of departure or arrival given by

$$\mathbf{o}(M, \varrho) = \left[1, e^{(\frac{j2\pi d}{\lambda}\sin\varrho)}, \ldots, e^{(\frac{j2\pi d(M-1)}{\lambda}\sin\varrho)}\right]. \tag{5.1}$$

The Rician channel having LoS ($\overline{\mathbf{H}}$ / $\overline{\mathbf{g_k}}$) and NLoS ($\widehat{\mathbf{H}}$ / $\widehat{\mathbf{g}_k}$) component between the BS-RIS and RIS-U_k are respectively given by

$$\widetilde{\mathbf{H}} = \sqrt{P_{L_1}}\left(\sqrt{\frac{K_1}{K_1+1}}\overline{\mathbf{H}} + \sqrt{\frac{1}{K_1+1}}\widehat{\mathbf{H}}\right), \tag{5.2}$$

$$\widetilde{\mathbf{g}}_k = \sqrt{P_{L_2}}\left(\sqrt{\frac{K_2}{K_2+1}}\overline{\mathbf{g}_k} + \sqrt{\frac{1}{K_2+1}}\widehat{\mathbf{g}_k}\right), \tag{5.3}$$

where (P_{L_1}) and (P_{L_2}) are the large scale path loss for BS-RIS path and RIS-U_k, respectively. The NLoS parts of the respective channels, $\widehat{\mathbf{H}}$ and $\widehat{\mathbf{g}_k}$ follows $\mathcal{CN}(0,1)$ identical and independently distributed $(\mathrm{i.i.d.})$ distribution. The LoS components for BS-RIS link depends on the beam steering vectors ϱ_{A_1} and ϱ_{D_1} from the ULA response (5.1) represented as

$$\overline{\mathbf{H}} = \mathbf{o}^H(M, \varrho_{A_1})\mathbf{o}(N_t, \varrho_{D_1}). \tag{5.4}$$

Similarly for the RIS-U_k path, the LoS component depends on steering vector ϱ_{D_2} is given by

$$\overline{\mathbf{g}_k} = \mathbf{o}(M, \varrho_{D_1}). \tag{5.5}$$

The perfect channel conditions marked as $\widetilde{\mathbf{H}}$ and $\widetilde{\mathbf{g}}_k$, can be degraded due to environmental conditions and heavy pilot contamination. This induced ICSI is discussed in next section.

5.2.1 Imperfections in Channel

Based on the channel model given for BS-RIS link in (5.2) and RIS-U_k link in (5.3), only the small-scale fading coefficients constituting only NLoS components for both the

links ($\widehat{\mathbf{H}}$ and $\widehat{\mathbf{g}_k})_{\forall k}$ need to be estimated in every transmission phase. Here, Gauss-Markov uncertainty model is utilized to introduces imperfections in these NLoS channels, by replacing $\widehat{\mathbf{H}}$ in (5.2) with $\ddot{\mathbf{H}}$ (5.6) and equivalently replacing $\widehat{\mathbf{g}_k}$ in (5.3) with $\ddot{\mathbf{g}_k}$ (5.7). It is mathematically given by [19]

$$\ddot{\mathbf{H}} = \sqrt{1-\epsilon}\,\widehat{\mathbf{H}} + \sqrt{\epsilon}\,\mathbf{E}_r, \tag{5.6}$$

$$\ddot{\mathbf{g}_k} = \sqrt{1-\epsilon}\,\widehat{\mathbf{g}_k} + \sqrt{\epsilon}\,\mathbf{e}_r, \tag{5.7}$$

where $\mathbf{E}_r$ and $\mathbf{e}_r$ are distributed as $(\mathrm{i.i.d.})$ complex Gaussian random variables with zero mean and unit variance $\mathcal{CN}(0,1)$, representing the error vector. The accuracy of the CSI estimation is given by the error index $\epsilon \in [0,1]$. The unit value of ϵ, implies complete erroneous channel with $\ddot{\mathbf{H}} = \mathbf{E}_r$ and $\ddot{\mathbf{g}_k} = \mathbf{e}_r$, whereas $\epsilon = 0$ represents that CSI estimation process is perfect with our NLoS channel same as in (5.2)-(5.3), i.e., $\ddot{\mathbf{H}} = \widehat{\mathbf{H}}$ and $\ddot{\mathbf{g}_k} = \widehat{\mathbf{g}_k}$. Incorporating channel imperfections, the ICSI channels are marked as $\mathbf{H}$ and $\mathbf{g}_k$. This expression is utilized in the rest of the system analysis.

5.2.2 Signal Model

The RIS phase shift matrix consists of each element's (m^{th}) reflection coefficient amplitude $\eta_m \in [0,1]$ and phase shift $\theta_m \in [0, 2\pi]$, given by $\mathbf{\Theta} = \mathrm{diag}(\eta_1 e^{j\theta_1}, \ldots, \eta_m e^{j\theta_m}, \ldots \eta_M e^{j\theta_M})$. To maximize the signal strength and for simplicity $\{\eta_m\}_{m=1}^{M} = 1$, though it can be individually designed by adding extra implementation cost. For realistic phase implementation θ_m is given by practical DPS model consisting of a set $\mathcal{S}$ containing DPS values (angles) for a particular quantization level $L = 2^b$, where bit b decides the required number of PIN diodes on each RIS element for the phase change. The individual RIS element's phase shift takes discrete value from the set

$\mathcal{S} = \{0, 2\pi/L, \ldots, 2\pi(L-1)/L\}$.

We assume a scenario wherein all the K users are inaccessible to directly communicate with BS. Thus, the cascaded channel BS-RIS-U_k is $\mathbf{f}_k^H = \mathbf{g}_k^H \mathbf{\Theta} \mathbf{H}$. The N_t antenna BS transmits signal $\mathbf{x}$ with linear precoding vector $\mathbf{w}_k \in \mathbb{C}^{N_t \times 1}$ to the desired user U_k, such that $\mathbf{x} = \sum_{k=1}^{K} \mathbf{w}_k s_k$. The transmitted symbol for k^{th} user is s_k, modeled as standard normal distribution having unit power. Thus, the total transmit power from the BS is $P_b = \sum_{k=1}^{K} ||\mathbf{w}_k||^2$. Since we consider the ICSI, the erroneous channel $\mathbf{H}$ and $\mathbf{g}_k$ affects the cascaded channel as well. Considering all the models and assumptions, the signal received from BS to k^{th} user via intelligent reflections from M element RIS is given by

$$y_k = \mathbf{f}_k^H \sum_{j=1}^{K} \mathbf{w}_j s_j + u_k = \mathbf{f}_k^H \mathbf{w}_k s_k + \sum_{j \neq k} \mathbf{f}_k^H \mathbf{w}_j s_j + u_k \tag{5.8}$$

The receiver noise is $u_k \sim \mathcal{CN}(0, \mu_k^2)$ and the RF-BB conversion noise is $v_k \sim \mathcal{CN}(0, \nu_k^2)$, both being characterized as $(\mathrm{i.\,i.\,d.})$ additive white Gaussian noise (AWGN). We consider PS-SWIPT protocol for quenching higher data rate and energy demands, which splits the total received power for ID and EH needs. The received signal for ID with β_k as the PS ratio and related SINR at U_k are respectively expressed as

$$y_k^{ID} = \sqrt{\beta_k} \mathbf{f}_k^H \mathbf{w}_k s_k + \sqrt{\beta_k} \sum_{j \neq k} \mathbf{f}_k^H \mathbf{w}_j s_j + \sqrt{\beta_k} u_k + v_k, \tag{5.9}$$

$$\Gamma_k = \frac{\beta_k |\mathbf{f}_k^H \mathbf{w}_k|^2}{\beta_k \sum_{j \neq k} |\mathbf{f}_k^H \mathbf{w}_j|^2 + \beta_k \mu_k^2 + \nu_k^2}. \tag{5.10}$$

The received signal for EH part with $(1 - \beta_k)$ PS ratio and related sigmoid function based NL-EH at U_k are [53]

$$y_k^{EH} = (\sqrt{1 - \beta_k}) \mathbf{f}_k^H \sum_{j=1}^{K} \mathbf{w}_j s_j + (\sqrt{1 - \beta_k}) u_k, \tag{5.11}$$

$$E_k = \frac{E'}{1-\chi}\left(\frac{1}{1+\exp(-a(1-\beta_k)\sum_{j=1}^{K}|\mathbf{f}_k^H\mathbf{w}_j|^2+ab)}-\chi\right) \tag{5.12}$$

where $\chi = (1+\exp(ab))^{-1}$ and (E', a, b) are the rectenna circuit related constants described in [31]. In the subsequent section, we formulate the primary problem concerning the total power minimization seeking optimized values of important system parameters.

5.3 Problem Formulation and Solution

Herein, the objective is to minimize the total BS transmit power by jointly optimizing the active beamforming vectors $\mathbf{w}_k$, PS ratios β_k, and RIS phase-shift matrix $\mathbf{\Theta}$ for all K users. The optimization is subject to minimum SINR (γ_{th}) and EH (ξ_{th}) constraints to avoid system outage, while additional constraints ensure the feasibility of the PS ratios and DPS-compliant RIS elements. The effects of ICSI are inherently incorporated through the modified channel expressions embedded in the system model and are implicitly reflected in the objective and constraints. The primal optimization problem is mathematically defined as

$$\text{(P1):} \underset{\{\beta_k,\mathbf{w}_k\}_{k=1}^{K},\mathbf{\Theta}}{\text{minimize}} \quad \sum_{k=1}^{K}||\mathbf{w}_k||^2 \tag{5.13}$$

$$\text{subject to :} \quad \text{(C1):}\ \Gamma_k \geq \gamma_{th},\ \forall\, k, \tag{5.14}$$

$$\text{(C2):}\ E_k \geq \xi_{th},\ \forall\, k, \tag{5.15}$$

$$\text{(C3):}\ 0 \leq \beta_k \leq 1,\ \forall\, k, \tag{5.16}$$

$$\text{(C4):}\ \theta_m \in \mathcal{S}, \forall\, m, \tag{5.17}$$

where γ_{th} and ξ_{th} are assumed identical for all K users. Problem (P1) is non-convex due to the coupled optimization variables $\mathbf{w}_k$, β_k, and $\mathbf{\Theta}$ appearing in both the SINR and EH

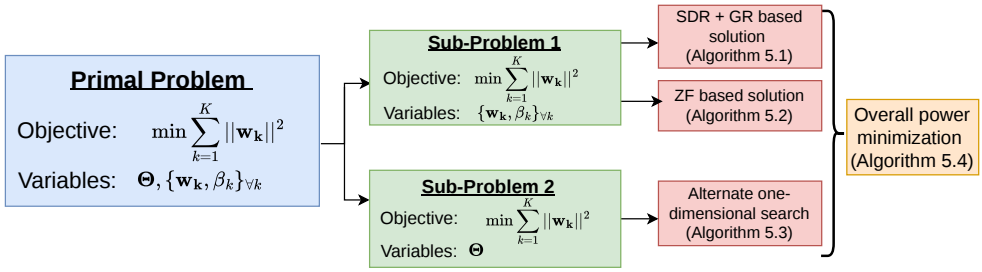


Figure 5.2: Solution frameworks for Problem (P1).

constraints. In particular, $\mathbf{\Theta}$ directly affects the cascaded channel $\mathbf{f}_k^H$ and is therefore implicitly coupled with constraints (C1) and (C2). Moreover, the quadratic objective and DPS constraint further increases the problem's complexity. Consequently, (P1) is classified as a mixed-integer non-linear program (MINLP) and is NP-hard, with no closed-form global optimum.

To address this challenge, a decoupled optimization framework is adopted. As shown in Fig. 5.2, (P1) is decomposed into sub-problems (P2) and (P3). Sub-problem (P2) optimizes $\mathbf{w}_k, \beta_k$ for fixed $\mathbf{\Theta}$ and is solved using either SDR followed by GR (Algorithm 5.1) or ZF (Algorithm 5.2). Sub-problem (P3) optimizes $\mathbf{\Theta}$ for fixed $\mathbf{w}_k, \beta_k$ using alternate one-dimensional search (Algorithm 5.3). The overall solution is obtained via an iterative procedure (Algorithm 5.4), which takes solutions by Algorithm 5.1 and 5.3 or Algorithm 5.2 and 5.3, and iteratively update it. The detailed description is given in the subsequent section.

5.3.1 Joint Optimization of Beamforming Vector and PS Ratio

In this section, the primal problem (P1) is solved for $\{\beta_k, \mathbf{w}_k\}_{\forall k}$ for a fixed value of DPS matrix. The sub-problem (P2) is described as follows.

$$\text{(P2): } \underset{\{\beta_k, \mathbf{w}_k\}_{k=1}^{K}}{\text{minimize}} \quad \sum_{k=1}^{K} ||\mathbf{w}_k||^2 \tag{5.18}$$

$$\text{subject to :} \quad \text{(C1), (C2), (C3).} \tag{5.19}$$

We seek two different types of solution to this sub-problem. The first approch provides an optimal solution by utilizing SDR and GR technique, while the other provides a sub-optimal yet fast converging solution with users and BS antenna limit.

5.3.1.1 Solution via SDR method

We utilize the SDR technique to jointly solve PS factor and transmit beamforming vector. As an initial step, to change the quadratic nature of the objective function in (P2), we introduce a variable $\mathbf{V}_k = \mathbf{w}_k \mathbf{w}_k^H, \forall\, k$, with condition Rank$(\mathbf{V}_k) \leq 1, \forall\, k$. In SDR, we drop the rank-one limitation of the newly introduced variable to avoid non-tractability and therefore (P2) is transformed into a fresh problem with changed variable as

$$\text{(P2)}_\text{a} : \underset{\{\beta_k, \mathbf{V}_k\}_{k=1}^{K}}{\text{min.}} \quad \sum_{k=1}^{K} \text{Tr}(\mathbf{V}_k) \tag{5.20}$$

$$\text{s.t :} \frac{\beta_k \mathbf{f}_k^H \mathbf{V}_k \mathbf{f}_k}{\beta_k \sum_{j \neq k} \mathbf{f}_k^H \mathbf{V}_j \mathbf{f}_k + \beta_k \mu_k^2 + \nu_k^2} \geq \gamma_{th}, \forall k, \tag{5.21}$$

$$\frac{E'}{1-\chi} \left(\frac{1}{1+e^{(-a(1-\beta_k)\sum_{j=1}^{K} \mathbf{f}_k^H \mathbf{V}_j \mathbf{f}_k + ab)}} - \chi \right) \geq \xi_{th}, \forall k, \tag{5.22}$$

$$0 \leq \beta_k \leq 1, \forall\, k, \tag{5.23}$$

$$\mathbf{V}_k \succeq 0, \forall\, k. \tag{5.24}$$

The modified problem (5.20) is still non-convex due to coupled optimizing variables in (5.21) and (5.22). We need to separate them out in order to make (5.20) a convex optimizing problem. Thus, variables in constraints are rearranged as follows

$$(\text{P2})_{\text{a}} : \min_{\{\beta_k, \mathbf{V}_k\}_{k=1}^{K}} \sum_{k=1}^{K} \text{Tr}(\mathbf{V}_k) \tag{5.25}$$

$$\text{s.t. } : \frac{\mathbf{f}_k^H \mathbf{V}_k \mathbf{f}_k}{\gamma_{th}} - \sum_{j \neq k} \mathbf{f}_k^H \mathbf{V}_j \mathbf{f}_k \geq \mu_k^2 + \frac{\nu_k^2}{\beta_k}, \forall k, \tag{5.26}$$

$$\sum_{j=1}^{K} \mathbf{f}_k^H \mathbf{V}_j \mathbf{f}_k \geq \frac{A}{1-\beta_k}, \forall k, \tag{5.27}$$

$$0 \leq \beta_k \leq 1, \forall\, k, \tag{5.28}$$

$$\mathbf{V}_k \succeq 0, \forall\, k. \tag{5.29}$$

where $A = b - \frac{1}{a} \ln \left(\frac{(1-\chi)(E'-\xi_{th})}{\xi_{th}(1-\chi)+\chi E'} \right)$. Problem $(\text{P2})_{\text{a}}$ is converted into a convex problem which can be numerically evaluated by the convex programming tool CVX utilizing SDP methods [20]. The optimized solution $\mathbf{V}_k^*$ is guaranteed only iff it remains a unit rank matrix. In this regard, we utilize GR techniques to convert multi-ranked $\mathbf{V}_k^*$ (if obtained) into unit rank with added computational complexities. As a compensation to the occurred loses, we consider a vector $\mathbf{u}_k$ in the direction of $\mathbf{w}_k$, defined as $\mathbf{u}_k = \frac{\mathbf{w}_k}{||\mathbf{w}_k||}$ for power refinement. It should be noted that we have already obtained the optimized β_k^* by solving Problem $(\text{P2})_{\text{a}}$, thus it does not create any hindrance while extracting a rank-1 solution. Thus, we reformulate the Problem $(\text{P2})_{\text{a}}$ into $(\text{P2})_{\hat{a}}$ with changed variable $\mathcal{P}_k$ as the power allocation to the k^{th} user

with $\mathbf{u}_k$ as its direction, i.e., $\mathbf{w}_k = \sqrt{\mathcal{P}_k}\mathbf{u}_k$, mathematically given as

$$(\text{P2})_{\hat{a}} : \min_{\{\mathcal{P}_k\}_{k=1}^K} \sum_{k=1}^{K} \mathcal{P}_k \tag{5.30}$$

$$\text{s.t. } : \frac{\mathcal{P}_k|\mathbf{f}_k\mathbf{u}_k|^2}{\gamma_{th}} - \sum_{j\neq k} \mathcal{P}_j|\mathbf{f}_k\mathbf{u}_j|^2 \geq \mu_k^2 + \frac{\nu_k^2}{\beta_k}, \forall k, \tag{5.31}$$

$$\sum_{j=1}^{K} \mathcal{P}_j|\mathbf{f}_k\mathbf{u}_j|^2 \geq \frac{A}{1-\beta_k}, \forall k, \tag{5.32}$$

$$\mathcal{P}_k \geq 0, \, \forall \, k. \tag{5.33}$$

The optimized solution $\mathcal{P}_k^*$ can be solved by applying CVX optimization solver to Problem $(\text{P2})_{\hat{a}}$. The complete process involving SDR, GR, and power refinement is summarized in Algorithm 5.1.

Algorithm 5.1 SDR and GR based Algorithm

1: **Input:** Channel parameters $(\mathbf{\Theta}, \mathbf{H}, \mathbf{g}_k^H)_{\forall k}$, randomization counts R;
2: **Initialize:** Find cascaded channel $\mathbf{f}_k = \mathbf{g_k^H \Theta H}$;
3: **Solution:** Find $\{\beta_k, \mathbf{V}_k\} \, \forall \, k$ to solve SDR problem (5.25) by CVX and following steps for GR;
4: **while** $r \leq R$ **do**
5: **Step 1:** Generate $\mathbf{w}_k^{(r)} \sim \mathcal{CN}(0, \mathbf{V}_k) \, \forall \, k$ with covariance matrix $\mathbf{V}_k$ obtained by CVX solution;
6: **Step 2:** Define $\mathbf{u}_k^{(r)} = \frac{\mathbf{w}_k^{(r)}}{||\mathbf{w}_k^{(r)}||}$ and solve (5.30) for $\mathcal{P}_k$ by CVX solver for all k.
7: **Step 3:** Save valid total power $P_b^{(r)} \leftarrow \sum_{k=1}^{K} \mathcal{P}_k$;
8: **Step 4:** $r = r + 1$, go to step 1;
9: **end while**
10: **Output:** $P_b \leftarrow \min_{r\in\mathcal{R}} P_b^{(r)}$, $\mathcal{R} = \{r|\text{validated candidates}\}$, $\mathbf{w}_k^* \leftarrow \arg\min_{r\in\mathcal{R}} P_b^{(r)}$, $\beta_k^* \leftarrow \beta_k$.

As an initial step, we find the cascaded channel $\mathbf{f}_k$. The Problem in (5.25) can now be solved by CVX convex optimizer to give preliminary solution $\{\beta_k, \mathbf{V}_k\}_{\forall k}$. Here, we get optimized β_k^*, but the Rank$(\mathbf{V}_k) > 1$ (in general), and thus we apply the GR technique to extract the rank-one matrix $(\mathbf{V}_k^*)$ and find corresponding beam forming vector $(\mathbf{w}_k^*)$. Inline with the GR process for a given randomization count r, we generate a Gaussian random

vector with zero mean and covariance $\mathbf{V}_k$. Subsequently, we apply a power refinement by solving (5.30) with CVX solver, and find the corresponding total power $P_b^{(r)} = \sum_{k=1}^{K} \mathcal{P}_k$ for all the validated candidate beamformers $\mathbf{w}_k^{(r)} \, \forall \, k$. Finding the least $P_b^{(r)}, \forall \, r \in \mathcal{R}$, yields the minimized total power and corresponding $\mathbf{w}_k^{(r)}$ as optimal beamforming vector $\mathbf{w}_k^*$.

By implementing the GR process, it is ensured that Rank$(\mathbf{V}_k) = 1$. Thus, the optimized solution to (5.25) is in fact the solution to the sub-problem (P2). Being a convex SDP, the SDR converges deterministically to the global optimum of the relaxed problem, such that relaxed optimal solution provides a tight lower bound on the true non-convex objective. The convergence of the GR stage is probabilistic, the better-found solution monotonically improves and tends to the best solution achievable by the randomization method, though not necessarily being the global optimum. Thus, the SDR ensures deterministic convergence to the relaxed bound, while the GR ensures stochastic convergence toward a near-optimal feasible solution.

The CVX utilizes the interior point Algorithm which increases the computation complexity, making the overall complexity of Algorithm 5.1 as $\mathcal{O}(KM^2N_t + \sqrt{KN_t}(K^3N_t^2 + K^2N_t^3) + RKN_t^2)$. More the randomization counts (R), the better is the solution however, with an increased execution time. Thus, we seek a solution which can provide satisfactory optimal solution (sub-optimal), but with a faster speed.

5.3.1.2 ZF based Closed form Solution

For the scenarios where the number of antennas are more than or equal to the number of users (i.e., $N_t \geq K$), we utilize the ZF precoder design for optimizing beamforming vector. It impressively cancels the interference term where multiple users are in vicinity, i.e., $\mathbf{f}_j^H \mathbf{w}_k = 0, \, \forall j \neq k$, and simplifies the SINR and EH term. With applied ZF approach to solve $\{\beta_k, \mathbf{w}_k\}_{\forall k}$ for a given RIS phase shift matrix $\mathbf{\Theta}$, sub-problem (P2) is mathematically

modified as follows

$$(\text{P2})_{\text{b}}: \min_{\{\beta_k, \mathbf{w}_k\}_{k=1}^{K}} \quad \sum_{k=1}^{K} ||\mathbf{w}_k||^2 \tag{5.34}$$

$$\text{s.t.} : \frac{\beta_k |\mathbf{f}_k^H \mathbf{w}_k|^2}{\beta_k \mu_k^2 + \nu_k^2} \geq \gamma_{th}, \, \forall \, k, \tag{5.35}$$

$$\frac{E'}{1-\chi}\left(\frac{1}{1+e^{(-a(1-\beta_k)|\mathbf{f}_k^H \mathbf{w}_k|^2 + ab)}} - \chi\right) \geq \xi_{th}, \, \forall \, k, \tag{5.36}$$

$$0 \leq \beta_k \leq 1, \, \forall \, k, \tag{5.37}$$

$$\mathbf{F}_k^H \mathbf{w}_k = \mathbf{0}, \, \forall \, k. \tag{5.38}$$

where $\mathbf{F}_k = [\mathbf{f}_1, \ldots, \mathbf{f}_{k-1}, \mathbf{f}_{k+1}, \ldots, \mathbf{f}_K] \in \mathbb{C}^{N_t \times (K-1)}$ represents all the interfering user channels being nullified by (5.38).

Theorem 1: Problem $(\text{P2})_{\text{b}}$ can be decomposed into K sub-problems of power minimization for all individual k user and then solving by applying ZF beamforming. The obtained closed form solutions are given as

$$\beta_k^* = 0.5\Big(- z_1 + \sqrt{z_1^2 + 4z_2}\Big), \, \forall \, k, \tag{5.39}$$

$$\mathbf{w}_k^* = \mathbf{Z}(\mathbf{Z}^H \mathbf{Z})^{-1} \mathbf{z}_4 = \mathbf{Z}^{\dagger} \mathbf{z}_4, \, \forall \, k. \tag{5.40}$$

Proof. It is noted that while seeking a solution via ZF, in the transformed problem $(\text{P2})_{\text{b}}$, both the SINR and EH constraints, i.e., (5.35) and (5.36), respectively, can be decoupled across each user k, along with the objective function itself. As a result, $(\text{P2})_{\text{b}}$ can be disintegrated into K independent sub-problems, where the k-th sub-problem is formulated as follows

$$(\text{P2})_{\text{c}}: \min_{\{\beta_k, \mathbf{w}_k\}} \quad ||\mathbf{w}_k||^2 \tag{5.41}$$

$$\text{s.t.} : \frac{\beta_k |\mathbf{f}_k^H \mathbf{w}_k|^2}{\beta_k \mu_k^2 + \nu_k^2} \geq \gamma_{th}, \tag{5.42}$$

$$\frac{E'}{1-\chi}\left(\frac{1}{1+\exp\left(-a(1-\beta_k)|\mathbf{f}_k^H \mathbf{w}_k|^2 + ab\right)} - \chi\right) \geq \xi_{th}, \tag{5.43}$$

$$0 \leq \beta_k \leq 1, \quad \mathbf{F}_k^H \mathbf{w}_k = \mathbf{0}. \tag{5.44}$$

The optimized solution β_k^* can be obtained if constraints related to the SINR (5.42) and NL-EH (5.43) of problem $(P2)_c$ must be tightly bounded and hold with the equality, represented as

$$\frac{\beta_k|\mathbf{f}_k^H\mathbf{w}_k|^2}{\beta_k\mu_k^2+\nu_k^2}=\gamma_{th} \implies |\mathbf{f}_k^H\mathbf{w}_k|^2=\frac{\gamma_{th}(\beta_k\mu_k^2+\nu_k^2)}{\beta_k} \tag{5.45}$$

$$\frac{E'}{1-\chi}\left(\frac{1}{1+\exp\left(-a(1-\beta_k)|\mathbf{f}_k^H\mathbf{w}_k|^2+ab\right)}-\chi\right)=\xi_{th},$$

$$\implies |\mathbf{f}_k^H\mathbf{w}_k|^2=\frac{b-\frac{1}{a}\ln\left(\frac{(1-\chi)(E'-\xi_{th})}{\xi_{th}(1-\chi)+\chi E'}\right)}{1-\beta_k}=\frac{A}{1-\beta_k} \tag{5.46}$$

Solving (5.45) and (5.46), we get

$$\frac{\gamma_{th}(\beta_k\mu_k^2+\nu_k^2)}{\beta_k}=\frac{A}{1-\beta_k} \implies \beta_k^2-\beta_k\Big(\frac{\nu_k^2}{\mu_k^2}+\frac{A}{\gamma_{th}\mu_k^2}-1\Big)-\frac{\nu_k^2}{\mu_k^2}=0$$

$$\implies \beta_k^*=0.5\Big(-z_1+\sqrt{z_1^2+4z_2}\Big). \tag{5.47}$$

Here $z_1=\frac{\nu_k^2}{\mu_k^2}+\frac{A}{\gamma_{th}\mu_k^2}-1$, $z_2=\frac{\nu_k^2}{\mu_k^2}$. The optimized value (5.47) essentially satisfies the constraint (5.44). Utilizing β_k^* in (5.45), we now find the optimal beamforming vector by modifying problem $(P2)_c$ for single variable $\mathbf{w}_k$, given by

$$(P2)_d: \min_{\mathbf{w}_k} \quad \mathbf{w}_k^H\mathbf{w}_k \tag{5.48}$$

$$\text{s.t.}: \mathbf{f}_k^H\mathbf{w}_k=z_3, \tag{5.49}$$

$$\mathbf{F}_k^H\mathbf{w}_k=\mathbf{0}. \tag{5.50}$$

where $z_3=\sqrt{\frac{\gamma_{th}}{\beta_k^*}(\beta_k^*\mu_k^2+\nu_k^2)}$. Constraints in (5.42) and (5.43) are combined together with equality to find optimized β_k^*, this take form of constraint (5.49) in Problem $(P2)_d$. It can be solved by taking λ_1 and λ_2 as Lagrangian multipliers, mathematically represented as

$$\mathcal{L}(\mathbf{w}_k,\lambda_1,\lambda_2)=\mathbf{w}_k^H\mathbf{w}_k+\lambda_1(\mathbf{f}_k^H\mathbf{w}_k-z_3)+\lambda_2(\mathbf{F}_k^H\mathbf{w}_k-\mathbf{0}_{1\times(K-1)}). \tag{5.51}$$

Algorithm 5.2 ZF based Algorithm

1: **Input:** Channel parameters $(\mathbf{H}, \mathbf{g}_k^H, \mathbf{\Theta})_{\forall k}$, γ_{th}, ξ_{th}, μ_k^2, ν_k^2, $\forall\, k$;
2: **Initialize:** Find cascaded channel $\mathbf{f}_k = \mathbf{g_k^H \Theta H}$ and interfering users channels $\mathbf{F_k} = [\mathbf{f_1}, \ldots, \mathbf{f_{k-1}}, \mathbf{f_{k+1}}, \ldots, \mathbf{f_K}],\ \forall\, k$;
3: **Solve:** $\beta_k^* = 0.5\Big(- z_1 + \sqrt{z_1^2 + 4z_2}\Big),\ \forall\, k$ by (5.39);
4: Find pseudoinverse $\mathbf{Z}^\dagger$ and solve $\mathbf{w}_k^* = \mathbf{Z}^\dagger \mathbf{z}_4,\ \forall\, k$ by (5.40);
5: **Output:** $P_b = \sum_{k=1}^{K} ||\mathbf{w}_k||^2\ , \{\beta_k^*, \mathbf{w}_k^*\}\, \forall\, k$.

The optimized beamforming hence obtained is written as

$$\mathbf{w}_k^* = \mathbf{Z}(\mathbf{Z}^H\mathbf{Z})^{-1}\mathbf{z}_4. \tag{5.52}$$

where $\mathbf{Z} = [\mathbf{f}_k^H\ \ \mathbf{F}_k^H]$ and $\mathbf{z}_4 = [z_3\ \ \mathbf{0}_{1\times(K-1)}]^T$. Henceforth, the obtained values of $\{\beta_k^*, \mathbf{w}_k^*\}$ are used in (5.40) and (5.39), respectively. □

The optimized transmit beamforming vector $\mathbf{w}_k^*$ for all K users are summed up to get total transmit power. The optimizing steps are summarized in Algorithm 5.2. Since both the transmit beamforming and PS ratio are obtained in closed-form expressions, the convergence is guaranteed. The worst-case complexity of Algorithm 5.2 is $\mathcal{O}(KM^2N_t + K^3N_t + K^4)$. For higher N_t and fewer K, complexity becomes $\mathcal{O}(KM^2N_t + K^3N_t)$. It is observed that the computation time is significantly less than applying Algorithm 5.2, though the solution obtained is sub-optimal. The convergence, execution speed, and performance comparison will be highlighted in Section 5.4.

5.3.2 Phase Shift Optimization

From the previous section, we obtain the optimized values of the PS factor and transmit beamformer either by applying Algorithm 5.1 or 5.2, depending on the user's preference for optimality or speed. In this section, we seek an alternate solution for another sub-problem (P3) to optimize the DPS matrix (passive RIS beamformer $\mathbf{\Theta}$). The objective of

total minimized power is now a function of $\mathbf{\Theta}$, mathematically given by

$$\text{(P3): } \min_{\mathbf{\Theta}} \quad P_b(\mathbf{\Theta}) = \sum_{k=1}^{K} ||\mathbf{w}_k(\mathbf{\Theta})||^2 \tag{5.53}$$

$$\text{s.t. : } \quad \text{(C1), (C2), (C4).} \tag{5.54}$$

From (C4), it is evident that the phase shift of each m RIS element should adhere to the DPS set $\mathcal{S}$ values. The direct solution to problem (P3) is not possible due to the discretized nature of the constraint (C4), thereby leading to the intractability. Thus, we need to devise an Algorithm which iteratively selects the best phase shift to each RIS element, to provide an overall lowest transmit power. For all the RIS elements, we start with the allocation of random values to $\mathbf{\Phi} = [\theta_1, \ldots, \theta_M]$ (variable containing RIS's M element phase angles) for a given L from set $\mathcal{S}$. Now, we take the RIS elements one-by-one and assign the best phase shift value from $\mathcal{S}$, i.e., by taking m^{th} individual element of RIS and fixing other $(M-1)$ element phases, we search through set $\mathcal{S}$ which minimizes the overall transmit power in iterative manner, such that

$$\theta_m^* = \arg \min_{\theta_m \in \mathcal{S}} P_b(\Phi). \tag{5.55}$$

The one-dimensional search continues until we encounter a higher $P_b(\Phi)$ value. The detailed procedure is given in Algorithm 5.3.

In Step 2 and Step 6 with the fixed value of $\mathbf{\Phi}$ and $\mathbf{\Phi}_{temp}$, respectively, we plug Algorithm 5.1 or 5.2 to obtain optimized $\{\beta_{k,1}, \mathbf{w}_{k,1}\}$ and $\{\beta_{k,2}, \mathbf{w}_{k,2}\}$, respectively. The computation complexity for Algorithm 5.3 is $\mathcal{O}(ML(C_{solver} + KN_t))$, where C_{solver} is the computation time required by Algorithm 5.1 or 5.2.

Algorithm 5.3 Phase Optimization Algorithm

Input: L, M;
Initialize: Random selection of $\mathbf{\Phi} = [\theta_1, \ldots, \theta_m, \ldots, \theta_M]$ where phase $\theta_m \in \mathcal{S}$;
Set of quantized levels $\mathcal{S}$=$\{s_1, \ldots, s_l, \ldots, s_L\}$,$m$=1, l=1.
Solution: Taking each element m at a time and iteratively assign optimized phase value from $\mathcal{S}$.
while $m \leq M$ **do**
    Step 1: $\theta_{best} = \theta_m$;
    Step 2: Compute $\{\beta_{k,1}, \mathbf{w}_{k,1}\} \forall\, k$ using Algorithm 5.1 or 5.2 with $\mathbf{\Phi}$;
    Step 3: Find $P_{best} \leftarrow \sum_{k=1}^{K} ||\mathbf{w}_{k,1}||^2$; ▷ Taking each quantized phase value from $\mathcal{S}$
    while $l \leq L$ **do**
        Step 4: $\theta_{test} = s_l$;
        Step 5: Replace $\theta_m \leftarrow \theta_{test}$ and update $\mathbf{\Phi}$ as $\mathbf{\Phi}_{temp}$;
        Step 6: With $\mathbf{\Phi}_{temp}$ find $\{\beta_{k,2}, \mathbf{w}_{k,2}\} \forall k$ using Algorithm 5.1 or 5.2 and find P_{temp};
        if $P_{temp} < P_{best}$ **then**
            Step 7: Update $P_{best} \leftarrow P_{temp}$;
            Step 8: Update $\theta_{best} \leftarrow \theta_{test}$;
        end if
        Step 9: $l = l + 1$;
    end while
    Step 10: Update $\mathbf{\Phi}$, $\theta_m^* \leftarrow \theta_{best}$ and $m = m + 1$;
end while
Output: $\mathbf{\Phi}^* = [\theta_1^*, \ldots, \theta_m^*, \ldots, \theta_M^*]$ and $\mathbf{\Theta}^* = \text{diag}(\eta_1 e^{j\theta_1^*}, \ldots, \eta_M e^{j\theta_M^*})$

Algorithm 5.4 Overall total power minimization Algorithm

Input: $i = 1$, τ, $i_{\max}$, L, $P_b^{(0)}$;
Initialize: Cascaded channel $\mathbf{f}_k$;
Solution: Iteratively optimizing sub-problems (P2) and (P3).
while $i \leq i_{\max}$ **do**
    Step 1: Calculate $\mathbf{\Theta}_{opt}^{(i)}$ using Algorithm 5.3;
    Step 2: Calculate $\{\beta_{k,opt}^{(i)}, \mathbf{w}_{k,opt}^{(i)}\} \forall\, k$ using Algorithm 5.1 or 5.2 with input $\mathbf{\Theta}_{opt}^{(i)}$ from step 1;
    Step 3: Calculate $P_b^{(i)} \leftarrow \sum_{k=1}^{K} ||\mathbf{w}_{k,opt}^{(i)}||^2$;
    if $|P_b^{(i)} - P_b^{(i-1)}| < \tau$ **then**
        break;
    else
        Step 4: Update $P_b^{(i-1)} \leftarrow P_b^{(i)}$, $i = i + 1$
    end if
end while
Output: $\mathbf{\Theta}^* \leftarrow \mathbf{\Theta}_{opt}^{(i)}, \beta_k^* \leftarrow \beta_{k,opt}^{(i)}, \mathbf{w}_k^* \leftarrow \mathbf{w}_{k,opt}^{(i)} \forall\, k$

5.3.3 Overall Transmit Power Minimization

Herein, we design an Algorithm to calculate the total minimized power consumption by the BS. This involves the algorithms developed in Section 5.3.1 for optimized values of beamforming vector and PS ratio, and related Algorithm in Section 5.3.2 for optimized phase values. An AO based Algorithm is proposed for the same, which is summarized in Algorithm 5.4. Fig. 5.3 provides a clearer visualization of each Algorithm and its corresponding steps. It highlights the sequential flow of computations, decision-making loops, and optimization updates involved in the proposed framework. This representation helps in understanding the interaction between sub-algorithms and the iterative nature of the overall optimization process.

We start with initializing the values of channel vector, tolerance τ, iteration limit $i_{\max}$ and a feasible total power for the sake of comparison for the rest of the iterations. We then iteratively calculate $\mathbf{\Theta}_{opt}$ and $\{\beta_{k,opt}\,, \mathbf{w}_{k,opt}\}_{\forall k}$ using Algorithm 5.3 and Algorithm 5.1 or 5.2 respectively, unless we reach the tolerance τ or $i_{\max}$.

The computation complexity is $\mathcal{O}(I(C_{solver} + C_{phase}))$, where I is the number of iterations required by Algorithm 5.4 to converge, C_{phase} is the computation time taken by Algorithm 5.3 for phase optimization. To validate the Algorithm 5.4, we present convergence plot in Fig. 5.4, which compares Algorithm 5.1 (GR based solution) and Algorithm 5.2 (ZF based solution) utilized in Step 2. The minimized power is least when employing GR than ZF, as it gives guaranteed optimal solution. Next, we move our focus to the execution time complexity analysis, It is evident that ZF has lesser complexity than GR based Algorithm 5.2. A detailed analysis will be presented in the subsequent section along with varying system parameters.

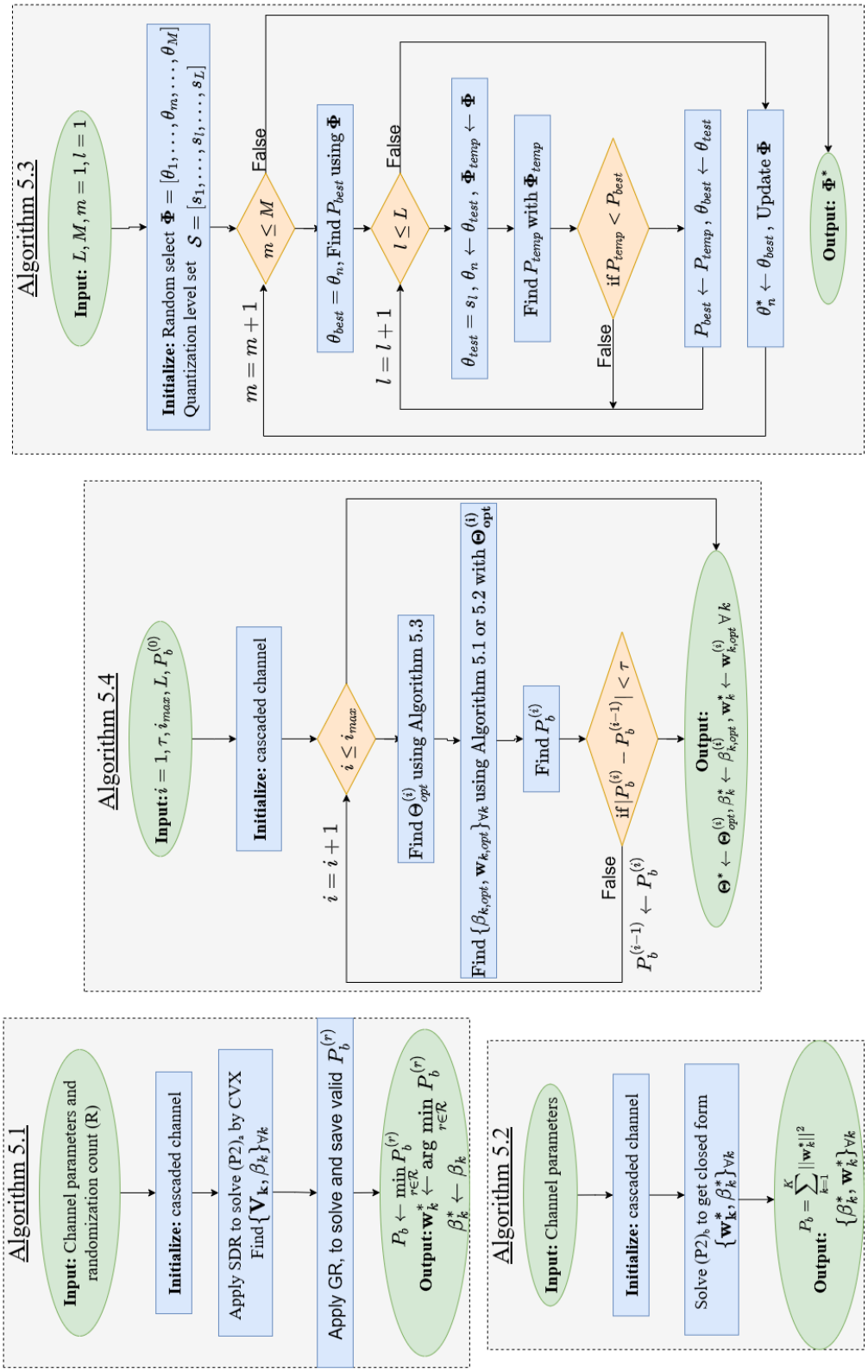


Figure 5.3: Flow chart summarizing the Algorithms: 5.1, 5.2, 5.3 and 5.4.

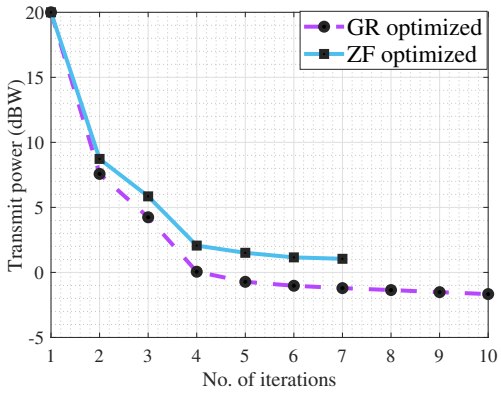


Figure 5.4: Convergence plot for the validation of various Algorithms.

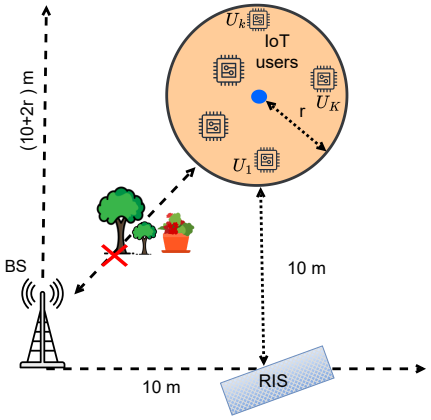


Figure 5.5: Simulation setup for BS, RIS and users placement.

5.4 Simulation Results

We provide the numerical results herein to validate the proposed algorithms and show the impact of various system parameters on the essential system outputs. The placement of BS, users and RIS are given by simulation setup in Fig. 5.5. To emulate a medium-scale farm cell, the BS is at origin (0,0), RIS is at (10 m, 0) coordinates and the K IoT users are randomly distributed within the circle with center (10 m, $10 + r$ m) and radius $r = 5$ meters [84]. The NL-EH circuit model values are E'=2.8 mJ, a=1500, b=0.0022, obtained after curve-fitting for $f = 0.915$ GHz [55]. It is experimentally proven that at 0.915 GHz frequency, more energy can be harvested and is suitable for the ISM band typ-

Table 5.2: Simulation parameters

Parameters	**Values**
Number of IoT users (K)	3 [1]
Number of BS antennas (N_t)	4 [1]
Number of RIS elements (M)	50 or 100 [55, 95]
Number of DPS levels (L)	2 [94]
Rician factor $(K_1 = K_2)$	10 dB [94]
BS-RIS distance (d_{BR})	10 meters [84]
K User space radial distance (r)	5 meters [84]
RIS-U_k distance (d_{RU_k})	$\mathcal{U}[10, 20]$ meters [84]
Frequency (f)	0.915 GHz [55]
Desired SINR (γ_{th})	30 dBm [94]
Desired EH (ξ_{th})	1 μJ [94]
U_k receiver noise power (μ_k^2)	-50 dBm [1]
U_k receiver conversion noise (ν_k^2)	-70 dBm [1]
Error index (ϵ)	0 or 0.9

ically used by IoT standards like low-range (LoRa) and narrowband IoT (NB-IoT). This ensures its practical compatibility with existing agricultural deployments. The Rician factor $(K_1 = K_2 = 10 \text{ dB})$ models a strong LoS component characteristic of open-field rural environments [94]. The desired SINR ($\gamma_{th} = 30$ dBm) and EH thresholds ($\xi_{th} = 1$ μJ) are chosen to represent typical QoS and energy demands for distributed IoT sensor nodes. The receiver and conversion noise powers (-50 dBm and -70 dBm, respectively) are aligned with the practical SWIPT receiver specifications reported in [1]. The number of BS antennas ($N_t = 4$) and RIS elements ($M = 50$ and 100) represents moderate and dense surface configurations. The DPS level ($L = 2$) corresponding 1-bit quantization implies reduced hardware cost and complexity. The typical simulation parameters with their corresponding values are summarized in Table. 5.2, unless specified otherwise.

The large scale path loss for BS-RIS path (P_{L_1}) and RIS-U_k path (P_{L_2}) are given by ITU-R P.1411-9 site general model for Urban or Sub-Urban propagation environment [62] and the values of constants are taken from [53]. We initially analyze the simplified single

user system and present the system analysis. Subsequently, we assess the MU system in further evaluation.

5.4.1 Single User System

This is a special case of the generalized system model as shown in Fig. 5.1, wherein we consider only a single U_1 available over a given time-frequency dimension. Thus, there is no interference term present in (5.10) and it changes for $K = 1$ as

$$\Gamma = \frac{\beta|\mathbf{f^H w}|^2}{\beta\mu^2 + \nu^2}. \tag{5.56}$$

Instead of solving the primal problem (P1) for all values of K, we are now only solving it for the case where $K = 1$. While solving the corresponding sub-problem (P2) for optimized beam forming vector and PS ratio, we need not utilize the computationally heavy ZF or SDR techniques. This can rather be solved by well-known technique of maximum ratio transmission (MRT), which provides direct solution for beamforming vector and PS ratio as

$$\beta^* = 0.5\Big(- z_1' + \sqrt{{z_1'}^2 + 4z_2'}\Big), \tag{5.57}$$

$$\mathbf{w}^* = z_3' \frac{\mathbf{f}^H}{||\mathbf{f}||^2}. \tag{5.58}$$

Here, $z_1' = \frac{\nu^2}{\mu^2} + \frac{A}{\gamma_{th}\mu^2} - 1$, $z_2' = \frac{\nu^2}{\mu^2}$, $z_3' = \sqrt{\frac{\gamma_{th}}{\beta^*}(\beta^*\mu^2 + \nu^2)}$. For optimized values of phase shift matrix, we utilize Algorithm 5.3, with a little change in Step 2 and Step 6, where we seek optimized values of $\{\beta_{k,1}, \mathbf{w}_{k,1}\}$ and $\{\beta_{k,2}, \mathbf{w}_{k,2}\}$, respectively, by (5.57) and (5.58) for $K = 1$.

Fig. 5.6 shows the effectiveness of utilizing optimized phase shift Algorithm 5.3 for single user system with beamforming vector solved by MRT along with ICSI. Here, with the quantized levels $L = 2$, the optimized phase yields similar results while applying im-

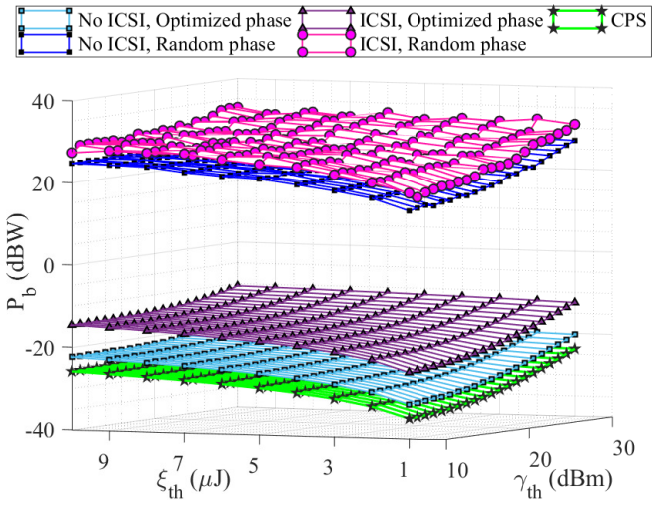


Figure 5.6: Comparison of optimized phase with random phase and CPS for single user employing MRT based beamformer. The ICSI with error index $\epsilon = 0.9$ shows increased power required for both random and optimized phase, when compared with the 'No ICSI' case.

practical CPS, though randomly distributed phase requires higher power. Also, minimized power increases with increase in rate and SNR thresholds. The presence of imperfect CSI, represented by an error index of (ϵ = 0.9), results in higher power consumption for both the random and optimized schemes, while comparing with perfect CSI condition (ϵ = 0) termed as 'No ICSI'. Next, we present the analysis for MU system.

5.4.2 Multiple User system

We now illustrate the effectiveness of a MU system by varying various system parameters like antenna number, RIS elements count, number of users, separation distance, quantized levels, desired SINR, and EH.

5.4.2.1 Algorithmic Comparison

In Section 5.3, we introduced three distinct algorithms to tackle the primal problem (P1), each with its own strategic approach to optimization. Building upon these, a unified framework (Algorithm 5.4) is developed to achieve comprehensive power minimization across the

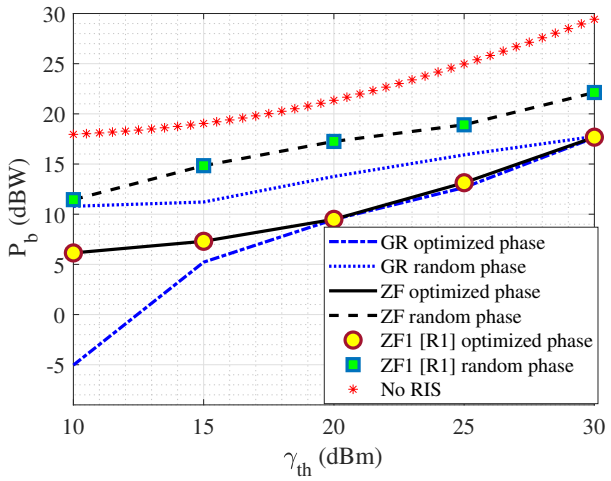


Figure 5.7: Comparative analysis of various Algorithmic solution for $M = 20$. Herein, [R1] corresponds to [1].

Table 5.3: Comparative solution types

Solution name	β_k **and** $\mathbf{w}_k$ **optimization**	**Phase optimization**
GR opt.	Algorithm 5.1	Algorithm 5.3
GR random	Algorithm 5.1	Random phase
ZF opt.	Algorithm 5.2	Algorithm 5.3
ZF random	Algorithm 5.2	Random phase
ZF1 opt.	[1] (Table II)	Algorithm 5.3
ZF1 random	[1] (Table II)	Random phase

system. The challenge lies in identifying which of these algorithms provides the best balance between maximizing system performance and minimizing execution time. To address this issue, a detailed comparison is presented in Fig. 5.7, wherein we illustrate the minimized transmit power required to satisfy a given SINR threshold (γ_{th}) by different solution methods adopted, as outlined in Table 5.3. The performance evaluation considers seven distinct solution types, which are described as follows: *(1) GR Optimized Phase*, which employs the finalized Algorithm 5.4 combined with Algorithm 5.1 (SDR and GR-based beamforming) and utilizes the optimized phase shift design obtained through Algorithm 5.3; *(2) GR Random Phase*, which uses the same beamforming setup as in the GR-optimized case but

replaces the optimized phase shifts with randomly assigned ones; *(3) ZF Optimized Phase*, which integrates Algorithm 5.4 with Algorithm 5.2 (ZF-based beamforming) along with the optimized phase shift matrix from Algorithm 5.3; *(4) ZF Random Phase*, similar in beamforming structure to ZF-optimized but uses a random phase shift matrix instead of the optimized one; *(5) ZF1 Optimized Phase*, where Algorithm 5.4 is used in conjunction with the solution framework provided in [1] (Table II), adapted to our system, and the phase shifts are optimized using Algorithm 5.3; *(6) ZF1 Random Phase*, which retains the same beamforming structure as ZF1-optimized but employs randomly generated phase shifts; and finally, *(7) No RIS*, which serves as a baseline scenario, modeled as a simple reflection off a concrete wall, as described in [53], without any RIS-assisted transmission. The ZF based optimized beamforming solutions by the Algorithm 5.1 and *ZF1* [1] (Table II), are overlapping, while there is improved transmit power for GR (Algorithm 5.2). We obtain similar transmit power for higher values of desired SINR, when solved via any type of solution for optimized phase shift. While employing the phase shift optimization we are able to get better performance for all solutions types (i.e., GR, ZF and ZF1), rather than keeping it randomly allocated.

Fig. 5.8 compares the execution time of first six solution type, viz., (1) ZF random phase, (2) ZF optimized phase, (3) ZF1 random phase, (4) ZF1 optimized phase, (5) GR optimized phase, and (6) GR random phase. The *'Ref.'* is the reference parameters as mentioned in Table 5.2 with $M = 20$. Later we increase antenna numbers $(N_t = 10)$, users $(K = 10)$, Quantized levels $(L = 8)$ and RIS elements to $M = 50$, which surely increases the execution time. Ofcourse, applying optimized phase Algorithm would take more time with respect to random phase allocation. It is noteworthy that *GR opt.*'s actual execution time is divided by 40, for the clarity of plot and giving clear distinction with other optimizing techniques, e.g., at a given *'Ref.'* bar plot, the actual execution time is 29.6 sec which is indicated

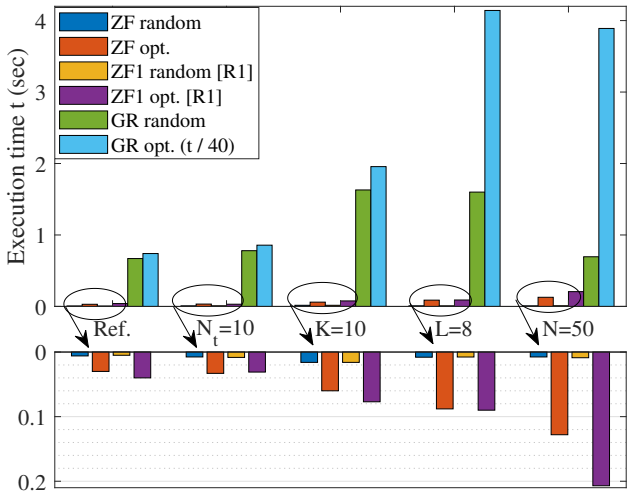


Figure 5.8: Execution time comparison for various algorithmic solutions of the primal problem.

as $\frac{29.6}{40} = 0.74$ sec. The execution time is considered here as a measure of computational complexity and is not, by itself, an indicator of improved system performance. In particular, the optimized solutions require additional computational effort to obtain the corresponding improvement in P_b, thereby introducing a performance-complexity trade-off. ZF1 solution with random phase nearly takes similar execution time as that of ZF solution. Among all, ZF with randomized phase gives result very fast, followed by ZF with optimized phase, then GR with random phase and optimized phase sequentially. For the reference case, the execution time for ZF and ZF1 has an absolute increase in execution time of only 24 ms and 35 ms, respectively when adopting optimized phase. In contrast, the GR-based optimization incurs a substantially higher computational burden. Hence, ZF provides a computationally efficient alternative when its resulting reduction in P_b is adequate. This does not imply that ZF is universally superior to GR; rather, it indicates that ZF can provide a favorable performance-complexity trade-off for the considered scenario. The performance-complexity trade-off can be improved by using a lower-complexity initialization, such as a ZF-based solution, and by reducing or adaptively selecting the randomization counts (R) in the GR procedure

Table 5.4: Comparative analysis of computational complexity

Sol. type	**Complexity**	**Exe. time**
GR opt.	$\mathcal{O}(I(C_{GR}+MLC_{GR}+MLKN_t))$	104 sec
GR random	$\mathcal{O}(I(C_{GR}))$	0.67 sec
ZF opt.	$\mathcal{O}(I(C_{ZF}+MLC_{ZF}+MLKN_t))$	0.03 sec
ZF random	$\mathcal{O}(I(C_{ZF}))$	0.006 sec
$C_{GR} = KM^2N_t + \sqrt{KN_t}(K^3N_t^2 + K^2N_t^3) + RKN_t^2$ $C_{ZF} = KM^2N_t + K^3N_t + K^4$		

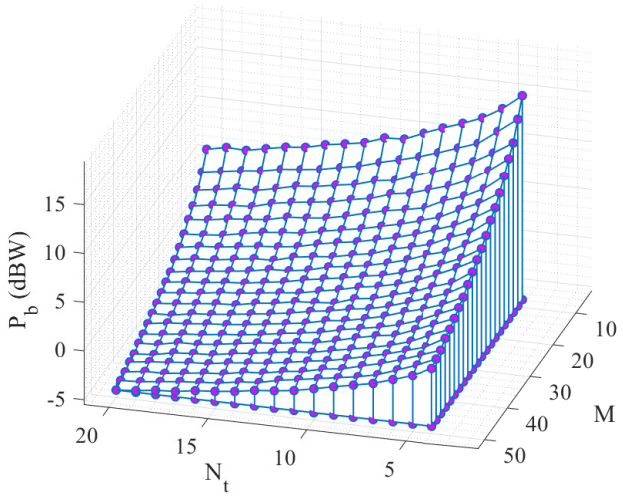


Figure 5.9: Combined impact of RIS elements and BS antenna count on transmit power.

(Algorithm 5.1) based on solution improvement or convergence.

From both the plots Fig. 5.7 and Fig. 5.8, ZF with optimized phase provides similar minimized transmit power at 30 dBm as GR optimized phase, with 987 times faster speed (from *Ref.* plot). Table. 5.4 contrasts the computation complexity in polynomial time along with the execution time with the reference parameters termed as *'Ref.'*. Thus, for the rest of the analysis we intend to utilize the optimized ZF and random phase algorithms to sketch the variations and impact of various important system parameters.

5.4.2.2 Number of RIS Elements and Antenna Count

Fig. 5.9 represents the minimized power with increasing RIS element number (M) as well as with higher total BS antenna count (N_t). Considering $N_t = 20$ and $M = 50$, the transmit power goes down to -4.7 dBW, a 127 times decrement as compared to $(N_t = 4, M = 10)$ provides 16.24 dBW power. This highlights the considerable advantages of deploying large-scale or even massive antenna arrays in MISO-SWIPT systems. With a higher number of antennas at the base station, the system can form highly directional beams that efficiently reduces the required transmit power at the base station, making the overall system more energy-efficient and practical for real-world deployment.

5.4.2.3 Impact of Optimized Phase and Quantized Phase Level

Fig. 5.10, presents the clear appreciation in the transmit power for higher desired SINR and EH demands at user. Likewise in Fig. 5.6 and Fig. 5.7, the optimized phase shift matrix (employing Algorithm 5.3 in Algorithm 5.4) reduces the required transmit power, while comparing it with the random allocation of phases. This comparative decrement is approximately 19 times that for $\xi_{th} = 1\,\mu J$, and $\gamma_{th} = 10$ dBm. As a reference, we compare random and optimized phase shift matrix with the quantized phase error model and MM based phase model, described in detail as follows.

5.4.2.3.1 Quantization Error with Projection Model (QEPM)

The authors in [2] discussed the phase error due to quantization in the DPS model and approximating it using projection method. We apply the same method to our system model for providing a contrasting view. First we consider that m^{th} RIS element phase $\theta_m \in [-\pi, \pi)$ and perfect optimized phase shift (CPS) are given for m^{th} RIS element considering k^{th} user is $\theta_{m,opt} = \arg([\mathbf{g}_k^H]_m[\mathbf{H}]_m)$. The same can be applied for all the K users. For a b-bit RIS, each element's discrete phase set is defined as $\mathcal{F} = \{-\pi, -\pi + \frac{2\pi}{2^b}, \ldots, \pi - \frac{2\pi}{2^b}\}$. The quan-

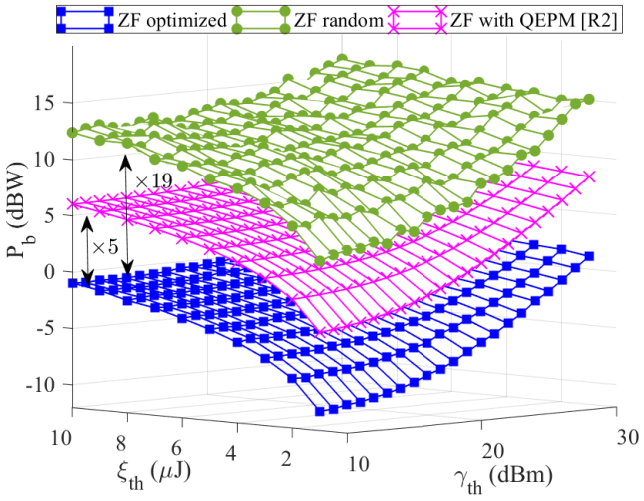


Figure 5.10: Minimized transmit power solved by ZF, varying with desired SINR and EH. The performance gains for random, optimized and QEPM [R2] (i.e., [2]) phase shift matrix are marked.

tized phase error $\theta_{m,err}$ is obtained by projecting the optimal continuous phase $\theta_{m,opt}$ onto $\mathcal{F}$ as $\theta_{m,err} = \Pi_{\mathcal{F}}(\theta_{m,opt}) - \theta_{m,opt}$, where $\Pi_{\mathcal{F}}(\cdot)$ denotes the nearest discrete phase point in $\mathcal{F}$. The corresponding projection is expressed as

$$\Pi_{\mathcal{F}}(\theta_m^{opt}) = \begin{cases} \dfrac{(m-1)\pi}{2^{b-1}} - \pi, & \text{if } \theta_m^{opt} < \dfrac{(2m-1)\pi}{2(2^{b-1})} - \pi, \\ \dfrac{m\pi}{2^{b-1}} - \pi, & \text{otherwise,} \end{cases} \tag{5.59}$$

where $m = \left\lfloor \dfrac{2^{b-1}(\theta_{m,opt} + \pi) + \pi}{\pi} \right\rfloor$. This operation minimizes the distance between the continuous and discrete phases, ensuring each RIS element adopts the nearest quantized phase level. The complete proof is given in Appendix A of [2]. Now, we utilize this erroneous phase shift matrix $\Delta\boldsymbol{\Theta} = \text{diag}(\eta_1 e^{j\theta_{1,err}}, \ldots, \eta_m e^{j\theta_{m,err}}, \ldots \eta_M e^{j\Delta\theta_{M,err}})$ in Step 1 of Algorithm 5.4, and solve Step 2 with ZF (Algorithm 5.2), to obtain the plot *ZF with QEPM* in Fig. 5.10. Following the comparison, there is a 5 times performance gain with the proposed Algorithm (indicated in the plot).

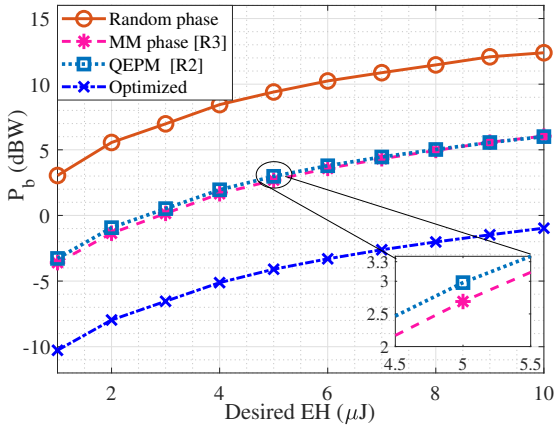


Figure 5.11: Optimized phase by Algorithm 5.3 is compared with random phase, QEPM [R2] (i.e., [2]) and MM phase model [R3] (i.e., [3]), for minimized power varying with demanded EH.

5.4.2.3.2 MM based Phase Model

As another reference to optimize the RIS phase-shift vector $\mathbf{u} = [e^{j\theta_1}, \ldots, e^{j\theta_M}]$, for given optimized beamforming vector and PS ratio $\{\mathbf{w}_k, \beta_k\}_{\forall k}$, we utilize the MM framework described in [3, 96]. The cascaded channel $\mathbf{f}_k^H = \mathbf{g}_k^H \boldsymbol{\Theta} \mathbf{H}$ is modified as defining $\mathbf{b}_{k,j} = \text{diag}(\mathbf{g}_k^H)\mathbf{H}\mathbf{w}_j$ and $\mathbf{B}_{k,j} = \mathbf{b}_{k,j}\mathbf{b}_{k,j}^H$. The SINR (C1) and EH (C2) constraints are modified as

$$\mathbf{u}^H \mathbf{R}_k^S \mathbf{u} \geq c_k^S; \quad \mathbf{u}^H \mathbf{R}_k^E \mathbf{u} \geq c_k^E, \tag{5.60}$$

where $\mathbf{R}_k^S = \beta_k \Big(\mathbf{B}_{k,k} - \gamma_{th} \sum_{j \neq k} \mathbf{B}_{k,j} \Big)$, $c_k^S = \gamma_{\text{th}} \big(\beta_k \mu_k^2 + \nu_k^2 \big)$, $\mathbf{R}_k^E = (1 - \beta_k) \sum_{j=1}^K \mathbf{B}_{k,j}$ and $c_k^E = A$.

Let $\mathbf{R}_\ell = [\mathbf{R}_k^S \ \mathbf{R}_k^E]$ and $c_\ell = [c_k^S \ c_k^E]$ with $\ell = 1, \ldots, 2K$ denote all the SINR and EH constraints. In the MM step, the quadratic term is majorized by its first-order surrogate at iteration t is

$$\mathbf{u}^H \mathbf{R}_\ell \mathbf{u} \leq 2\Re \Big\{ \mathbf{u}^H \mathbf{d}_\ell^{(t)} \Big\} + \text{const}, \tag{5.61}$$

This transforms the feasibility update into maximizing a linear function of $\mathbf{u}$. Aggregating all the violated constraints with weights $w_\ell^{(t)} = \max\big(0, \ c_\ell - \mathbf{u}^{(t)H} \mathbf{R}_\ell \mathbf{u}^{(t)}\big)$, the MM

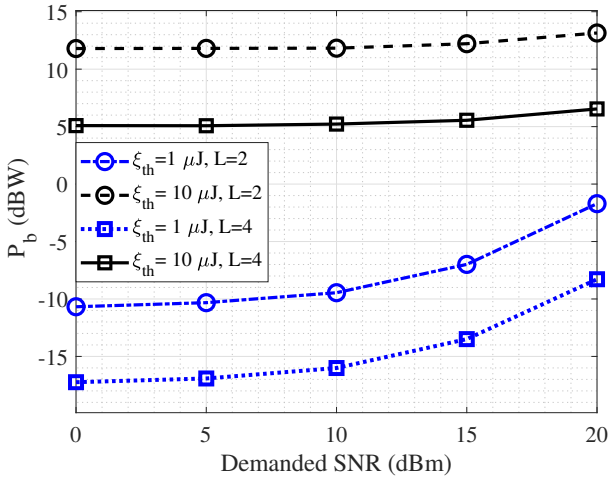


Figure 5.12: Minimized transmit power varying with desired SINR and EH for different quantized phase levels with $M = 100$.

direction becomes

$$\mathbf{q}^{(t)} = \sum_{\ell=1}^{2K} w_{\ell}^{(t)} \mathbf{R}_{\ell} \mathbf{u}^{(t)}. \tag{5.62}$$

The optimal unit-modulus update is then obtained in closed form as $u_n^{(t+1)} = e^{j \arg(q_n^{(t)})}$, followed by a discrete projection for the adopted DPS model. This MM-based procedure ensures a monotonic reduction of constraint violations and yields an efficient RIS phase design without matrix convex programming solvers.

Fig. 5.11 compares MM based phase model with the three described techniques, namely, random phase, QEPM, and proposed optimized solution given by Algorithm 5.3, for minimized power with demanded EH (ξ_{th}). This demonstrates the effectiveness of the proposed Algorithm. Between the MM-based optimized phase-shift matrix and the QEPM model, the former exhibits superior performance, achieving nearly a 25% improvement. This additionally highlights the importance of employing the optimization algorithms in the system to make it robust.

Similarly Fig. 5.12 highlights the same trend between ξ_{th} and γ_{th} as observed in Fig. 5.10, however with varying quantized phased shift level ($L = 2 \text{ or } 4$). As we increase

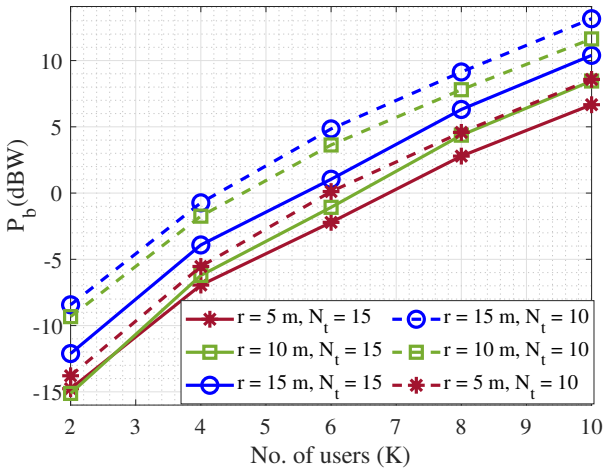


Figure 5.13: Impact of increasing the users on transmit BS power with growing user's radial distance (r) and BS antenna count with $M = 100$.

the quantized phase shift levels, the sample space of $\mathcal{S}$ increases, and therefore the phase shift error reduces. Correspondingly, the optimized phase shift Algorithm can provide better optimized values which makes cascaded channels grow stronger. As a result, there is impactful reduction in the transmit power of around 70% from $L = 2$ to $L = 4$, at $\xi_{th} = 1\,\mu J$, $\gamma_{th} = 20\,\text{dBm}$. Although, increasing the number of levels does not only reduces transmit power, but also increases the overhead bits on the RIS elements for phase tuning. Thus, we need to find a solution which balances the device's bulkiness and acceptable transmit power as per the requirements.

5.4.2.4 Variation in the Number of Users

Fig. 5.13 depicts the variation of the minimized transmit power as a function of the number of users for different user radial distances (r), which indirectly reflects the increase in the RIS–U_k separation. As observed, the minimized total transmit power exhibits a monotonic increase with the number of users, owing to the additional spatial degrees of freedom required to satisfy the QoS constraints of each user. Furthermore, a larger radial distance r results in a higher minimized power due to the increased path loss between the RIS and

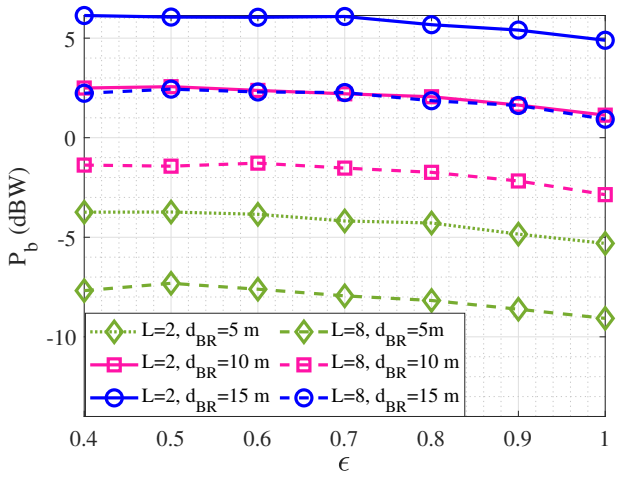


Figure 5.14: Impact of channel state error on minimized power with quantized level and BS-RIS distance.

the users. Notably, increasing the number of BS antennas from $N_t = 10$ to $N_t = 15$ leads to a substantial reduction in the transmit power to 88% for $r = 15$ m, whereas the reduction of 55% for $r = 5$ m. This behavior indicates that the impact of increasing N_t is more pronounced in the scenarios with larger propagation distances and higher user densities. In particular, the variation in minimized transmit power is significantly greater for higher user counts (e.g., $K = 10$ compared to $K = 2$) and for larger radial distances (e.g., $r = 15$ m compared to $r = 5$ m).

5.4.2.5 Impact of CSI Error

Following our previous analysis, where we considered the perfect CSI available globally, we now rule out the assumption of perfect CSI and bring out the imperfections in all the related channels to observe its impact on our system's objective function. Fig. 5.14 represents the impact of error term ϵ on the minimized transmit power for quantized level and BS-RIS separation distance. As a proof for the theoretical explanation, with ϵ moving close to unity, the transmit power reduces. For the plot $L = 2, d = 5$ m, the reduction in P_b is 44% by increasing ϵ from 0.4 to 1. It also highlights that growing quantized levels L and

reduced separation distance can further degrade the P_b. It is inline with the quantized phase shift analysis provided in Fig. 5.12 and inference for separation distance given in Fig. 5.13.

We have carried out several analyses for our system under consideration by varying different system variables to check for its impact on the objective function. For a reduced BS transmit power, we aim at more RIS elements, higher BS antennas and quantized phase shift levels while the desired SINR, EH requirements, and separation distance (BS-RIS or RIS-U_k) should be downsized with the error index tending closer to unity. In terms of algorithmic performance and speed, we have compared seven types of solutions; namely: ZF random and quantized phase, GR based random and quantized phase, ZF1 (as given in [1]) random and quantized phase, and no RIS condition. The number of available users and BS antenna count, along with execution time is a sweet-sour type of condition for ZF based Algorithm. Utilization of the GR is a suitable solution for such conditions while sacrificing the execution time. In addition, there is a tremendous saving in the transmit power when utilizing optimized phase Algorithm than its randomized allocation.

5.5 Summary

This chapter investigated an RIS-assisted MISO PS-SWIPT framework designed to supporting multiple users (IoT-enabled devices), giving power optimized practical solution for considered smart farming use-case. To capture real-world deployment characteristics, the system incorporates RIS DPS model along with logistic NL-EH model at SWIPT-IoT side. To satisfy strict QoS demands while maintaining a reliable communication, a joint optimization framework involving the BS beamforming vectors (active beamforming), RIS phase shift configurations (passive beamforming), and PS ratios was developed. Owing to the coupled variables and non-convex nature of the problem, efficient solution strategies based on on ZF, SDR, and GR techniques were proposed, together with an alternate

one-dimensional search approach for RIS phase optimization. These methods were jointly implemented within an AO Algorithm. The numerical results demonstrated that the proposed framework effectively minimizes the transmit power while preserving robust system performance under ICSI and diversified network conditions including RIS element number, user densities, discrete levels of DPS, and SINR targets. The obtained results validate the suitability of RIS-assisted SWIPT systems for energy-efficient IoT communications in the next-generation smart agriculture networks. Future research will investigate intelligent learning-driven optimization methods capable of offering faster convergence and improved adaptability compared to conventional convex optimization methods. Specifically, reinforcement learning (RL) approaches such as Deep Deterministic Policy Gradient (DDPG), Proximal Policy Optimization (PPO), and Deep Q-Network (DQN) will be explored to enable near real-time control of beamforming and RIS configuration in dynamically changing wireless environments. Such AI-enabled methods are expected to reduce computational complexity and convergence latency while maintaining near-optimal energy and spectral efficiency. Additional extensions may include full-duplex operation, and integration with other 6G technologies like non-orthogonal multiple access (NOMA) and integrated sending and communication (ISAC) with RIS.

Chapter 6

STAR-RIS assisted SWIPT-IoT System

The conventional reflection-only Reconfigurable Intelligent Surface (RIS) limited coverage is extended from 180° to 360° by Simultaneously Transmitting and Reflecting-RIS (STAR-RIS). When integrated with the Simultaneous Wireless Information and Power Transmission (SWIPT) Internet-of-Things (IoT) systems, performance is significantly enhanced by dynamically directing energy and information signals to distinct IoT nodes, energy receiver (ER) and information receiver (IR), with Energy Splitting (ES) and Mode Switching (MS) mode of operation, enabling precise control over the energy distribution between the transmission and reflection zones, accommodating various types of user demands. For the considered practical system with discrete phase shift (DPS) model and non-linear Energy Harvesting (EH) model, we aim to maximize the weighted Rate-Energy (WRE) function, i.e., data rate of IR and EH of ER, with certain Quality-of-Service (QoS) constraints by optimizing power parameters. The proposed Alternate Optimization (AO) algorithm is used to solve the complicated WRE maximization problem. The numerical results emphasize on the energy split ratio for ES and element division for MS that greatly impacts the performance. The choice of DPS level (quantization bits) relies on the balance of device bulkiness (phase control bits) and system performance.

The organization of this chapter is as follows. Section 6.1 presents the introduction, identifies the research gap and summarizes the major contributions. Section 6.2 details the system model for separate ES and MS operational modes. The formulated optimization problem along with the proposed algorithmic solutions are presented in Section 6.3. Section 6.4 provides the simulation results together with the comparative analysis and key observations. Finally, the chapter is concluded in Section 6.5.

6.1 Maximizing Weighted Function in STAR-RIS aided SWIPT-IoT with Discrete Phase Shifting

The "Bharat 6G Vision" Mission of India, envisions the availability of internet connectivity to 6 Lakh villages with emphasis on smart farming having use cases of Uncrewed-Aerial-Vehicle (UAV) for pesticide application, advanced storage systems, intelligent transportation solutions, and farm-to-plate tracking [97]. The extended battery life for Internet-of-Things (IoT) devices deployed on-field for soil and weather vitals, monitoring is essential for self-sustainable systems.

The Reconfigurable Intelligent Surfaces (RIS) has myriad advantages of spectral, energy, and cost efficiency, but its operation is limited by providing directivity to reflection side only [53]. The coverage can be further extended to full-space smart radio environment by modified version of RIS named as Simultaneously Transmitting and Reflecting-RIS (STAR-RIS), which can accommodate users not only on the reflecting side but also in the transmission zone too. Structure wise, STAR-RIS consists of tiny metamaterials called elements, that supports magnetic current on a transparent substrate, looking like "ice cubes in a glass of water" [17]. These elements intelligently direct the incident signal, partly to the reflection and transmission side depending on the adopted protocol. There are three oper-

Table 6.1: Comparison of existing literature on STAR-RIS assisted SWIPT systems.

Ref.	**STAR-RIS Protocol**	**SWIPT**	**EH Model**	**Phase Shift Model**	**Optimization Objective**
[99]	-	No	–	CPS	Near and far field channel modeling
[100]	ES, MS	No	–	CPS	Outage probability analysis
[101]	ES	Yes	Linear	CPS	Rate and power outage analysis
[102]	ES	Yes	Linear	CPS	Rate maximization
[103]	ES	Yes	Linear	CPS	EE and sum-rate maximization
[104]	ES	Yes	Linear	CPS	Weighted sum power maximization
[105]	ES/MS	Yes	Linear	CPS	RSMA-based performance enhancement
[106, 107]	ES/MS	No	–	DPS	Phase quantization analysis
Present Work	ES, MS	Yes	Non-linear	DPS	Weighted rate-energy maximization

ational protocols reported in the literature, namely Energy Splitting (ES), Mode Switching (MS), and Time Switching (TS). Each has its own pros and cons, like ES and TS are complex to implement but have great flexibility, while MS is quite easy to operate but provides marginal gains [98].

STAR-RIS are asserted to be economical and environment friendly, when employed with the Simultaneous Wireless Information and Power Transmission (SWIPT) systems providing prudent solution to the longer battery life of the IoT devices [66]. In this case, information receiver (IR) and energy receiver (ER) are served simultaneously, which are present across the reflection and transmission zones of STAR-RIS. The recent works on STAR-RIS are highlighted in Table 6.1. Authors in [99, 100], considers the performance analysis in terms of outage probability comparing the ES and MS protocols. The authors employing the STAR-RIS for SWIPT systems utilize the linear EH model, as also reported in majority of the works in this context [101, 102, 103, 104]. The linear EH model considers constant energy efficiency (EE), which lacks in replicating the non-linear behaviors of the diodes used in the EH circuit. The rate and power outage analysis for IR and ER

users respectively, with ES is given in [101]. While only the rate maximization is considered in [102]. The multiple-objective EE and sum rate maximization problem is considered by Authors in [103]. The weighted sum power maximization is taken as objective by Authors in [104]. Integrating advanced technology of Rate Splitting Multiple Access (RSMA) communication with the aid of STAR-RIS considering spatial correlation is examined by Authors in [105]. The above works consider STAR-RIS phase shift to be perfectly designed with no errors. The concept of practical discrete phase shift (DPS) model for the STAR-RIS element's phase is incorporated by Authors in [106, 107], but without considering SWIPT communication.

The main contributions of this chapter addresses the gap in above mentioned literature are summarized as follows.

1. Practical sigmoid function based non-linear EH (NL-EH) model is used at ER, which captures all the non-linearity of the rectenna (rectifier + antenna) circuit.

2. The continuous phase shift (CPS) model for STAR-RIS element's phase shift is unfeasible to realize the high resolution hardware configuration. Thus, the DPS model is incorporated with finite quantization levels.

3. For a holistic examination of the system, a weighted rate-energy (WRE) function is maximized for optimized power parameters, which benefits both the ER and IR users. The proposed algorithm based on AO is utilized for possible solution pursuing a divide-and-conquer approach.

4. ES and MS transmission protocols are compared for various cases involving energy split ratio, element division, quantization bits and maximum allowed transmit power.

In the next section, we will discuss the system and signal model.

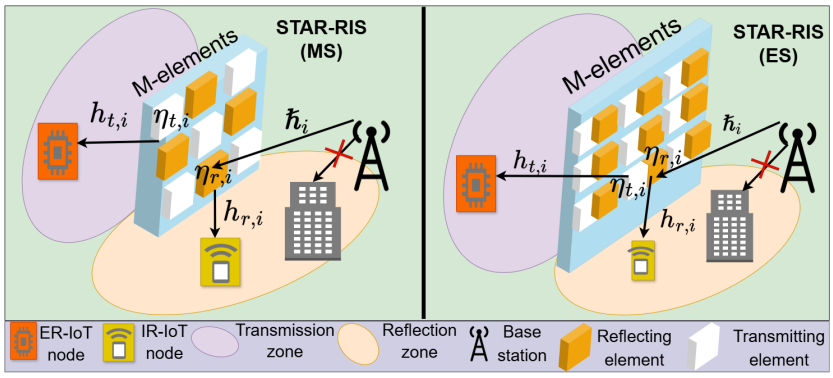


Figure 6.1: System model of STAR-RIS assisted SWIPT-IoT communication operating in ES and MS mode, simultaneously serving IR in reflection zone and ER in transmission zone.

6.2 System Model

The system model described in Fig. 6.1, depicts the simultaneous wireless communication between the single antenna base station (BS) and single antenna IR and ER, via STAR-RIS consisting of M elements having capabilities of serving ER present in the transmission zone with simultaneously serving the IR in the reflection zone. The direct transmission between BS and IR or ER is assumed to be blocked by an obstacle. The complex channel vector from BS to i^{th} STAR-RIS element is $\tilde{\hbar}_i = \hbar_i e^{j\phi_i}$, i^{th} element of STAR-RIS to IR is $\tilde{h}_{r,i} = h_{r,i} e^{j\varphi_{r,i}}$ and STAR-RIS i^{th} element to ER is $\tilde{h}_{t,i} = h_{t,i} e^{j\varphi_{t,i}}$. The channel magnitudes are denoted by $(\hbar_i, h_{r,i}, h_{t,i})$ and phases are represented as $(\phi_i, \varphi_{r,i}, \varphi_{t,i} \in [0, 2\pi))$. The transmission coefficient of the i^{th} STAR-RIS element has magnitude $\eta_{t,i}$ and phase $\theta_{t,i}$. Similarly, the reflection coefficient magnitude is $\eta_{r,i}$ with phase $\theta_{r,i}$, such that $\{\eta_{t,i}, \eta_{r,i}\} \in [0, 1]$ and $\{\theta_{t,i}, \theta_{r,i}\} \in [0, 2\pi)$ [99]. Following the law of energy conservation, $(\eta_{t,i})^2 + (\eta_{r,i})^2 = 1$. The BS with P_b power transmits signal $x = \sqrt{P_b}(\sqrt{K_r} s_r + \sqrt{K_t} s_t)$, where K_r and K_t are fraction of total power for IR (reflection side) and ER (transmission side) [100], s_r and s_t as their respective symbols with unit normalized power $\mathbb{E}\{|s_r|^2\} = \mathbb{E}\{|s_t|^2\} = 1$, where $\mathbb{E}\{.\}$ represents expectation.

The impractical system theoretically considers the CPS with infinite (very large) phase shift levels. The hardware implementation of RIS elements requires PIN diode for phase change and beamforming. Each PIN diode represents a bit b. The number of DPS level L depends on these bits as $L = 2^b$. These discrete phase samples belong to the set $\mathcal{S} = \{0, 2\pi/L, \ldots, 2\pi(L-1)/L\}$ [106]. Keeping large PIN diodes for each element (more than 100) for phase adjustment makes the STAR-RIS module bulky and difficult to implant [55]. Thus, we include DPS in our analysis with STAR-RIS elements phases $\{\theta_{t,i}, \theta_{r,i}\} \in \mathcal{S}$.

6.2.1 SWIPT with STAR-RIS in Energy Splitting mode

In ES, each element of STAR-RIS operates in reflection mode and transmission mode together, thus the users on both the sides can be served at once by each element, as illustrated in Fig. 6.1. The incident energy on i^{th} element is split for transmission side and reflection side with transmitting and reflectivity factors $\eta_{t,i}$ and $\eta_{r,i}$, respectively. The signal received by IR is given by

$$y_I = \sqrt{P_b}\left(\sum_{i=1}^{M} \tilde{\hbar}_i \eta_{r,i} \tilde{h}_{r,i} e^{j\theta_{r,i}}\right)\left(\sqrt{K_r}s_r + \sqrt{K_t}s_t\right) + w_I, \tag{6.1}$$

where $w_I \sim \mathcal{CN}(0, W_I^2)$ is the additive white Gaussian noise (AWGN) at the IR. In order to simplify the system analysis, it is assumed that the transmitted s_t signal is completely known at the IR and it is capable of completely canceling out the interference caused by s_t. Hence, there exists no interference term in the received SNR by the IR [101, 102], represented as

$$\Gamma_I = \frac{P_b K_r}{W_I^2}\left|\sum_{i=1}^{M} \hbar_i \eta_{r,i} h_{r,i} e^{j(\theta^*_{r,i} + \phi_i + \varphi_{r,i})}\right|^2. \tag{6.2}$$

It is assumed that the perfect Channel State Information (CSI) exists at the STAR-RIS elements that can generate the optimum phase shift maximizing end-to-end SNR [100].

For CPS, the optimized phase shift is $\theta_{r,i}^{*} = -(\phi_i + \varphi_{r,_i})$. In the case of DPS, $\theta_{r,i}^{*}$ is mapped to the nearest discrete values from set $\mathcal{S}$, denoted as $\widehat{\theta}_{r,i}$. There exists phase error ($\Delta\theta_{r,i} = \widehat{\theta}_{r,i} - \theta_{r,i}^{*}$) due to the limited discrete points, which impacts the SNR as [106]

$$\Gamma_I = \frac{P_b K_r}{W_I^2} \left| \sum_{i=1}^{M} \hbar_i \eta_{r,i} h_{r,i} e^{j\Delta\theta_{r,i}} \right|^2 . \tag{6.3}$$

The related data rate is represented as

$$R_I = \log_2(1 + \Gamma_I) = \log_2 \left(1 + \frac{P K_r Z_I}{W_I^2}\right). \tag{6.4}$$

The channel parameter related to communication with IR is $Z_I = \left| \sum_{i=1}^{M} \hbar_i \eta_{r,i} h_{r,i} e^{j\Delta\theta_{r,i}} \right|^2$. Similarly, the signal received by ER present on the transmission side is

$$y_E = \sqrt{P_b} \left(\sum_{i=1}^{M} \tilde{\hbar}_i \eta_{t,i} \tilde{h}_{t,i} e^{j\theta_{t,i}} \right) \left(\sqrt{K_r} s_r + \sqrt{K_t} s_t \right) + w_E, \tag{6.5}$$

where $w_E \sim \mathcal{CN}(0, W_E^2)$ is AWGN at the ER. The ER is capable of harvesting energy, which utilizes the complete received signal. The NL sigmoid based EH model is

$$E_h = \frac{E'}{1 - \chi} \left(\frac{1}{1 + \exp(-a(P_b K_r + P_b K_t) Z_E + ab)} - \chi \right). \tag{6.6}$$

The channel parameter associated with ER and the DPS related to transmission phase shift error ($\Delta\theta_{t,i}$) is $Z_E = \left| \sum_{i=1}^{M} \hbar_i \eta_{t,i} h_{t,i} e^{j\Delta\theta_{t,i}} \right|^2$ [107]. The other constant parameters a, b, χ, E' are circuit constants in the NL-EH modeling [53].

6.2.2 SWIPT with STAR-RIS in Mode Switching Framework

In Mode Switching operation of STAR-RIS, out of M total elements, M_t and M_r elements are dedicated exclusively for transmission and reflection operation, respectively such

that $M_t + M_r = M$, as given in Fig. 6.1. As per the energy conservation, the elements dedicated for reflection have $\eta_{t,_i} = 0, \eta_{r,_i} = 1$, and reverse for transmission only elements. The signal received by IR is

$$\overline{Y}_I = \sqrt{P_b}\left(\sum_{i=1}^{M_r} \tilde{\hbar}_i \eta_{r,i} \tilde{h}_{r,i} e^{j\theta_{r,i}}\right)\left(\sqrt{K_r}s_r + \sqrt{K_t}s_t\right) + w_I, \tag{6.7}$$

With the similar argument in ES of interference cancellation and applying DPS with phase error $\Delta\overline{\theta}_{r,i}$, the end-to-end SNR and data rate at IR are respectively represented as

$$\overline{\Gamma}_I = \frac{P_b K_r}{W_I^2}\left|\sum_{i=1}^{M_r} \hbar_i h_{r,i} e^{j\Delta\overline{\theta}_{r,i}}\right|^2, \quad \overline{R}_I = \log_2(1+\overline{\Gamma}_I) = \log_2\left(1 + \frac{P_b K_r \overline{Z}_I}{W_I^2}\right). \tag{6.8}$$

The NL-EH at the ER is given as

$$\overline{E}_h = \frac{E'}{1-\chi}\left(\frac{1}{1+\exp(-a(P_b K_r + P_b K_t)\overline{Z}_E + ab)} - \chi\right). \tag{6.9}$$

The associated channel parameter with transmission phase shift error ($\Delta\overline{\theta}_{t,i}$) is $\overline{Z}_E = \left|\sum_{i=1}^{M_t} \hbar_i h_{t,i} e^{j\Delta\overline{\theta}_{t,i}}\right|^2$.

Remark: In the time switching (TS) mode of operation of STAR-RIS, the whole STAR-RIS with all its elements works in reflection mode for a time instant serving IR, for another time instant it switches to transmission mode serving ER. Its functionality is similar to ES, where $\eta_{r,_i} = 1$ at a time for IR and $\eta_{t,_i} = 1$ for ER in the next time slot [106].

6.3 Problem Formulation and Solution

In this section, we define the primal optimization problem and analyze its inherent properties to check its complexity. We then develop a suitable algorithm to guide the solution process.

6.3.1 Weighted Rate-Energy Maximization Problem

Herein, we present the main problem associated with the maximization of the weighted data rate of IR and weighted EH of ER, such that holistic behavior can be analyzed. The optimized values of transmit power and power allocation ratio for IR (K_r) and ER ($K_t = 1 - K_r$) can be sought, while adhering to the constraints on data rate, EH, maximum allowed transmit power, and the allocation factor. We perform a rigorous assessment for both the ES and MS operations. For further simplicity, we introduce the notation for WRE function $\big(\mathcal{W}_x(P_b, K_r)\big)$, which takes two different cases of ES $\big(\mathcal{W}_E(P_b, K_r)\big)$, and MS $\big(\mathcal{W}_M(P_b, K_r)\big)$ expressed as follows.

$$\underset{\forall x \in [E,M]}{\mathcal{W}_x(P_b, K_r)} := \begin{cases} \mathcal{W}_E(P_b, K_r) = w_r R_I + w_e E_h \ : \text{ES} \\ \mathcal{W}_M(P_b, K_r) = w_r \overline{R}_I + w_e \overline{E}_h : \text{MS} \end{cases} \tag{6.10}$$

The weights w_r and w_e corresponds to the data rate of IR and EH of ER, respectively. The values are adjusted by the network operator depending on the priority of the ER or IR service required as per user demands [31]. The special notation denoted by $\mathcal{W}_x(P_b, K_r)$ signifies the choice of x from the set $[E, M]$ based on the selected case. Specifically, $\mathcal{W}_x(P_b, K_r)$ corresponds to either $\mathcal{W}_E(P_b, K_r)$, or $\mathcal{W}_M(P_b, K_r)$ at any given time, as defined in (6.10).

The objective of problem $(P1)$ is to maximize the metric $\mathcal{W}_x(P_b, K_r)$. The mathematical

representation of the overall optimization problem is defined as

$$\text{(P1): } \underset{P_b, K_r}{\text{maximize}} \quad \mathcal{W}_x(P_b, K_r) \quad \forall\, x \in [E, M] \tag{6.11}$$

$$\text{subject to :} \quad \text{(C1): } R \geq \mathcal{R}_{th}, \;\; R \in [R_u, \overline{R}_u] \tag{6.12}$$

$$\text{(C2): } \xi \geq \xi_{th}, \;\; \xi \in [E_h, \overline{E}_h] \tag{6.13}$$

$$\text{(C3): } P_b \leq \mathcal{P}_{\text{max}}, \tag{6.14}$$

$$\text{(C4): } 0 \leq K_r \leq 1. \tag{6.15}$$

In (6.12) and (6.13), $R \in [R_u, \overline{R}_u]$ and $\xi \in [E_h, \overline{E}_h]$ means $R = R_u, E = E_h$ for $\mathcal{W}_E(P_b, K_r)$ objective for ES case. While $R = \overline{R}_u, E = \overline{E}_h$ for $\mathcal{W}_M(P_b, K_r)$ objective for MS case. $\mathcal{R}_{th}$ and ξ_{th} are required data rate, and corresponding desired EH. Additionally, we have an upper limit on transmit power denoted as $\mathcal{P}_{\text{max}}$.

6.3.2 Proposed Solution

We seek suitable solution(s) of the primal weighted maximization problem (P1) with the proposed algorithm and compare its robustness in the later section.

The weighted objective of (P1) has both Rate and non-linear Energy term with optimizing variables K_r and P_b enveloped in the objective as well as in the non-convex constraint. Seeking direct solution of such non-convex problem possess immense challenge. Thus, we propose an algorithm which breaks the complex problem of (P1) into sub-problems taking one variable at a time, while fixing the other. In the convex optimization methodology, it is termed as the AO technique which is based on the divide-and-conquer approach [108]. The

respectively broken down sub-problems $(\text{P1})_{\text{a}}$ and $(\text{P1})_{\text{b}}$ are mathematically defined as

$$(\text{P1})_{\text{a}} : \underset{P_b}{\text{maximize}} \quad \mathcal{W}_x(P_b, K_r) \quad \forall\, x \in [E, M] \tag{6.16}$$

$$\text{subject to :} \quad P_b \geq \frac{W_I^2}{K_r \mathbb{Z}_I}\big(2^{\mathcal{R}_{th}} - 1\big), \mathbb{Z}_I \in [Z_I, \overline{Z}_I] \tag{6.17}$$

$$P_b \geq \frac{b}{\mathbb{Z}_E} - \frac{\ln(\Sigma)}{a\mathbb{Z}_E}, \mathbb{Z}_E \in [Z_E, \overline{Z}_E] \tag{6.18}$$

$$P_b \leq \mathcal{P}_{\text{max}}. \tag{6.19}$$

$$(\text{P1})_{\text{b}} : \underset{K_r}{\text{maximize}} \quad \mathcal{W}_x(P_b, K_r) \quad \forall\, x \in [E, M] \tag{6.20}$$

$$\text{subject to :} \quad K_r \geq \frac{W_I^2}{P_b \mathbb{Z}_I}\big(2^{\mathcal{R}_{th}} - 1\big), \mathbb{Z}_I \in [Z_I, \overline{Z}_I] \tag{6.21}$$

$$0 \leq K_r \leq 1. \tag{6.22}$$

where $\Sigma = \left(\frac{(1-\chi)(E'-\xi_{th})}{\xi_{th}(1-\chi)+\chi E'}\right)$. In (6.17), (6.18), and (6.21) $\mathbb{Z}_I \in [Z_I, \overline{Z}_I]$ and $\mathbb{Z}_E \in [Z_E, \overline{Z}_E]$, respectively. It means that for the ES mode of transmission, i.e., for $\mathcal{W}_E(P_b, K_r)$ the objective assumes $\mathbb{Z}_I = Z_I, \mathbb{Z}_E = Z_E$; while for the MS transmission mode the $\mathcal{W}_M(P_b, K_r)$ objective takes the value of $\mathbb{Z}_I = \overline{Z}_I, \mathbb{Z}_E = \overline{Z}_E$ in the constraints evaluation. The Algorithm 6.1 defines the guiding steps for solving (P1) in alternating fashion, utilizing sub-problems $(\text{P1})_{\text{a}}$ and $(\text{P1})_{\text{b}}$. We begin by initializing the array $\mathcal{W}_x$ with $x = E$ or M (i.e., either for ES case or MS case at a time) and assigning two feasible initial values to K_r. Initially, we fix K_r and compute P_b by solving the sub-problem $(\text{P1})_{\text{a}}$. Subsequently, the value of P_b is updated in sub-problem $(\text{P1})_{\text{b}}$ as computed from the previous step, and thus the optimized K_r is obtained. Now, with the optimized values of P_b and K_r, we proceed to solve for $\mathcal{W}_x$. If the current value of $\mathcal{W}_x$ is less than its value from the previous iteration, or if the iteration count reaches the predefined limit t', the process terminates. Otherwise, the computed values are stored, and the iteration continues until a lower value of $\mathcal{W}_x$ is found. Through this iterative procedure, the optimized values P_b^* and K_r^* are obtained. The proposed method is detailed in Algorithm 6.1.

Algorithm 6.1 Iterative Maximization of WRE

1: **Initialize:** Set $\mathcal{W}_x^{(1)} = \mathcal{W}_x^{(2)}$, $K_r^{(1)} = K_r^{(2)}$, and iteration limit t'. Initialize the iteration counter $t = 2$.
2: **Step 1:** Solve sub-problem $(\text{P1})_\text{a}$ by fixing $K_r^{(t)}$ to optimize $P_b^{(t+1)}$.
3: **Step 2:** Solve sub-problem $(\text{P1})_\text{b}$ using $P_b^{(t+1)}$ from Step 1 to optimize $K_r^{(t+1)}$.
4: **Step 3:** Compute the updated value $\mathcal{W}_x^{(t+1)}$ using $P_b^{(t+1)}$ and $K_r^{(t+1)}$.
5: **Step 4: Convergence Check**

- **If** $\mathcal{W}_x^{(t+1)} \geq \mathcal{W}_x^{(t)}$ **and** $t < t'$, update $t = t + 1$, $K_r^{(t)}$ and return to Step 1.
- **Else** (if $\mathcal{W}_x^{(t+1)} < \mathcal{W}_x^{(t)}$ **or** $t \geq t'$), terminate the loop.

6: **Output:** The optimized function value $\mathcal{W}_x^{(t)}$.

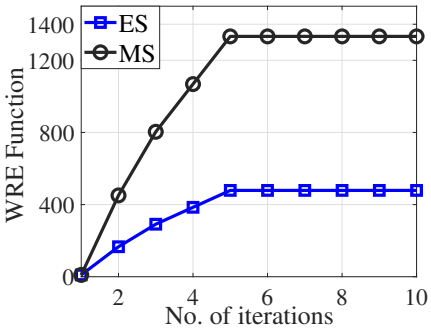


Figure 6.2: Convergence of WRE function for ES and MS mode of transmission considering Case 2 (Table 6.2).

6.3.2.1 Computational Complexity

To validate the performance of Algorithm 6.1, Fig. 6.2 shows the convergence plot (averaged 500 channel realizations) of WRE objective for both the ES and MS cases with both converging in almost $I = 5$ iterations. The computation complexity is $\mathcal{O}(I(\kappa_1 + \kappa_2))$. Here κ_1 and κ_2 in the computation time of Step 1 and Step 2 respectively, which depends on M^2 for ES and M_t^2 ($M_t > M_r$) or M_r^2 ($M_r > M_t$) for MS.

6.4 Results and Discussion

This section presents the numerical evaluation pertaining to the performance of the proposed solutions via simulations. As mentioned in Section 6.2, the Rician fading models all

Table 6.2: Simulation cases for ES and MS.

	ES		MS	
	$(\eta_r)^2$	$(\eta_t)^2$	M_r	M_t
Case 1	0.5	0.5	100	100
Case 2	0.8	0.2	80	120

the channels, i.e., the BS→STAR-RIS i^{th} element ($\tilde{\hbar}_i$), i^{th} element STAR-RIS →IR ($\tilde{h}_{r,i}$) and i^{th} element STAR-RIS→ER ($\tilde{h}_{t,i}$), mathematically represented as [99]

$$\tilde{\hbar}_i = \sqrt{\frac{C_0}{d_1^{\nu_1}}}\left(\sqrt{\frac{K_1}{K_1+1}}\bar{\hbar}_i + \sqrt{\frac{1}{K_1+1}}\hat{\hbar}_i\right), \tag{6.23}$$

$$\tilde{h}_{r,i} = \sqrt{\frac{C_0}{d_2^{\nu_2}}}\left(\sqrt{\frac{K_2}{K_2+1}}\bar{h}_{r,i} + \sqrt{\frac{1}{K_2+1}}\hat{h}_{r,i}\right), \tag{6.24}$$

$$\tilde{h}_{t,i} = \sqrt{\frac{C_0}{d_3^{\nu_3}}}\left(\sqrt{\frac{K_3}{K_3+1}}\bar{h}_{t,i} + \sqrt{\frac{1}{K_3+1}}\hat{h}_{t,i}\right), \tag{6.25}$$

where C_0 is the reference path loss, $[K_1, K_2, K_3]$ are Rician factors, $[d_1, d_2, d_3]$ separation distances, and $[\nu_1, \nu_2, \nu_3]$ are the path loss exponent corresponding to the BS→STAR-RIS, STAR-RIS→IR and STAR-RIS→ER channels, respectively. Additionally, $\{\bar{\hbar}_i, \bar{h}_{r,i}, \bar{h}_{t,i}\}$ are Line-of-Sight (LoS) component and $\{\hat{\hbar}_i, \hat{h}_{r,i}, \hat{h}_{t,i}\}$ are the non Line-of-Sight (nLoS) component, in the Rician fading model.

The specific values of other parameters unless stated are depicted in Table 6.3 with total $M = 200$ STAR-RIS elements. Table 6.2, represents various simulation cases for ES with different energy divide ratio, reflection or transmission coefficient values (i.e., letting $\{\eta_{r,i}\}_{i=1}^{M} = \eta_r, \{\eta_{t,i}\}_{i=1}^{M} = \eta_t$) and MS with different element division for reflection and transmission. Case 1 advocates for equal divide of energy (ES) and elements (MS). Both of these cases are compared and analyzed for different parameters.

Table 6.3: Parameter values' initializations

Parameters	Values	Parameters	Values
C_0	-20 dB	$\mathcal{R}_{th}$	10 bps/Hz
d_1	10 m	$\mathcal{P}_{\max}$	5W
$d_2 = d_3$	5 m	ξ_{th}	1 μJ
$\nu_1 = \nu_2 = \nu_3$	2.2	E'	2.8 mJ [55]
$K_1 = K_2 = K_3$	2	a	1500 [55]
$W_I^2 = W_E^2$	-70 dBm	b	0.0022 [55]
w_r	0.01 units/bps/Hz	w_e	10^6 units/J

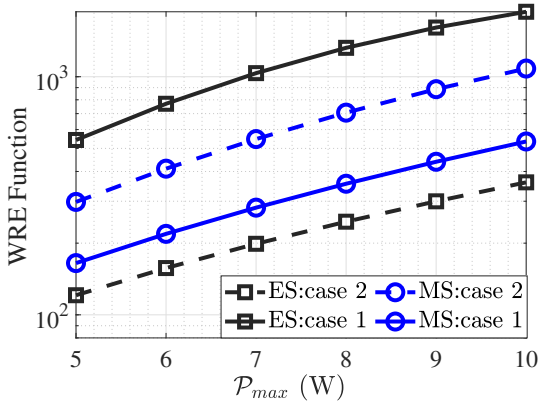


Figure 6.3: ES and MS comparison for various cases described in Table. 6.2.

6.4.1 Impact of Energy Split and Element Division

Fig. 6.3 provides a comparative study of various cases of energy splitting ratios of ES and element divide cases for MS, while maximizing the WRE function for various maximum allowed transmit power. For Case 1, ES performs better than MS due to the utilization of all elements $M = 200$ in ES, increasing diversity gain. Whereas for the Case 2, MS has higher WRE function than ES because of the dropped down channel parameter in ES due to lower transmission coefficient or energy split ratio of just 0.2. This fair comparison shows that any of the transmission protocol (ES or MS) works better depending on the energy split ratio and how the elements are divided.

Fig. 6.4 compares three different types of solutions for (P1), i.e., algorithmic solution, joint optimization (JO) solution, and the baseline solution utilizing parameters of Case 1.

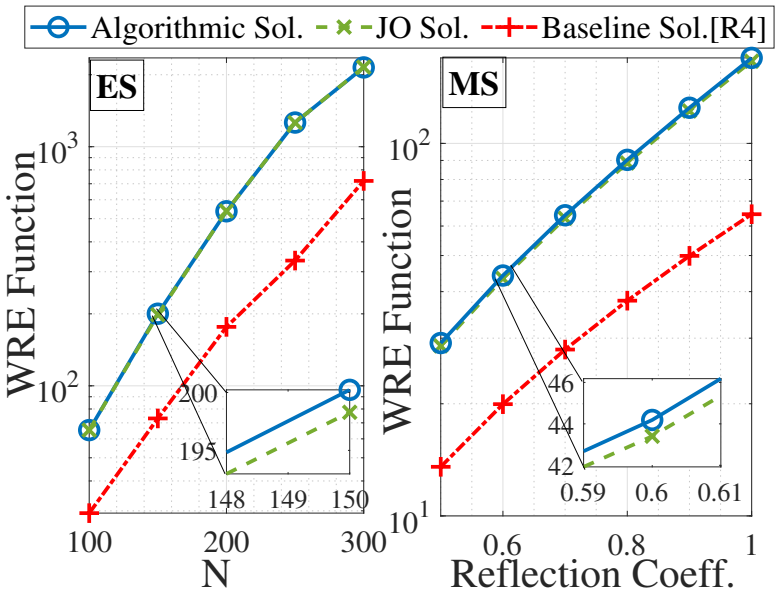


Figure 6.4: Various types of solution comparisons for ES and MS with the number of STAR-RIS elements and reflection coefficient. Here, baseline solution [R4] corresponds to [4].

WRE is varied for a total number of STAR-RIS elements in the ES mode, while different reflection or transmission coefficients are varied to study WRE in the MS mode. It is obvious that the WRE increases with appreciating values of M and η_r or η_t. The Algorithmic solution utilizes Algorithm 6.1, where the JO solution is given by MATLAB's non-linear solver *fmincon*$(\cdot)$ for jointly optimizing K_r and P_b simultaneously. The baseline solution is constructed following the variable-fixing approach adopted in [4][109]. Specifically, K_r is fixed to 0.5 (equal power divide), while the original objective function and constraints are retained, and the resulting single-variable optimization problem with respect to P_b is solved. Thus, the baseline corresponds to a restricted version of the original joint optimization problem, rather than an independently formulated optimization problem.

The closeness of the algorithmic solution to the JO, proves the effectiveness and accuracy of the proposed Algorithm. The baseline solution performs the least for the obvious reason of under optimized solution.

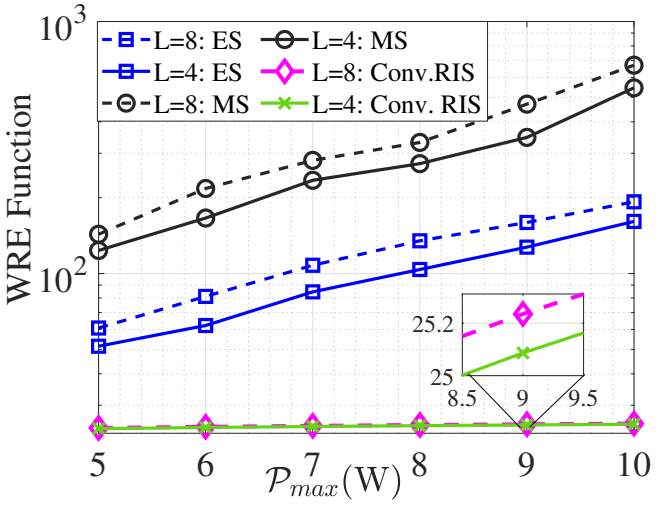


Figure 6.5: Impact of DPS levels on WRE function with $\mathcal{P}_{\text{max}}$ comparing conventional RIS.

6.4.2 Impact of DPS Levels

In Fig. 6.5 and Fig. 6.6, WRE function is analyzed for the DPS levels L, which indirectly depends on the quantization bits b ($L = 2^b$). The ES and MS STAR-RISs are compared with the conventional RIS in Fig. 6.5. For replicating the conventional RIS operation, there exists only reflection zone and thus no EH takes place. This will ultimately reduce the objective of WRE to be just Rate Maximization. The reflection coefficient of unity i.e., $\eta_r = 1$ is assumed with $\eta_t = 0$, such that the optimization problem become single variable with full power allocation for IR ($K_r = 1$). Consequently, the conventional RIS has the least performance. The higher DPS levels provide better performance for all the ES, MS, and conventional RIS case, but with an increased bulkiness in the device. Thus, we need to figure out the best possible quantization level to be utilized in the RIS phase design.

Fig. 6.6 provides the Cumulative Density Function (CDF) analysis of WRE for ES and MS protocols, respectively, with increasing DPS levels $L = [2, 8, 32]$ considering the Case 2 parameters. The CPS is assumed to have infinite levels ($L = \infty$) with null phase shift error (i.e., $\Delta\theta_{r,i}$ or $\Delta\overline{\theta}_{r,i} = 0$, $\Delta\theta_{t,i}$ or $\Delta\overline{\theta}_{t,i} = 0$). The DPS modeling is used for the present system characterization, the CPS is simulated by keeping $L = 1024$, $b = 10$. It is observed

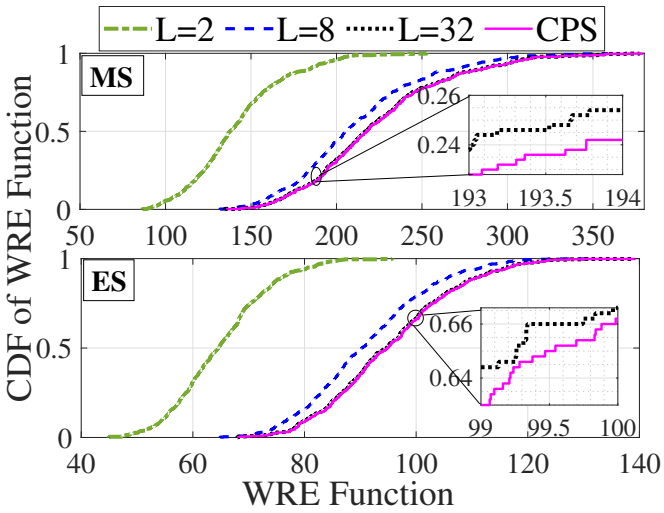


Figure 6.6: Impact of DPS level on CDF plot of maximized WRE for ES and MS comparing PS.

that WRE increases with the higher number of levels. From $L = 2$ to $L = 8$, there is a 36% increase in the WRE for ES, and 42% raise for the MS. It is worth observing that the plots for $L = 32$ and CPS case are almost inline for both ES and MS. Thus, for lesser number of level, we obtain almost similar performance. For instance, the present system works very well with 3 quantization bits ($L = 8$), which saves upon need for extra control diodes in our STAR-RIS device while ensuring good performance.

Thus, it is conferred that the competition between utilizing ES or MS protocol depends on the choice of the parameters for reflection and transmission zone. Therefore, the energy split ratio and STAR-RIS element's division for transmission and reflection zones, respectively, are very essential for the system design. WRE increases with total number of elements, maximum transmit power, and the number of quantization levels. The performance is almost similar to ideal CPS model with infinite levels, which can be achieved even with fewer quantization bits of the practical DPS model. It is evident that the conventional RIS with reflection only capabilities performs inferior to the STAR-RIS.

6.5 Summary

This chapter investigated a STAR-RIS assisted SWIPT framework, in which IR is located in the reflection region and ER is placed in the transmission region. The system performance is evaluated through the maximization of WRE metric, which jointly captures the classic R-E trade-off. To replicate the practical hardware behavior, the NL-EH of ER and DPS based STAR-RIS phase model is incorporated for the analytical evaluation. Both the ES and MS operational protocols are considered, where the selection depends on the reflection and transmission region's parameters. Consequently, the selection of the energy split ratio and STAR-RIS element allocation is essential for system performance. Numerical results of proposed framework present the effective WRE improvements with increasing STAR-RIS element count, higher transmit power budgets, and higher resolution of DPS levels. Moreover, the STAR-RIS SWIPT system outperforms the conventional reflect-only RIS architecture. Future extensions of this work includes the consideration of ICSI, robust optimization strategies, and inclusion of Integrated Sensing and Communication (ISAC) for next generation 6G wireless network.

Chapter 7

Conclusion and Future Directions

A brief summary and the major conclusions of the work performed in this thesis are provided in Section 7.1. Subsequently, the Section 7.2 outlines the possible future extensions of the considered frameworks.

7.1 Main Conclusions

Reconfigurable Intelligent Surfaces (RIS) is highly suitable for integration with Simultaneous Wireless Information and Power Transfer (SWIPT) enabled Internet-of-Things (IoT) networks, due to its advantageous coverage extension, passive nature, signal strength, and Energy Efficiency (EE) improvement. However, RIS-assisted SWIPT systems face critical challenges, including the joint optimization of system metrics and inclusion of practical deployable constrained. The complexity of these challenges amplifies with advanced system scenarios.

The work in this thesis addresses the several critical issues, by developing and analyzing a comprehensive optimization framework for the RIS-assisted SWIPT-IoT communication systems with multi-antenna, multi-user, multi RIS-user pair and distributed-RIS scenarios. This is done by incorporating several practical aspects such as RIS selection, imperfect

channel state information (CSI), discrete phase shift (DPS) model, phase-dependent reflection amplitude model, and sigmoid function based non-linear Energy Harvesting (NL-EH) model.

Next, distinct complex optimization problems were developed for maximization of Rate, Energy Harvesting (EH), EE and minimization of power, along with the weighted fractional formulations, under essential Quality-of-Service (QoS) and hardware related constraints, extended to joint active-passive beamforming design. Owing to their highly coupled and non-convex nature, these problems were addressed using advanced convex optimization techniques, including Zero Forcing (ZF), Semidefinite Relaxation (SDR), and Gaussian Randomization (GR) for quadratic objectives. In additions, Dinklebach Transform (DT) and Quadratic Transform (QT) for fractional formulations were addressed while being complemented by Alternate Optimization (AO) with a divide-and-conquer strategy and Karush-Kuhn-Tucker (KKT)-based closed-form solutions where applicable.

Sequentially, the proposed algorithms were compared for their execution time and performance. Numerical results showed that increasing RIS elements, RIS count, BS power and reducing placement distance enhances the data rate and EH, with gains saturating at higher DPS levels. Under limited base station (BS) transmit power, performance was maintained by increasing RIS size, BS antennas, users and phase quantization levels, while relaxing signal-to-interference-plus-noise ratio (SINR), EH targets, and separation distances.

Furthermore, Simultaneously Transmitting and Reflecting-RIS (STAR-RIS)-assisted SWIPT system was investigated to serve Energy Receiver (ER) and Information Receiver (IR) utilizing the Energy Splitting (ES) and Mode Switching (MS) operational means. A Weighted Rate-Energy (WRE) maximization problem was formulated for the optimal power parameters with practical DPS model, solved by an AO based technique. Numerical results showed that energy split ratio and element division significantly influence performance, with

optimal DPS selection balancing hardware complexity and efficiency.

Towards this end, the main contributions of this thesis are summarized below.

1. Different from several existing works in the literature, this thesis investigated three distinctly novel RIS-assisted and one STAR-RIS-assisted SWIPT-IoT system designs.

2. The designed frameworks were individually examined through advanced optimization-based mathematical rigor and analysis.

3. Suitable closed-form expressions, algorithms, and various convex optimization techniques were employed to solve the developed problems.

4. The validated algorithms were compared with the existing works for computation complexity and performance.

5. Inferences were drawn with varying system parameters, proving the robustness and correctness of the given optimal/sub-optimal solutions.

The next section discusses how the proposed frameworks in this thesis can be extended for the advanced wireless communication technologies.

7.2 Future Directions

Although the results presented in this thesis demonstrate the effectiveness of the proposed designs and optimization techniques for various RIS-assisted SWIPT-IoT systems, several opportunities for further research and extension still remain. This section highlights some promising directions and emerging challenges that may possibly be explored in the future work.

7.2.1 Potential Extensions

The following are a few proposed directions for future research related to RIS-assisted SWIPT systems.

1. In this thesis, an RIS-assisted communication system was developed for static SWIPT-IoT node scenario as evident from Chapters 3 and 4, 5. As an extension, the model could be generalized to incorporate user mobility, such as Uncrewed Aerial Vehicle (UAV)-assisted communications or Vehicular-IoT networks. This requires incorporating the dynamic channel variations and adaptive real-time RIS configuration.

2. Future research will focus on developing Machine Learning-based Optimization schemes that can achieve faster and more adaptive performance than the classical convex optimization techniques. In particular, the works in chapter 3 and 5 may further be explored with consideration of Reinforcement Learning (RL) algorithms such as Deep Deterministic Policy Gradient (DDPG), Proximal Policy Optimization (PPO), and Deep Q-Network (DQN) to enable joint active-passive beamforming, RIS selection, and TS or PS optimization under dynamic wireless conditions, to reduce computational complexity and enable real-time implementation. These data-driven methods have shown superior convergence behavior and adaptability compared to iterative convex solvers, and are expected to provide a 30–40% reduction in the convergence time while maintaining a near-optimal energy and spectral efficiency.

3. Practical and efficient methods for CSI estimation in robust RIS-assisted SWIPT systems may be incorporated in chapter 4. Here, the larger sized RIS leads to larger training of pilot symbols and due to highly dynamic environment, higher performance yearns for higher RIS elements. The ON/OFF based channel estimation leads to a significant power loss which increases the training overhead. It may reduced by grouping

the RIS elements into sub-surfaces and then applying ON/OFF scheme on each surface [110]. Another technique for mitigation of imperfect CSI due to largely scaled RIS includes, two-time scaled channel estimation for highly dimensional cascaded BS-RIS-user channels and Deep Learning based strategy for highly dynamic scenarios [111][112].

4. In chapter 6, the presented STAR-RIS framework may be employed with Integrated Sensing and Communication (ISAC) framework, enabling simultaneous communication, energy transfer, and environmental sensing for smart IoT applications with extended coverage. This can serve three type of users, energy users, communication/information users, and sensing users, present all around the STAR-RIS.

5. To provide a realistic quantitative characterization of the smart-agriculture deployment as covered in chapter 5, we may employ the Siradel 3D ray-tracing (RT) platform for site-specific propagation analysis. Siradel's RT engine supports vegetation and terrain modeling, and multi-band rural propagation prediction, making it well suited for farm-scale evaluation despite the lack of prior agriculture-focused Siradel studies. Existing research demonstrates 'Siradel Inowave' RT tool's accuracy in complex 3D environments, including RIS-enabled industrial scenarios [113]. Leveraging these validated capabilities, realistic power map (in the range of mJ-μJ), path-loss statistics, sensor device density (50–100 count per hectare), and BS-RIS-U channel link parameters for representative farm layouts and sub-GHz or ISM bands are generated [114]. The resulting ray-tracing outputs are integrated into the system-level analysis to support a quantitatively grounded assessment of RIS-assisted SWIPT performance in rural IoT environments.

7.2.2 Towards Novel Problem Formulations and Solutions

In this section, we discuss advancement of RIS technologies with possible integrated SWIPT-IoT systems. Few novel problems which can be taken as future work are enumerated as follows.

1. **ISAC with RIS- assisted SWIPT-IoT Systems**

   The integration of ISAC with RIS- assisted SWIPT-IoT Systems presents a promising approach for concurrently serving ground users and sensing targets across terrestrial, maritime, and aerial domains. However, such a design introduces increased complexity, particularly in ensuring user fairness between communication and energy services. SWIPT technology enables dual-functional BSs (DFBS) to simultaneously transmit signals to both information users and energy receivers. Specifically, users that decode information from the DFBS are referred to as communication users, whereas devices that harvest energy from the received signals are termed energy receivers [115]. These energy receivers typically consist of low-power IoT devices that require only a minimal amount of power to meet their QoS requirements.

2. **RIS-assisted Free space Optics (FSO) Communication**

   Free Space Optics (FSO) Communication provides several benefits, such as increased bandwidth and higher throughput, compared to RF communication. As the licensed spectrum are limited and expensive, FSO is a potential candidate for the unlicensed spectrum management. However, FSO links are negatively impacted by atmospheric conditions like fog, cloud or smog, turbulence, and pointing errors, and additionally by obstacles between the transmitter and receiver. FSO when paired with optical-based RIS, potentially enhances its reliability and coverage, specially overcomes the barriers in the Line-of-Sight (LoS) path [116].

3. **RIS-assisted Vehicular-to-Everything (V2X) Communication**

   The Internet-of-Vehicles (IoV) plays a crucial role in Intelligent Transportation Systems (ITS) and is advancing swiftly through the integration of smartly connected vehicles. IoV enabled vehicular systems open up the prospect to interact via V2X communications. Two primary technologies have been employed for V2X communications: one is dedicated for short-range communication (DSRC), while the other being the Vehicular Networks based on Cellular Technology. DSRC is commercially popular but fails for dense and high-mobility environments, adversely affecting the coverage, QoS and data rate, leading to unreliable channel delays. Utilizing RIS for V2X scenarios has potential for improving the QoS [41]. Though modeling RIS-V2X scenarios with practical delay-Doppler shift is challenging, opening the doors for new the research area.

4. **Security and privacy enhancement by Rate-Splitting Multiple Access (RSMA)**

   RSMA enhances physical-layer security by dividing messages into common and private parts, ensuring controlled data sharing among users. RIS element splitting is effective with RSMA, where the optimal number of elements are configured to assist in efficiently decoding both message components [117]. In RIS-enabled SWIPT-IoT networks, RSMA mitigates eavesdropping risks from BS transmissions by dynamically adjusting power and rate allocation. This flexible structure offers robustness against imperfect CSI and interference, while preserving user privacy and enhancing both the spectral and energy efficacy.

5. **Stacked Intelligent Metasurfaces (SIM)**

   Instead of keeping the single layer of fabricated metamaterials on a substrate in conventional RIS, the SIM has a multiple stacked metasurface structure [118]. De-

ployed at the BS and receiver, SIM architecture handles transmit or receive beamforming directly in the electromagnetic wave domain for the implementation of holographic multi-input-multi-output (HMIMO), using only low-resolution digital-to-analog-converter (DAC) and fewer RF chains. This makes system more energy-efficient.

In conclusion, this thesis presented several advanced system designs and optimization techniques for the RIS-assisted SWIPT-IoT framework. It is expected that the insights and findings discussed in the thesis will contribute toward the development of sustainable and efficient next generation Wireless Communication System.

APPENDIX

Appendix A

Optimization Techniques

In general, an optimization problem is mathematically expressed as follows

$$\begin{aligned} \underset{\mathbf{x}}{\text{maximize/minimize}} \quad & f(\mathbf{x}) \\ \text{subject to:} \quad & g_i(\mathbf{x}) \leq 0, \quad i = 1, 2, \ldots, m, \\ & h_j(\mathbf{x}) = 0, \quad j = 1, 2, \ldots, n, \end{aligned} \tag{A.1}$$

where $f(x)$ denotes the objective function, x represents the optimization variables, and $g_i(\mathbf{x})$ and $h_j(\mathbf{x})$ denote the inequality and equality constraints, respectively.

A.1 Relevant Optimization Techniques

In this section, the explanation related to the various categories of the optimization technique is covered.

A.1.1 Classification based on Uncertainty

Optimization problems can be categorized based on the availability and certainty of system information.

1. **Deterministic Optimization:** All system parameters are assumed to be perfectly

known and fixed. The objective function and constraints are represented using deterministic mathematical expressions.

2. **Stochastic Optimization:** One or more system parameters are random or uncertain in nature. Stochastic optimization incorporates probabilistic models to optimize the expected system performance under uncertain conditions.

A.1.2 Classification based on Optimization Objective

Optimization problems may also be classified according to the number of objectives involved. It is divided into two categories, namely, single-objective optimization and multi-objective optimization problem. The former is simple to solve and deals with one performance metric solely, while the latter is complicated and focuses on the optimization of multiple conflicting objectives, often looking for the balance with the metrics having trade-offs.

A.1.3 Classification based on the Nature of Variables

Optimization problems can also be classified according to the type of optimization variables involved, defined as follows

1. **Continuous Optimization:** Problems involve real-valued variables that can take any value within a feasible range. These problems are commonly solved using convex optimization techniques and gradient-based iterative methods.

2. **Discrete Optimization:** The function involves integer or binary-valued optimization variables. For example, discrete phase shift optimization in RIS-assisted communication systems, where RIS elements can only support quantized phase values due to

hardware limitations. These type of problems are generally combinatorial and computationally more complex.

3. **Mixed-Integer Nonlinear Programming (MINLP):** It involves both continuous and discrete variables along with nonlinear objective functions or constraints. MINLP problems are highly challenging due to the coexistence of integer constraints and nonlinear relationships. Such problems are generally NP-hard and require advanced optimization methods to solve [119].

A.1.4 Classification based on Nature of Constraints

Optimization problems may further be classified according to the nature of constraints imposed on the optimization variables, namely unconstrained, constrained, and bound-constrained optimization. As the name suggests, the lesser practical unconstrained optimization problem does not explicitly contain any type of constraint. The objective is optimized over a complete solution space. The constrained optimization involves any equality or non-equality feasibility functions defining solution space. Bound-constrained optimization represents a special case where optimization variables are restricted within upper and lower bounds.

A.2 Leveraged Optimization Techniques

Several optimization techniques are employed in this Thesis to solve the RIS-assisted Wireless Communication problems efficiently. They are listed and discussed as follows.

A.2.1 Karush-Kuhn-Tucker (KKT) Conditions

The KKT conditions constitute one of the most important mathematical tools for solving constrained optimization problems. It extends the classical Lagrange multiplier method to optimization problems involving both equality and inequality constraints. For a general constrained optimization problem mathematically represented as.

$$\begin{aligned} \underset{\mathbf{x}}{\text{minimize}} \quad & f(\mathbf{x}) \\ \text{subject to} \quad & g_i(\mathbf{x}) \leq 0, \quad i = 1, 2, \ldots, m, \\ & h_j(\mathbf{x}) = 0, \quad j = 1, 2, \ldots, n, \end{aligned} \tag{A.2}$$

The corresponding Lagrangian function is expressed as

$$\mathcal{L}(\mathbf{x}, \lambda_i, \nu_j) = f(\mathbf{x}) + \sum_{i=1}^{m} \lambda_i g_i(\mathbf{x}) + \sum_{j=1}^{n} \nu_j h_j(\mathbf{x}), \tag{A.3}$$

where λ_i and ν_j denote the Lagrange multipliers associated with inequality and equality constraints, respectively. The KKT optimality conditions are given as follows:

- **Stationarity Condition**

$$\nabla f(\mathbf{x}^*) + \sum_{i=1}^{m} \lambda_i \nabla g_i(\mathbf{x}^*) + \sum_{j=1}^{n} \nu_j \nabla h_j(\mathbf{x}^*) = 0. \tag{A.4}$$

- **Primal Feasibility**

$$g_i(\mathbf{x}^*) \leq 0, \quad h_j(\mathbf{x}^*) = 0. \tag{A.5}$$

- **Dual Feasibility**

$$\lambda_i \geq 0. \tag{A.6}$$

- **Complementary Slackness**

$$\lambda_i g_i(\mathbf{x}^*) = 0. \tag{A.7}$$

In convex optimization problems satisfying certain regularity conditions, such as Slater's condition, the KKT conditions also become sufficient for achieving global optimality [95].

A.2.2 Semidefinite Programming (SDP)

Semidefinite Programming (SDP) is a powerful convex optimization framework used for solving optimization problems involving matrix variables and linear matrix inequalities. SDP belongs to the class of convex optimization problems and can be efficiently solved using interior-point methods. SDP provides an effective approach to transform non-convex problems into tractable convex forms through Semidefinite Relaxation (SDR), in which non-convex rank-one constraints are relaxed, thereby converting the original optimization problem into a convex Semidefinite program. For a positive Semidefinite optimization matrix variable ($\mathbf{X}$), the SDR problem structure is mathematically written as.

$$\begin{aligned} \underset{\mathbf{X}}{\text{minimize}} \quad & \mathrm{Tr}(\mathbf{C}\mathbf{X}) \\ \text{subject to} \quad & \mathrm{Tr}(\mathbf{A}_i\mathbf{X}) \leq b_i, \quad i = 1, 2, \ldots, m, \\ & \mathbf{X} \succeq 0. \end{aligned} \tag{A.8}$$

The relaxed problem can then be solved efficiently using standard convex optimization solvers such as CVX [119].

A.2.3 Gaussian Randomization

After applying SDR, the original rank-one constraint is relaxed, which results in a convex SDP problem. However, the obtained solution matrix may not satisfy the required rank-one constraint i.e., $\mathrm{rank}(\mathbf{X}) = 1$. Gaussian Randomization is therefore employed to recover an approximate feasible rank-one solution from the relaxed SDP solution. Initially, L number of randomized candidate vectors are generated according to the complex Gaus-

sian distribution, mathematically given by

$$\mathbf{v}_l \sim \mathcal{CN}(\mathbf{0}, \mathbf{X}), \tag{A.9}$$

where $\mathbf{v}_l$ denotes the l^{th} randomized vector and $\mathbf{X}$ represents the covariance matrix obtained from SDR. The generated L random vectors are normalized to satisfy the problem constraints, and the best feasible solution is selected based on the objective function as

$$\mathbf{v}^* = \arg\max_{\mathbf{v}_l} f(\mathbf{v}_l). \tag{A.10}$$

The accuracy of Gaussian Randomization generally improves with an increase in the number of randomized trials L [119].

A.2.4 Fractional Programming

Fractional Programming framework is used for solving optimization problems involving ratio-based objectives. A general fractional optimization problem can be represented as

$$\underset{\mathbf{x}}{\text{maximize}} \quad \eta(\mathbf{x}) = \frac{R(\mathbf{x})}{P(\mathbf{x})}, \tag{A.11}$$

Using Dinkelbach's transformation, the fractional objective function can be converted into the following subtractive form [54, 55, 95]

$$\underset{\mathbf{x}}{\text{maximize}} \quad R(\mathbf{x}) - \mu P(\mathbf{x}), \tag{A.12}$$

where μ is iteratively updated as

$$\mu^{(k+1)} = \frac{R(\mathbf{x}^{(k)})}{P(\mathbf{x}^{(k)})}. \tag{A.13}$$

The iterative process continues until the convergence is achieved, i.e.,

$$R(\mathbf{x}^{(k)}) - \mu^{(k)} P(\mathbf{x}^{(k)}) \leq \epsilon, \tag{A.14}$$

where ϵ denotes the convergence tolerance. Using the quadratic transform, the above fractional function can be equivalently rewritten as

$$2y\sqrt{R(\mathbf{x})} - y^2 P(\mathbf{x}), \tag{A.15}$$

where y is an auxiliary variable introduced to decouple the numerator and denominator terms. The optimal value of the auxiliary variable is obtained as

$$y^* = \frac{\sqrt{R(\mathbf{x})}}{P(\mathbf{x})}. \tag{A.16}$$

The quadratic transform converts the original non-convex fractional problem into an equivalent optimization problem that can be efficiently solved using iterative optimization techniques [55].

A.2.5 Alternate Optimization (AO)

It is an iterative optimization framework widely used for solving coupled non-convex optimization problems [120, 121]. Joint optimization of all variables simultaneously is often mathematically intractable. AO addresses this issue by decomposing the original optimization problem into smaller sub-problems.

Consider an optimization optimization problem involving two coupled variable blocks $\mathbf{x}$ and $\mathbf{y}$, as follows.

$$\underset{\mathbf{x},\mathbf{y}}{\text{maximize}} \quad f(\mathbf{x}, \mathbf{y}). \tag{A.17}$$

In AO, one group of variables is optimized while keeping all remaining variables fixed. The process is repeated iteratively until convergence is achieved. At iteration k, the optimization steps are given as

$$\mathbf{x}^{(k+1)} = \arg\max_{\mathbf{x}} f(\mathbf{x}, \mathbf{y}^{(k)}), \quad \mathbf{y}^{(k+1)} = \arg\max_{\mathbf{y}} f(\mathbf{x}^{(k+1)}, \mathbf{y}). \tag{A.18}$$

The iterative optimization process continues until the convergence criterion is satisfied, i.e.,

$$\left| f^{(k+1)} - f^{(k)} \right| \leq \epsilon. \tag{A.19}$$

where ϵ denotes the convergence threshold.

Appendix B

Appendices for Chapter 3

B.1 Rate Maximization using KKT Optimization

After analyzing the Rate Maximization problem (P1) in Chapter 3 under the TS protocol, all the possible solution cases of KKT-based solution are summarized in Table B.1. Similarly, for the considered PS protocol, the possible KKT-based cases are tabulated in Table B.2. A total of eight cases are obtained, out of which only two possible cases are feasible, and their corresponding solutions are provided in the main discussion on Chapter 3.

B.2 EH Maximization using KKT Optimization

For EH maximization involving the TS and PS protocols, the eight available KKT conditions are cataloged in Table B.4 and Table B.3, respectively. The possible two cases for individual TS and PS cases, respectively, have been marked with corresponding equations as well. Their complete solution which maximizes the EH is given in the main text of the Chapter 3.

Table B.1: Rate maximization: KKT cases for TS scheme.

KKT cases (TS)	**Sol.**	**Remark**
$\lambda_1{=}0{\Rightarrow}R_u^T(\alpha,P_b){\neq}\mathcal{R}_{th}$; $\lambda_2{=}0{\Rightarrow}E_h^T(\alpha,P_b){\neq}\xi_{th}$; $\lambda_3{=}0{\Rightarrow}(\mathcal{P}_{\max}-P_b){\neq}0$	$\alpha{=}1$	not possible
$\lambda_1{=}0{\Rightarrow}R_u^T(\alpha,P_b){\neq}\mathcal{R}_{th}$; $\lambda_2{=}0{\Rightarrow}E_h^T(\alpha,P_b){\neq}\xi_{th}$; $\lambda_3{\neq}0{\Rightarrow}(\mathcal{P}_{\max}-P_b){=}0$	$P_b{=}0$	not possible
$\lambda_1{=}0{\Rightarrow}R_u^T(\alpha,P_b){\neq}\mathcal{R}_{th}$; $\lambda_2{\neq}0{\Rightarrow}E_h^T(\alpha,P_b){=}\xi_{th}$; $\lambda_3{=}0{\Rightarrow}(\mathcal{P}_{\max}-P_b){\neq}0$	λ_2=-ve	not possible
$\lambda_1{=}0{\Rightarrow}R_u^T(\alpha,P_b){\neq}\mathcal{R}_{th}$; $\lambda_2{\neq}0{\Rightarrow}E_h^T(\alpha,P_b){=}\xi_{th}$; $\lambda_3{\neq}0{\Rightarrow}(\mathcal{P}_{\max}-P_b){=}0$	P_b^*(3.23) α^*(3.23)	possible
$\lambda_1{\neq}0{\Rightarrow}R_u^T(\alpha,P_b){=}\mathcal{R}_{th}$; $\lambda_2{=}0{\Rightarrow}E_h^T(\alpha,P_b){\neq}\xi_{th}$; $\lambda_3{=}0{\Rightarrow}(\mathcal{P}_{\max}-P_b){\neq}0$	$\lambda_1{=}{-}1$	not possible
$\lambda_1{\neq}0{\Rightarrow}R_u^T(\alpha,P_b){=}\mathcal{R}_{th}$; $\lambda_2{=}0{\Rightarrow}E_h^T(\alpha,P_b){\neq}\xi_{th}$; $\lambda_3{\neq}0{\Rightarrow}(\mathcal{P}_{\max}-P_b){=}0$	$\lambda_1{=}{-}1$	not possible
$\lambda_1{\neq}0{\Rightarrow}R_u^T(\alpha,P_b){=}\mathcal{R}_{th}$; $\lambda_2{\neq}0{\Rightarrow}E_h^T(\alpha,P_b){=}\xi_{th}$; $\lambda_3{=}0{\Rightarrow}(\mathcal{P}_{\max}-P_b){\neq}0$	$\lambda_1{=}{-}1$	not possible
$\lambda_1{\neq}0{\Rightarrow}R_u^T(\alpha,P_b){=}\mathcal{R}_{th}$; $\lambda_2{\neq}0{\Rightarrow}E_h^T(\alpha,P_b){=}\xi_{th}$; $\lambda_3{\neq}0{\Rightarrow}(\mathcal{P}_{\max}-P_b){=}0$	$P_b^\dagger$(3.24) $\alpha^\dagger$(3.24)	possible

Table B.2: Rate maximization: KKT cases for PS scheme.

KKT cases (PS)	**Sol.**	**Remark**
$\mu_1{=}0{\Rightarrow}R_u^P(\beta,P_b){\neq}\mathcal{R}_{th}$; $\mu_2{=}0{\Rightarrow}E_h^P(\beta,P_b){\neq}\xi_{th}$; $\mu_3{=}0{\Rightarrow}(\mathcal{P}_{\max}-P_b){\neq}0$	$P_b{=}0$	not possible
$\mu_1{=}0{\Rightarrow}R_u^P(\beta,P_b){\neq}\mathcal{R}_{th}$; $\mu_2{=}0{\Rightarrow}E_h^P(\beta,P_b){\neq}\xi_{th}$; $\mu_3{\neq}0{\Rightarrow}(\mathcal{P}_{\max}-P_b){=}0$	$P_b{=}0$	not possible
$\mu_1{=}0{\Rightarrow}R_u^P(\beta,P_b){\neq}\mathcal{R}_{th}$; $\mu_2{\neq}0{\Rightarrow}E_h^P(\beta,P_b){=}\xi_{th}$; $\mu_3{=}0{\Rightarrow}(\mathcal{P}_{\max}-P_b){\neq}0$	$P_b{=}0$	not possible
$\mu_1{=}0{\Rightarrow}R_u^P(\beta,P_b){\neq}\mathcal{R}_{th}$; $\mu_2{\neq}0{\Rightarrow}E_h^P(\beta,P_b){=}\xi_{th}$; $\mu_3{\neq}0{\Rightarrow}(\mathcal{P}_{\max}-P_b){=}0$	P_b^*(3.30) β^*(3.30)	possible
$\mu_1{\neq}0{\Rightarrow}R_u^P(\beta,P_b){=}\mathcal{R}_{th}$; $\mu_2{=}0{\Rightarrow}E_h^P(\beta,P_b){\neq}\xi_{th}$; $\mu_3{=}0{\Rightarrow}(\mathcal{P}_{\max}-P_b){\neq}0$	$\mu_1{=}{-}1$	not possible
$\mu_1{\neq}0{\Rightarrow}R_u^P(\beta,P_b){=}\mathcal{R}_{th}$; $\mu_2{=}0{\Rightarrow}E_h^P(\beta,P_b){\neq}\xi_{th}$; $\mu_3{\neq}0{\Rightarrow}(\mathcal{P}_{\max}-P_b){=}0$	$\mu_1{=}{-}1$	not possible
$\mu_1{\neq}0{\Rightarrow}R_u^P(\beta,P_b){=}\mathcal{R}_{th}$; $\mu_2{\neq}0{\Rightarrow}E_h^P(\beta,P_b){=}\xi_{th}$; $\mu_3{=}0{\Rightarrow}(\mathcal{P}_{\max}-P_b){\neq}0$	$\mu_1{=}{-}1$	not possible
$\mu_1{\neq}0{\Rightarrow}R_u^P(\beta,P_b){=}\mathcal{R}_{th}$; $\mu_2{\neq}0{\Rightarrow}E_h^P(\beta,P_b){=}\xi_{th}$; $\mu_3{\neq}0{\Rightarrow}(\mathcal{P}_{\max}-P_b){=}0$	$P_b^\dagger$(3.31) $\beta^\dagger$(3.31)	possible

Table B.3: KKT cases for EH maximization in TS scheme.

KKT cases (TS)	**Sol.**	**Remark**
$\lambda_1{=}0{\Rightarrow}R_u^T(\alpha,P_b){\neq}\mathcal{R}_{th}$; $\lambda_2{=}0{\Rightarrow}E_h^T(\alpha,P_b){\neq}\xi_{th}$; $\lambda_3{=}0{\Rightarrow}(\mathcal{P}_{\max}-P_b){\neq}0$	$\alpha{=}0$	not possible
$\lambda_1{=}0{\Rightarrow}R_u^T(\alpha,P_b){\neq}\mathcal{R}_{th}$; $\lambda_2{=}0{\Rightarrow}E_h^T(\alpha,P_b){\neq}\xi_{th}$; $\lambda_3{\neq}0{\Rightarrow}(\mathcal{P}_{\max}-P_b){=}0$	–	not feasible
$\lambda_1{=}0{\Rightarrow}R_u^T(\alpha,P_b){\neq}\mathcal{R}_{th}$; $\lambda_2{\neq}0{\Rightarrow}E_h^T(\alpha,P_b){=}\xi_{th}$; $\lambda_3{=}0{\Rightarrow}(\mathcal{P}_{\max}-P_b){\neq}0$	$\lambda_2{=}-1$	not possible
$\lambda_1{=}0{\Rightarrow}R_u^T(\alpha,P_b){\neq}\mathcal{R}_{th}$; $\lambda_2{\neq}0{\Rightarrow}E_h^T(\alpha,P_b){=}\xi_{th}$; $\lambda_3{\neq}0{\Rightarrow}(\mathcal{P}_{\max}-P_b){=}0$	$\lambda_2{=}-1$	not possible
$\lambda_1{\neq}0{\Rightarrow}R_u^T(\alpha,P_b){=}\mathcal{R}_{th}$; $\lambda_2{=}0{\Rightarrow}E_h^T(\alpha,P_b){\neq}\xi_{th}$; $\lambda_3{=}0{\Rightarrow}(\mathcal{P}_{\max}-P_b){\neq}0$	λ_1=-ve	not possible
$\lambda_1{\neq}0{\Rightarrow}R_u^T(\alpha,P_b){=}\mathcal{R}_{th}$; $\lambda_2{=}0{\Rightarrow}E_h^T(\alpha,P_b){\neq}\xi_{th}$; $\lambda_3{\neq}0{\Rightarrow}(\mathcal{P}_{\max}-P_b){=}0$	P_b^*(3.38) α^*(3.38)	possible
$\lambda_1{\neq}0{\Rightarrow}R_u^T(\alpha,P_b){=}\mathcal{R}_{th}$; $\lambda_2{\neq}0{\Rightarrow}E_h^T(\alpha,P_b){=}\xi_{th}$; $\lambda_3{=}0{\Rightarrow}(\mathcal{P}_{\max}-P_b){\neq}0$	λ_1=-ve	not possible
$\lambda_1{\neq}0{\Rightarrow}R_u^T(\alpha,P_b){=}\mathcal{R}_{th}$; $\lambda_2{\neq}0{\Rightarrow}E_h^T(\alpha,P_b){=}\xi_{th}$; $\lambda_3{\neq}0{\Rightarrow}(\mathcal{P}_{\max}-P_b){=}0$	$P_b^\dagger$(3.39) $\alpha^\dagger$(3.39)	possible

Table B.4: KKT cases for EH maximization in PS scheme.

KKT cases (PS)	**Sol.**	**Remark**
$\mu_1{=}0{\Rightarrow}R_u^P(\beta,P_b){\neq}\mathcal{R}_{th}$; $\mu_2{=}0{\Rightarrow}E_h^P(\beta,P_b){\neq}\xi_{th}$; $\mu_3{=}0{\Rightarrow}(\mathcal{P}_{\max}-P_b){\neq}0$	$\beta=0$ $P_b=0$	not possible
$\mu_1{=}0{\Rightarrow}R_u^P(\beta,P_b){\neq}\mathcal{R}_{th}$; $\mu_2{=}0{\Rightarrow}E_h^P(\beta,P_b){\neq}\xi_{th}$; $\mu_3{\neq}0{\Rightarrow}(\mathcal{P}_{\max}-P_b){=}0$	$P_b{=}0$	not feasible
$\mu_1{=}0{\Rightarrow}R_u^P(\beta,P_b){\neq}\mathcal{R}_{th}$; $\mu_2{\neq}0{\Rightarrow}E_h^P(\beta,P_b){=}\xi_{th}$; $\mu_3{=}0{\Rightarrow}(\mathcal{P}_{\max}-P_b){\neq}0$	$\mu_2{=}-1$	not possible
$\mu_1{=}0{\Rightarrow}R_u^P(\beta,P_b){\neq}\mathcal{R}_{th}$; $\mu_2{\neq}0{\Rightarrow}E_h^P(\beta,P_b){=}\xi_{th}$; $\mu_3{\neq}0{\Rightarrow}(\mathcal{P}_{\max}-P_b){=}0$	$\mu_2{=}-1$	not possible
$\mu_1{\neq}0{\Rightarrow}R_u^P(\beta,P_b){=}\mathcal{R}_{th}$; $\mu_2{=}0{\Rightarrow}E_h^P(\beta,P_b){\neq}\xi_{th}$; $\mu_3{=}0{\Rightarrow}(\mathcal{P}_{\max}-P_b){\neq}0$	$P_b{=}0$	not possible
$\mu_1{\neq}0{\Rightarrow}R_u^P(\beta,P_b){=}\mathcal{R}_{th}$; $\mu_2{=}0{\Rightarrow}E_h^P(\beta,P_b){\neq}\xi_{th}$; $\mu_3{\neq}0{\Rightarrow}(\mathcal{P}_{\max}-P_b){=}0$	P_b^*(3.44) β^*(3.44)	possible
$\mu_1{\neq}0{\Rightarrow}R_u^P(\beta,P_b){=}\mathcal{R}_{th}$; $\mu_2{\neq}0{\Rightarrow}E_h^P(\beta,P_b){=}\xi_{th}$; $\mu_3{=}0{\Rightarrow}(\mathcal{P}_{\max}-P_b){\neq}0$	$\mu_1{=}0$	not possible
$\mu_1{\neq}0{\Rightarrow}R_u^P(\beta,P_b){=}\mathcal{R}_{th}$; $\mu_2{\neq}0{\Rightarrow}E_h^P(\beta,P_b){=}\xi_{th}$; $\mu_3{\neq}0{\Rightarrow}(\mathcal{P}_{\max}-P_b){=}0$	$P_b^\dagger$(3.45) $\beta^\dagger$(3.45)	possible

Bibliography

[1] Q. Shi, L. Liu, W. Xu, and R. Zhang, "Joint transmit beamforming and receive power splitting for MISO SWIPT systems," *IEEE Trans. Wireless Commun.*, vol. 13, no. 6, pp. 3269–3280, 2014.

[2] Q. Zhang, J. Liu, H. Tang, Z. Dong, and Y. Li, "Practical RIS-aided multiuser communications with imperfect CSI: Practical model, amplitude feedback, and beamforming optimization," *IEEE Trans. Wireless Commun.*, vol. 23, no. 10, pp. 15 245–15 260, 2024.

[3] G. Wu, X. Zhao, H. Jiang, and Z. Chen, "Joint beamforming optimization for UAV and an active RIS-assisted hybrid DFRC systems," *IEEE Internet Things J.*, vol. 12, no. 18, pp. 38 059–38 072, 2025.

[4] E. M. Abadi, A. N. Hokmabadi, and S. Gezici, "Joint RIS Phase Profile Design and Power Allocation for Parameter Estimation in Presence of Eavesdropping," *IEEE Trans. Veh. Technol.*, vol. 73, no. 12, pp. 19 186–19 202, 2024.

[5] M. Series, "IMT vision — framework and overall objectives of the future development of IMT for 2020 and beyond," *Recommendation ITU-R M.2083-0*, 2015.

[6] R. Singh, A. Kaushik, W. Shin, M. D. Renzo, V. Sciancalepore, D. Lee, H. Sasaki,

A. Shojaeifard, and O. A. Dobre, "Towards 6G evolution: Three enhancements, three innovations, and three major challenges," *IEEE Network*, pp. 1–1, 2025.

[7] G. Moloudian, M. Hosseinifard, S. Kumar, R. B. V. B. Simorangkir, J. L. Buckley, C. Song, G. Fantoni, and B. O'Flynn, "RF Energy harvesting techniques for battery-less wireless sensing, industry 4.0, and internet of things: A review," *IEEE Sensors J.*, vol. 24, no. 5, pp. 5732–5745, 2024.

[8] I. Krikidis, S. Timotheou, S. Nikolaou, G. Zheng, D. W. K. Ng, and R. Schober, "Simultaneous wireless information and power transfer in modern communication systems," *IEEE Commun. Mag.*, vol. 52, no. 11, pp. 104–110, 2014.

[9] J. Ding, M. Nemati, C. Ranaweera, and J. Choi, "IoT Connectivity technologies and applications: A survey," *IEEE Access*, vol. 8, pp. 67 646–67 673, 2020.

[10] L. Li and Y. Jiang, "Design of high-efficiency microwatt RF energy harvesting system," *IEEE Trans. Power Electronics*, vol. 39, no. 5, pp. 5883–5901, 2024.

[11] M. V. Katwe, A. Kaushik, L. Mohjazi, M. Abualhayja'a, D. Dardari, K. Singh, M. A. Imran, M. M. Butt, and O. A. Dobre, "An overview of intelligent meta-surfaces for 6G and beyond: Opportunities, trends, and challenges," *IEEE Commun. Stand. Mag.*, vol. 8, no. 4, pp. 62–69, 2024.

[12] S. Kumar, V. Sharma, and A. Sharma, "SWIPT Module for battery-less ultra-low-power sensor nodes," *IEEE Sensors Lett.*, vol. 8, no. 12, pp. 1–4, 2024.

[13] M. Di Renzo, A. Zappone, M. Debbah, M.-S. Alouini, C. Yuen, J. de Rosny, and S. Tretyakov, "Smart radio environments empowered by reconfigurable intelligent surfaces: How it works, state of research, and the road ahead," *IEEE J. Sel. Areas Commun.*, vol. 38, no. 11, pp. 2450–2525, 2020.

[14] K. Ntontin, A. A. Boulogeorgos, E. Björnson, W. A. Martins, S. Kisseleff, S. Abadal, E. Alarcón, A. Papazafeiropoulos, F. I. Lazarakis, and S. Chatzinotas, "Wireless energy harvesting for autonomous reconfigurable intelligent surfaces," *IEEE Trans. Green Commun. Netw.*, vol. 7, no. 1, pp. 114–129, 2023.

[15] Q. Wu and R. Zhang, "Beamforming optimization for wireless network aided by intelligent reflecting surface with discrete phase shifts," *IEEE Trans. Commun.*, vol. 68, no. 3, pp. 1838–1851, 2020.

[16] M. Aldababsa, A. M. Salhab, A. A. Nasir, M. H. Samuh, and D. B. da Costa, "Multiple RISs-aided networks: Performance analysis and optimization," *IEEE Trans. Veh. Tech.*, vol. 72, no. 6, pp. 7545–7559, 2023.

[17] Y. Liu, X. Mu, J. Xu, R. Schober, Y. Hao, H. V. Poor, and L. Hanzo, "STAR: Simultaneous transmission and reflection for 360° coverage by intelligent surfaces," *IEEE Wireless Commun.*, vol. 28, no. 6, pp. 102–109, 2021.

[18] G. Zhou, C. Pan, H. Ren, K. Wang, M. D. Renzo, and A. Nallanathan, "Robust beamforming design for intelligent reflecting surface aided MISO communication systems," *IEEE Wireless Commun. Lett.*, vol. 9, no. 10, pp. 1658–1662, 2020.

[19] J.-C. Chen, "Designing STAR-RIS-assisted wireless systems with coupled and discrete phase shifts: A computationally efficient algorithm," *IEEE Trans. Veh. Technol.*, vol. 73, no. 7, pp. 10 772–10 777, 2024.

[20] S. Boyd and L. Vandenberghe, *Convex optimization*. Cambridge university press, 2004.

[21] M. Di Renzo, K. Ntontin, J. Song, F. H. Danufane, X. Qian, F. Lazarakis, J. De Rosny, D.-T. Phan-Huy, O. Simeone, R. Zhang, M. Debbah, G. Lerosey,

M. Fink, S. Tretyakov, and S. Shamai, "Reconfigurable intelligent surfaces vs. relaying: Differences, similarities, and performance comparison," *IEEE Open J. Commun. Soc.*, vol. 1, pp. 798–807, 2020.

[22] E. Basar, M. Di Renzo, J. De Rosny, M. Debbah, M.-S. Alouini, and R. Zhang, "Wireless communications through reconfigurable intelligent surfaces," *IEEE Access*, vol. 7, pp. 116 753–116 773, 2019.

[23] E. Björnson, Özdogan, and E. G. Larsson, "Reconfigurable intelligent surfaces: Three myths and two critical questions," *IEEE Commun. Mag.*, vol. 58, no. 12, pp. 90–96, 2020.

[24] S. Kisseleff, S. Chatzinotas, and B. Ottersten, "Reconfigurable intelligent surfaces in challenging environments: Underwater, underground, industrial and disaster," *IEEE Access*, vol. 9, pp. 150 214–150 233, 2021.

[25] S. Gautam, "Intelligent reflecting and refracting surfaces for SWIPT-enabled 6G RF-based communications," in *IEEE Veh. Technol. Conf. (VTC2025-Spring)*, 2025, pp. 1–6.

[26] W. Wang, W. Ni, H. Tian, Y. C. Eldar, and R. Zhang, "Multi-functional reconfigurable intelligent surface: System modeling and performance optimization," *IEEE Trans. Wireless Commun.*, vol. 23, no. 4, pp. 3025–3041, 2024.

[27] H. Li, S. Shen, M. Nerini, and B. Clerckx, "Reconfigurable intelligent surfaces 2.0: Beyond diagonal phase shift matrices," *IEEE Commun. Mag.*, vol. 62, no. 3, pp. 102–108, 2024.

[28] J. Peng, J. Zhang, J. Wang, L. Zheng, and X. Zhao, "Hybrid power supply-based

power scheduling and splitting for green SWIPT system," *IEEE Trans. Green Commun. Netw.*, vol. 9, no. 4, pp. 1810–1822, 2025.

[29] S. Gautam and P. Ubaidulla, "Relay selection and transceiver design for joint wireless information and energy transfer in cooperative networks," in *IEEE Veh. Technol. Conf.(VTC Spring)*, 2017, pp. 1–5.

[30] P. N. Alevizos and A. Bletsas, "Sensitive and nonlinear far-field RF energy harvesting in wireless communications," *IEEE Trans. Wireless Commun.*, vol. 17, no. 6, pp. 3670–3685, 2018.

[31] S. Gautam, S. Solanki, S. K. Sharma, S. Chatzinotas, and B. Ottersten, "Hybrid active-and-passive relaying model for 6G-IoT greencom networks with SWIPT," *Sensors*, vol. 21, no. 18, p. 6013, 2021.

[32] E. Boshkovska, D. W. K. Ng, N. Zlatanov, and R. Schober, "Practical non-linear energy harvesting model and resource allocation for SWIPT systems," *IEEE Commun. Lett.*, vol. 19, no. 12, pp. 2082–2085, 2015.

[33] S. Gautam, E. Lagunas, A. Bandi, S. Chatzinotas, S. K. Sharma, T. X. Vu, S. Kisseleff, and B. Ottersten, "Multigroup multicast precoding for energy optimization in SWIPT systems with heterogeneous users," *IEEE Open J. Commun. Soc.*, vol. 1, pp. 92–108, 2020.

[34] T. N. Do, G. Kaddoum, T. L. Nguyen, D. B. da Costa, and Z. J. Haas, "Multi-RIS-aided wireless systems: Statistical characterization and performance analysis," *IEEE Trans. Commun.*, vol. 69, no. 12, pp. 8641–8658, 2021.

[35] M. Yang, Y. Xu, C. Huang, D. Li, and Y. Peng, "Sum-rate maximization in RIS-

aided wireless-powered D2D communication networks," in *Int. Symp. Pers., Indoor, Mobile Radio Commun. (PIMRC)*, 2022, pp. 307–312.

[36] P. K. Sharma, N. Sharma, S. Dhok, and A. Singh, "RIS-assisted FD short packet communication with non-linear EH," *IEEE Commun. Lett.*, vol. 27, no. 2, pp. 522–526, 2023.

[37] S. Dhok, P. Raut, P. K. Sharma, K. Singh, and C.-P. Li, "Non-linear energy harvesting in RIS-assisted URLLC networks for industry automation," *IEEE Trans. Commun.*, vol. 69, no. 11, pp. 7761–7774, 2021.

[38] K. Xu, Z. Shen, M. Zhang, Y. Wang, X. Xia, W. Xie, and D. Zhang, "Beam-domain SWIPT for MIMO system with nonlinear energy harvesting legitimate terminals and a non-cooperative terminal," *IEEE Trans. Green Commun. Netw.*, vol. 3, no. 3, pp. 703–720, 2019.

[39] W. Lu, X. Xu, G. Huang, B. Li, Y. Wu, N. Zhao, and F. R. Yu, "Energy efficiency optimization in SWIPT enabled WSNs for smart agriculture," *IEEE Trans. Ind. Inform.*, vol. 17, no. 6, pp. 4335–4344, 2021.

[40] K. Lin and Y. Mao, "RIS-aided wireless-powered backscatter communications for sustainable internet of underground things," *IEEE Internet Things Mag.*, vol. 8, no. 2, pp. 70–76, 2025.

[41] M. B. Kokare, R. Swaminathan, and S. Gautam, "Performance analysis and optimization with deep learning assessment of multi-IRS-aided IoV network," *IEEE Internet Things J.*, vol. 12, no. 9, pp. 11 581–11 599, 2025.

[42] S. P. Dash and A. Kaushik, "RIS-assisted 6G wireless communications: A novel

statistical framework in the presence of direct channel," *IEEE Commun. Lett.*, vol. 28, no. 3, pp. 717–721, 2024.

[43] A. Mohamed, A. Zappone, and M. Di Renzo, "Bi-objective optimization of information rate and harvested power in RIS-aided SWIPT systems," *IEEE Wireless Commun. Lett.*, vol. 11, no. 10, pp. 2195–2199, 2022.

[44] W. Wang, W. Ni, H. Tian, Y. C. Eldar, and R. Zhang, "Multi-functional reconfigurable intelligent surface: System modeling and performance optimization," *IEEE Trans. Wireless Commun.*, vol. 23, no. 4, pp. 3025–3041, 2024.

[45] D. L. Galappaththige and G. Aruma Baduge, "Exploiting distributed IRSs for enabling SWIPT," *IEEE Wireless Commun. Lett.*, vol. 11, no. 4, pp. 673–677, 2022.

[46] Z. Mohamed and S. Aïssa, "Wireless power transfer aided with reconfigurable intelligent surfaces: Design, and coverage analysis," in *IEEE inter. symp. pers., indoor and mobile radio commun. (PIMRC)*, 2022, pp. 695–700.

[47] N. P. Le and K. N. Le, "Distributed-RIS assisted wireless powered communication networks in the finite blocklength regim," *IEEE Commun. Lett.*, vol. 26, no. 12, pp. 2884–2888, 2022.

[48] I. Yildirim, A. Uyrus, and E. Basar, "Modeling and analysis of reconfigurable intelligent surfaces for indoor and outdoor applications in future wireless networks," *IEEE Trans. Commun.*, vol. 69, no. 2, pp. 1290–1301, 2021.

[49] Z. Yang, M. Chen, W. Saad, W. Xu, M. Shikh-Bahaei, H. V. Poor, and S. Cui, "Energy-efficient wireless communications with distributed reconfigurable intelligent surfaces," *IEEE Trans. Wireless Commun.*, vol. 21, no. 1, pp. 665–679, 2022.

[50] Y. Fang, S. Atapattu, H. Inaltekin, and J. Evans, "Optimum reconfigurable intelligent surface selection for wireless networks," *IEEE Trans. Commun.*, vol. 70, no. 9, pp. 6241–6258, 2022.

[51] S. Zargari, A. Khalili, and R. Zhang, "Energy efficiency maximization via joint active and passive beamforming design for multiuser MISO IRS-aided SWIPT," *IEEE Wireless Commun. Lett.*, vol. 10, no. 3, pp. 557–561, 2021.

[52] M. B. Kokare, S. Gautam, and R. Swaminathan, "On efficient resource allocation strategies for Multi-RIS enhanced V2I SWIPT systems," in *IEEE Wireless Commun. Netw. Conf. (WCNC)*, 2024 , pp. 1–6.

[53] N. Sharma, S. Gautam, S. Chatzinotas, and B. Ottersten, "On optimizing RIS-aided SWIPT-IoT with power splitting-based non-linear energy harvesting," in *IEEE Global Commun. Conf. (GLOBECOM)*, 2023, pp. 619–624.

[54] N. Sharma, S. Gautam, A. Kaushik, S. Chatzinotas, and B. Ottersten, "Fractional programming strategy for rate-energy optimization in RIS-assisted SWIPT IoT networks," in *IEEE Global Commun. Conf. (GLOBECOM)*, 2024, pp. 5126–5131.

[55] N. Sharma, S. Gautam, S. Chatzinotas, and B. Ottersten, "Fractional programming based optimization techniques for RIS-assisted SWIPT-IoT system," *IEEE Commun. Lett.*, pp. 1–1, 2024.

[56] J. Yaswanth, S. K. Singh, K. Singh, and M. F. Flanagan, "Energy-efficient beamforming design for RIS-aided MIMO downlink communication with SWIPT," *IEEE Trans. Green Commun. Netw.*, vol. 7, no. 3, pp. 1164–1180, 2023 .

[57] E. Björnson, Özdogan, and E. G. Larsson, "Intelligent reflecting surface versus

decode-and-forward: How large surfaces are needed to beat relaying?" *IEEE Wireless Commun. Lett.*, vol. 9, no. 2, pp. 244–248, 2020.

[58] Z. Li, M. Hua, Q. Wang, and Q. Song, "Weighted sum-rate maximization for multi-IRS aided cooperative transmission," *IEEE Wireless Commun. Lett.*, vol. 9, no. 10, pp. 1620–1624, 2020.

[59] D. L. Galappaththige, D. Kudathanthirige, and G. Amarasuriya, "Performance analysis of distributed intelligent reflective surface aided communications," in *IEEE Global Commun. Conf. (GLOBECOM)*, 2020, pp. 1–6.

[60] N. Sharma and S. Gautam, "Optimizing RIS-assisted wireless communication systems with non-linear energy harvesting," in *Int. Conf. Energy, Power and Environment (ICEPE)*, 2023, pp. 1–5.

[61] J. C. Bezdek and R. J. Hathaway, "Convergence of alternating optimization," *Neural, Parallel Sci. Comput.*, vol. 11, no. 4, p. 351–368, 2003.

[62] P. Series, "Propagation data and prediction methods for the planning of short-range outdoor radiocommunication systems and radio local area networks in the frequency range 300 MHz to 100 GHz," *ITU recommmendations*, pp. 1411–9, 2017 .

[63] W. Mei and R. Zhang, "Cooperative beam routing for multi-IRS aided communication," *IEEE Wireless Commun. Lett.*, vol. 10, no. 2, pp. 426–430, 2021.

[64] Y. Zhang, J. Zhang, M. Di Renzo, H. Xiao, and B. Ai, "Reconfigurable Intelligent Surfaces With Outdated Channel State Information: Centralized vs. Distributed Deployments," *IEEE Trans. Commun.*, vol. 70, no. 4, pp. 2742–2756, 2022.

[65] S. Gautam, S. Kumar, S. Chatzinotas, and B. Ottersten, "Experimental evaluation

of RF waveform designs for wireless power transfer using software defined radio," *IEEE Access*, vol. 9, pp. 132 609–132 622, 2021.

[66] Q. Wu, X. Guan, and R. Zhang, "Intelligent reflecting surface-aided wireless energy and information transmission: An overview," *Proc. IEEE*, vol. 110, no. 1, pp. 150–170, 2022.

[67] Q. Wu and R. Zhang, "Weighted sum power maximization for intelligent reflecting surface aided SWIPT," *IEEE Wireless Commun. Lett.*, vol. 9, no. 5, pp. 586–590, 2020.

[68] X. Peng, P. Wu, H. Tan, and M. Xia, "Optimization for IRS-assisted MIMO-OFDM SWIPT system with nonlinear EH model," *IEEE Internet Things J.*, vol. 9, no. 24, pp. 25 253–25 268, 2022.

[69] J. Tang, Y. Yu, M. Liu, D. K. C. So, X. Zhang, Z. Li, and K.-K. Wong, "Joint power allocation and splitting control for SWIPT-enabled NOMA systems," *IEEE Trans. Wireless Commun.*, vol. 19, no. 1, pp. 120–133, 2020.

[70] V. Sharma, J. Yaswanth, S. K. Singh, S. Biswas, K. Singh, and F. Khan, "A pricing-based approach for energy-efficiency maximization in RIS-aided multi-user MIMO SWIPT-enabled wireless networks," *IEEE Access*, vol. 10, pp. 29 132–29 148, 2022.

[71] Z. Chen, J. Tang, N. Zhao, M. Liu, and D. K. C. So, "Hybrid beamforming with discrete phase shifts for RIS-assisted multiuser SWIPT system," *IEEE Wireless Commun. Lett.*, vol. 12, no. 1, pp. 104–108, 2023.

[72] A. Khalili, S. Zargari, Q. Wu, D. W. K. Ng, and R. Zhang, "Multi-objective resource allocation for IRS-aided SWIPT," *IEEE Wireless Commun. Lett.*, vol. 10, no. 6, pp. 1324–1328, 2021.

[73] Y. Xu, B. Gu, Z. Gao, D. Li, Q. Wu, and C. Yuen, "Applying RIS in multi-user SWIPT-WPCN systems: A robust and environmentally-friendly design," *IEEE Trans. Cognitive Commun. Netw.*, vol. 10, no. 1, pp. 209–222, 2024.

[74] S. Abeywickrama, R. Zhang, Q. Wu, and C. Yuen, "Intelligent reflecting surface: Practical phase shift model and beamforming optimization," *IEEE Trans. Commun.*, vol. 68, no. 9, pp. 5849–5863, 2020.

[75] S. Zargari, A. Khalili, and R. Zhang, "Energy efficiency maximization via joint active and passive beamforming design for multiuser MISO IRS-aided SWIPT," *IEEE Wireless Commun. Lett.*, vol. 10, no. 3, pp. 557–561, 2021.

[76] K. Shen and W. Yu, "Fractional programming for communication systems—part I: Power control and beamforming," *IEEE Trans. Signal Proc.*, vol. 66, no. 10, pp. 2616–2630, 2018.

[77] S. Gautam, E. Lagunas, S. Vuppala, S. Chatzinotas, and B. Ottersten, "Pricing perspective for SWIPT in OFDM-based multi-user wireless cooperative systems," in *IEEE Wireless Commun. Netw. Conf. (WCNC)*, 2019, pp. 1–7.

[78] A. T. Phillips, *Quadratic fractional programming: Dinkelbach method.* Boston, MA: Springer US, 2009, pp. 3149–3153. [Online]. Available: https://doi.org/10.1007/978-0-387-74759-0_535

[79] S. Zargari, A. Hakimi, C. Tellambura, and S. Herath, "Multiuser MISO PS-SWIPT Systems: Active or Passive RIS?" *IEEE Wireless Commun. Lett.*, vol. 11, no. 9, pp. 1920–1924, 2022.

[80] H. Guo, Y.-C. Liang, J. Chen, and E. G. Larsson, "Weighted sum-rate maximization

for reconfigurable intelligent surface aided wireless networks," *IEEE Trans. Wireless Commun.*, vol. 19, no. 5, pp. 3064–3076, 2020.

[81] C. Huang, A. Zappone, G. C. Alexandropoulos, M. Debbah, and C. Yuen, "Reconfigurable intelligent surfaces for energy efficiency in wireless communication," *IEEE Trans. Wireless Commun.*, vol. 18, no. 8, pp. 4157–4170, 2019.

[82] C. Pan, H. Ren, K. Wang, M. Elkashlan, A. Nallanathan, J. Wang, and L. Hanzo, "Intelligent reflecting surface aided MIMO broadcasting for simultaneous wireless information and power transfer," *IEEE J. Selected Areas Commun.*, vol. 38, no. 8, pp. 1719–1734, 2020.

[83] B. Zhang, K. Yang, K. Wang, and G. Zhang, "Performance analysis for RIS-assisted SWIPT-enabled IoT systems," *IEEE Trans. Wireless Commun.*, vol. 23, no. 8, pp. 10 030–10 043, 2024.

[84] D. Xu, V. Jamali, X. Yu, D. W. K. Ng, and R. Schober, "Optimal resource allocation design for large IRS-assisted SWIPT systems: A scalable optimization framework," *IEEE Trans. Commun.*, vol. 70, no. 2, pp. 1423–1441, 2022.

[85] Y. Gao, Q. Wu, G. Zhang, W. Chen, D. W. K. Ng, and M. D. Renzo, "Beamforming optimization for active intelligent reflecting surface-aided SWIPT," *IEEE Trans. Wireless Commun.*, vol. 22, no. 1, pp. 362–378, 2023.

[86] X. Peng, P. Wu, H. Tan, and M. Xia, "Optimization for IRS-assisted MIMO-ofdm SWIPT system with nonlinear EH model," *IEEE Internet Things J.*, vol. 9, no. 24, pp. 25 253–25 268, 2022.

[87] J. Tang, Z. Peng, D. K. C. So, X. Zhang, K.-K. Wong, and J. A. Chambers, "Energy

efficiency optimization for a multiuser IRS-aided MISO system with SWIPT," *IEEE Trans. Commun.*, vol. 71, no. 10, pp. 5950–5962, 2023.

[88] J. Yaswanth, S. K. Singh, K. Singh, and M. F. Flanagan, "Energy-efficient beamforming design for RIS-aided MIMO downlink communication with SWIPT," *IEEE Trans. Green Commun. Netw.*, vol. 7, no. 3, pp. 1164–1180, 2023.

[89] V. Sharma, R. Allu, S. K. Singh, K. Singh, T. Q. Duong, and T. A. Tsiftsis, "Robust transmission design in multiobjective RIS-aided SWIPT IoT communications," *IEEE Internet Things J.*, vol. 11, no. 10, pp. 18 605–18 618, 2024.

[90] L. Chai, L. Bai, T. Bai, J. Choi, and W. Zhang, "RIS-aided SCMA-based SWIPT systems: Design and optimization," *IEEE Trans. Veh. Technol.*, vol. 72, no. 5, pp. 6238–6252, 2023.

[91] M. Mohammadi, H. Q. Ngo, and M. Matthaiou, "Phase-shift and transmit power optimization for RIS-aided massive MIMO SWIPT IoT networks," *IEEE Trans. Commun.*, vol. 73, no. 1, pp. 631–647, 2025.

[92] Y. Zheng, S. A. Tegos, Y. Xiao, P. D. Diamantoulakis, Z. Ma, and G. K. Karagiannidis, "Zero-energy device networks with wireless-powered RISs," *IEEE Trans. Veh. Technol.*, vol. 72, no. 10, pp. 13 655–13 660, 2023.

[93] C. Zhang, Y. Huang, C. He, C. Pan, and K. Wang, "Energy optimization for IRS-aided SWIPT under imperfect cascaded channels," *IEEE Trans. Veh. Technol.*, vol. 72, no. 9, pp. 11 631–11 643, 2023.

[94] S. Gong, Z. Yang, C. Xing, J. An, and L. Hanzo, "Beamforming optimization for intelligent reflecting surface-aided SWIPT IoT networks relying on discrete phase shifts," *IEEE Internet Things J.*, vol. 8, no. 10, pp. 8585–8602, 2021.

[95] N. Sharma, S. Gautam, S. Chatzinotas, and B. Ottersten, "Integrating multiple RIS for enhanced SWIPT-IoT performance: Optimization strategies," *IEEE Access*, vol. 12, pp. 182 841–182 855, 2024.

[96] Q. Xue, R. Wei, Z. Li, Y. Liu, Y. Xu, and Q. Chen, "Beamforming design for cooperative double-RIS aided mmWave MU-MIMO communications," *IEEE Trans. Green Commun. Netw.*, vol. 9, no. 2, pp. 645–657, 2025.

[97] "Bharat 6G vision statement," March 2023, https://dot.gov.in/circular-and-notifications/3199.

[98] X. Mu, Y. Liu, L. Guo, J. Lin, and R. Schober, "Simultaneously transmitting and reflecting (STAR) RIS aided wireless communications," *IEEE Trans. Wireless Commun.*, vol. 21, no. 5, pp. 3083–3098, 2022.

[99] J. Xu, Y. Liu, X. Mu, and O. A. Dobre, "STAR-RISs: Simultaneous transmitting and reflecting reconfigurable intelligent surfaces," *IEEE Commun. Lett.*, vol. 25, no. 9, pp. 3134–3138, 2021.

[100] D. Gunasinghe and G. Amarasuriya, "Performance analysis of STAR-RIS for wireless communication," in *IEEE Int. Conf. Commun. (ICC)*, 2022, pp. 3275–3280.

[101] H. Zhang, J. Nie, Y. Yu, Z. Xiong, W. Jiang, and D. Niyato, "Performance analysis for STAR-RIS assisted SWIPT system over rayleigh fading channel," in *IEEE Int. Conf. Commun. (ICC)*, 2023, pp. 1468–1473.

[102] P. Zhao, J. Zuo, and C. Wen, "Power allocation and beamforming vectors optimization in STAR-RIS assisted SWIPT," in *IEEE Int. Conf. Commun. Tech. (ICCT)*, 2022, pp. 1174–1178.

[103] A. Farhadi, M. Moomivand, S. K. Taskou, M. R. Mili, M. Rasti, and E. Hossain, "A meta-DDPG algorithm for energy and spectral efficiency optimization in STAR-RIS-aided SWIPT," *IEEE Wireless Commun. Lett.*, vol. 13, no. 5, pp. 1473–1477, 2024.

[104] Y. Li, J. Wang, Y. Zou, W. Xie, and Y. Liu, "Weighted sum power maximization for STAR-RIS assisted SWIPT systems," *IEEE Trans. Wireless Commun.*, pp. 1–1, 2024.

[105] S. Dhok and P. K. Sharma, "Rate-splitting multiple access with STAR RIS over spatially-correlated channels," *IEEE Trans. Commun.*, vol. 70, no. 10, pp. 6410–6424, 2022.

[106] Y. Liu, Y. Ni, H. Zhao, Y. Yang, S. Qiao, and H. Zhu, "STAR-RIS Assisted wireless communications with discrete phase shifter," *IEEE Wireless Commun. Lett.*, vol. 13, no. 11, pp. 3152–3156, 2024.

[107] J.-C. Chen, "Designing STAR-RIS-assisted wireless systems with coupled and discrete phase shifts: A computationally efficient algorithm," *IEEE Trans. Veh. Technol.*, vol. 73, no. 7, pp. 10 772–10 777, 2024.

[108] N. Sharma and S. Gautam, "Optimization strategy for RIS-assisted SWIPT-IoT with non-linear energy harvesting," in *National Conf. commun. (NCC)*, 2024, pp. 1–6.

[109] Q. Gao, Y. Liu, X. Mu, M. Jia, D. Li, and L. Hanzo, "Joint Location and Beamforming Design for STAR-RIS Assisted NOMA Systems," *IEEE Trans. Commun.*, vol. 71, no. 4, pp. 2532–2546, 2023.

[110] S. Basharat, S. A. Hassan, H. Pervaiz, A. Mahmood, Z. Ding, and M. Gidlund, "Reconfigurable intelligent surfaces: Potentials, applications, and challenges for 6G wireless networks," *IEEE Wireless Commun.*, vol. 28, no. 6, pp. 184–191, 2021.

[111] Z. Chen, G. Chen, J. Tang, S. Zhang, D. K. So, O. A. Dobre, K.-K. Wong, and J. Chambers, "Reconfigurable-intelligent-surface-assisted B5G/6G wireless communications: Challenges, solution, and future opportunities," *IEEE Commun. Mag.*, vol. 61, no. 1, pp. 16–22, 2023.

[112] S. Dhok and N. B. Mehta, "Two-timescale channel estimation for RIS-assisted near-field communication," in *IEEE Int. Conf. Acoustics, Speech, Signal Process. (ICASSP)*, 2026, pp. 21 536–21 540.

[113] Siradel, "How to improve 5G coverage in a factory using reconfigurable intelligent surfaces (RIS)?" 2025, [Online]. Available: https://www.siradel.com/ris-for-improved-5g-in-factories/.

[114] H. M. Jawad, R. Nordin, S. K. Gharghan, A. M. Jawad, and M. Ismail, "Energy-efficient wireless sensor networks for precision agriculture: A review," *Sensors*, vol. 17, no. 8, p. 1781, 2017.

[115] Y. Li, K. Xiong, W. Zhang, W. Chen, P. Fan, Y. Zhang, and K. B. Letaief, "Robust transmit beamforming for integrating communication, sensing and power transfer systems," *IEEE Internet Things J.*, pp. 1–1, 2026.

[116] S. Uniyal, N. Vishwakarma, S. Sharma, and R. Swaminathan, "Intelligent reflecting surfaces-aided mixed FSO/RF communication system," in *IEEE Wireless Commun. Netw. Conf. (WCNC)*, 2023, pp. 1–6.

[117] D. Shambharkar, S. Dhok, A. Singh, and P. K. Sharma, "Rate-splitting multiple access for RIS-aided cell-edge users with discrete phase-shifts," *IEEE Commun. Lett.*, vol. 26, no. 11, pp. 2581–2585, 2022.

[118] H. Liu, J. An, X. Jia, L. Gan, G. K. Karagiannidis, B. Clerckx, M. Bennis, M. Debbah, and T. J. Cui, "Stacked intelligent metasurfaces for wireless communications: Applications and challenges," *IEEE Wireless Commun.*, vol. 32, no. 4, pp. 46–53, 2025.

[119] N. Sharma, S. Gautam, S. Chatzinotas, and B. Ottersten, "Power optimization in RIS-assisted SWIPT-IoT system with discrete phase shift," *IEEE Internet Things J.*, vol. 13, no. 11, pp. 22 770–22 786, 2026.

[120] N. Sharma, M. B. Kokare, S. R, and S. Gautam, "Distributed RIS SWIPT-IoT systems: Optimizing spectral efficiency and energy harvesting," in *IEEE Wireless Commun. Netw. Conf. (WCNC)*, 2025, pp. 1–6.

[121] N. Sharma, M. B. Kokare, R. Swaminathan, and S. Gautam, "Maximizing weighted function in STAR-RIS aided SWIPT-IoT with discrete phase shifting," in *IEEE Veh. Technol. Conf. (VTC2025-Spring)*, 2025, pp. 1–5.